

ABSTRACT

ROBICHAUD, GUILLAUME. Design, Fabrication and Testing of a High Precision Air Amplifier as an Ion Focusing Device for Mass Spectrometry. (Under the direction of Thomas A. Dow.)

The objective of this research was to design, fabricate and evaluate the use of an air amplifier to improve the capture and detection of the ions generated by electrospray ionization mass spectrometry. Mass spectrometry is an analytical method widely used by chemists and biologists to determine the nature and/or the abundance of molecules and proteins in a sample. The capability to detect very low concentrations of a molecule is often critical in applications such as the detection of cancer biomarkers in blood samples.

Prior to being measured by the mass spectrometer, individual molecules have to be ionized, put into gas phase and transported to the mass spectrometer inlet. It is estimated that less than 1% of the gas phase ions that have been created will be successfully captured by the mass spectrometer, mainly due to the coulombic repulsive force scattering the ions away from each other. By placing the mass spectrometer inlet along the axis of an air amplifier, the device has the potential to focus the scattering ion toward the inlet and improve the abundance of ion collected (abundance is proportional to number of ion captured by the instrument).

Proof of concept of the use of an air amplifier or Venturi device to improve abundance of ion collected in mass spectrometry has been made previously using a commercial device. It was then that imprecise control and slight misalignment of the gap impacted performance and repeatability of the results. It was concluded that a precision engineered air amplifier was needed to fully investigate the effect of the device on the abundance of ion collected by the instrument.

Two devices were designed and fabricated. Air Amplifier I, with an adjustable annular gap, was first designed to investigate the effect of gap width and plenum pressure on the gas flow. It was concluded that gap could be fixed since effect of increasing gap was equivalent to increasing the plenum pressure. Also, design of experiment was used to investigate the effect of different variables on the ion abundance and it was found that the use of an air amplifier could improve ion abundance in condition where desolvation is typically low (up to 34x).

Since it was shown that abundance can be improved by reducing the length of the MS inlet tube, Air Amplifier II, a more compact version of the device with a fixed gap was designed to reduce to a minimum this MS inlet. It was possible to reduce the MS inlet length to 23 mm without affecting the performance of the air amplifier. Result of this research also confirmed that symmetry of the flow was improved using a precision engineered device.

Design, Fabrication and Testing of a High Precision Air Amplifier as an
Ion Focusing Device for Mass Spectrometry

by
Guillaume Robichaud

A thesis submitted to the Graduate Faculty of
North Carolina State University
in partial fulfillment of the
requirements for the Degree of
Master of Science

Mechanical Engineering

Raleigh, North Carolina

2011

APPROVED BY:

Dr. Thomas A. Dow
Advisory Committee Chair

Dr. David C. Muddiman

Dr. Jeffrey W. Eischen

Dr. Ronald O. Scattergood

BIOGRAPHY

Guillaume was born on April 6th 1978 in Alma, a small town in northern Québec, Canada. After backpacking in Europe for almost a year and planting 950 000 trees he started his B.Eng. degree in Mechanical Engineering at École Polytechnique de Montréal while working part time for General Electric Hydro, assisting mechanical engineers in the design of large hydroelectric turbines. After his graduation in 2003, he worked 5 years as a technical advisor/site engineer, installing hydroelectric turbines and generators at multiple locations around the world. After meeting his future wife in North Carolina, he decided to pursue a Masters degree at North Carolina State University.

TABLE OF CONTENTS

| | |
|--|------------|
| LIST OF FIGURES | iv |
| LIST OF TABLES | vii |
| 1. INTRODUCTION | 1 |
| 1.1 Background Information | 1 |
| 1.1.1 What is mass spectrometry? | 1 |
| 1.1.2 Abundance and mass to charge ratio | 1 |
| 1.1.3 Mass spectrometer instrument | 2 |
| 1.1.4 Electrospray ionization | 8 |
| 1.2 Previous work | 12 |
| 1.3 Problem Statement | 14 |
| 2. AIR AMPLIFIER I | 15 |
| 2.1 Design | 15 |
| 2.2 Fabrication | 20 |
| 2.2.1 Setup and Tool Centering | 21 |
| 2.2.2 Machining and Assembly | 27 |
| 2.2.3 Piezoelectric Actuators Calibration | 32 |
| 2.3 Testing | 36 |
| 2.3.1 Static pressure measurements | 36 |
| 2.3.2 Characterization Using Current Measurement..... | 38 |
| 2.3.3 Fourier Transform Mass Spectrometer (FTMS)..... | 42 |
| 2.3.4 Design of Experiment | 44 |
| 2.3.5 Results on a QqQ Mass Spectrometer | 47 |
| 3. AIR AMPLIFIER II | 53 |
| 3.1 Design | 53 |
| 3.2 Fabrication | 55 |
| 3.3 Testing | 57 |
| 3.3.1 Static pressure measurement..... | 57 |
| 3.3.2 LTQ-FTMS tests..... | 63 |
| 4. CONCLUSION AND FUTURE WORK | 69 |
| REFERENCES | 71 |
| APPENDIX | 74 |
| APPENDIX A – First Iteration Air Amplifier Parts and Drawings | 75 |
| APPENDIX B – Additional Measurements on First Iteration of Air Amplifier | 83 |
| APPENDIX C – Second Iteration of Air Amplifier – Parts and Drawings..... | 84 |
| APPENDIX D – Heating of the Mass Spectrometer inlet..... | 87 |

LIST OF FIGURES

| | |
|--|----|
| Figure 1-1. Example of mass spectrum | 1 |
| Figure 1-2. Mass Spectrometry workflow diagram..... | 3 |
| Figure 1-3. Working principle of quadrupole mass spectrometer..... | 4 |
| Figure 1-4. Analyzer cell of a FTICR [2]..... | 5 |
| Figure 1-5. Excitation and detection of ions in a Ion Cell (FTICR)..... | 6 |
| Figure 1-6. Conversion of signal from time domain to m/z in a FTICR..... | 7 |
| Figure 1-7. Working principle of linear ion trap mass spectrometer | 8 |
| Figure 1-8. Electrospray Ionization and desolvation process..... | 10 |
| Figure 1-9. Focusing ions using an aerodynamic device | 12 |
| Figure 1-10. Section view of a commercial air amplifier..... | 13 |
| Figure 1-11. Cross section of commercial air amplifier [21] | 14 |
| Figure 2-1. Aerodynamic model of the air amplifier | 15 |
| Figure 2-2. Section view of first iteration of air amplifier design..... | 16 |
| Figure 2-3. Exploded view of 1st iteration of air amplifier..... | 17 |
| Figure 2-4. Force diagram for first iteration of air amplifier | 18 |
| Figure 2-5. Belleville washer preload calculation..... | 19 |
| Figure 2-6. Design considerations to ensure axially symmetric flow | 20 |
| Figure 2-7. Coordinate System of Diamond Turning Machine ASG Rank Pneumo 2500 | 21 |
| Figure 2-8. Effect of error on vertical tool adjustment on machined radius | 22 |
| Figure 2-9. Effect of tool centering evaluation on cylindrical error..... | 23 |
| Figure 2-10. Tool centering for cylindrical turning [25]..... | 24 |
| Figure 2-11. Astigmatism error profile after 4th tool iteration of tool centering..... | 26 |
| Figure 2-12. Plot of X-error and x-command as a function of Z command for test plug machining on the ASG. | 26 |
| Figure 2-13. Machined surfaces (bold) and measurement chains on air amplifier | 27 |
| Figure 2-14. Tool holder used to machine top and bottom insert | 28 |
| Figure 2-15. Machining of inside diameter on base | 29 |
| Figure 2-16. Parallelism adjustment and annular gap measurement..... | 31 |

| | |
|--|----|
| Figure 2-17. Setup for Air Amplifier Piezoactuators Calibration Curve measurement | 33 |
| Figure 2-18. Relation between applied voltage and annular gap to top insert mating face | 34 |
| Figure 2-19. CMM machine used to measure annular gap indirectly | 35 |
| Figure 2-20. Diamond turning of critical surfaces and verification using New View (white light interferometer)..... | 35 |
| Figure 2-21. Setup for pitot tube pressure measurements | 37 |
| Figure 2-22. Effect of plenum pressure increase vs annular gap increase on pressure profile ... | 38 |
| Figure 2-23. - Schematic of setup for current measurement on MS skimmer cone | 39 |
| Figure 2-24. Setup for current measurement on MS skimmer cone..... | 40 |
| Figure 2-25. Skimmer cone current vs air amplifier position | 41 |
| Figure 2-26 - Abundance of 857 ± 1 m/z ions as a function of AA axial position shows that there is a peak of abundance..... | 42 |
| Figure 2-27 – Improvement of 4.34 folds of abundance measured for a ESI gap of 9mm (without and with AA)..... | 44 |
| Figure 2-28. Comparison of full factorial design vs fractional factorial design of different resolution | 47 |
| Figure 2-29. Half normal plot for FFD experiment..... | 49 |
| Figure 2-30. Mass spectrum comparison at 2 μ L/min with and without the air amplifier..... | 51 |
| Figure 3-1. Reduction of MS inlet tube length..... | 53 |
| Figure 3-2. Next air amplifier outline and FEA results for a plenum pressure of 45 psi | 55 |
| Figure 3-3. Simulation used to design custom made diamond tool and determine tool setup | 56 |
| Figure 3-4. Diamond turned surfaces (bold) and measurement chain on new design of air amplifier | 56 |
| Figure 3-5. Static Pressure Measurement for 2nd iteration of air amplifier..... | 58 |
| Figure 3-6. Pressure profile - 1 st vs 2 nd iteration..... | 59 |
| Figure 3-7. Maximum Vacuum vs Outlet Cone Length..... | 59 |
| Figure 3-8. Test bench to measure the effect of MS inlet cone on aerodynamic profile | 60 |
| Figure 3-9. Pressure at focal point as a function of gap between MS inlet and air amplifier | 61 |

Figure 3-10. Stagnation pressure measured 1 mm from commercial air amplifier outlet (Left: 3D representation; Right: 4 axis superposed)..... 62

Figure 3-11. Stagnation pressure measured 1 mm from Air Amplifier II (Left: 3D representation; Right: 4 axis superposed)..... 62

Figure 3-12. LTQ injection time data sample 63

Figure 3-13. Ion injection time comparison with regular capillary..... 64

Figure 3-14. Ion injection time as a function of air amplifier cone length..... 65

Figure 3-15. Full Factorial Design experiment results (sum of 19⁺, 9⁺ and 8⁺ of Cyt-C)..... 66

Figure 3-16. Total Ion Current as a function of flow rate at 3 mm ESI gap 68

Figure 3-17. Total ion current as a function of flow rate at 6 mm ESI gap 68

LIST OF TABLES

| | |
|---|----|
| Table 2-1. Results for tool centering calculation..... | 25 |
| Table 2-2. Maximum vacuum as a function of plenum pressure and annular gap width..... | 38 |
| Table 2-3. Representation of a resolution V fractional factorial design for 5 variables | 46 |
| Table 2-4. Variable definition for FFD experiments..... | 48 |
| Table 2-5. Variable combinations that were tested during second serie of experiment..... | 51 |
| Table 3-1. Full factorial performed on the second iteration of the air amplifier..... | 66 |

1. INTRODUCTION

1.1 Background Information

1.1.1 What is mass spectrometry?

Mass spectrometry is the analytical technique most widely used to measure the mass to charge ratio of molecules. Being able to quantitatively and qualitatively determine very precisely the mass of a molecule can ultimately allow its identification. It is therefore a powerful tool used in biology, pharmaceutical research, analytical chemistry and cancer research. For example, being able to detect very low concentration of a specific biomarker protein in a patient blood can lead to detection of cancer at earlier stage and eventually result in greater survival rates.

1.1.2 Abundance and mass to charge ratio

The typical output of a mass spectrometer is a mass spectrum chart where the X-axis represents the ratio of the mass-to-charge ratio (m/z) of the ions detected and Y-axis their abundance or intensity as shown Figure 1-1.

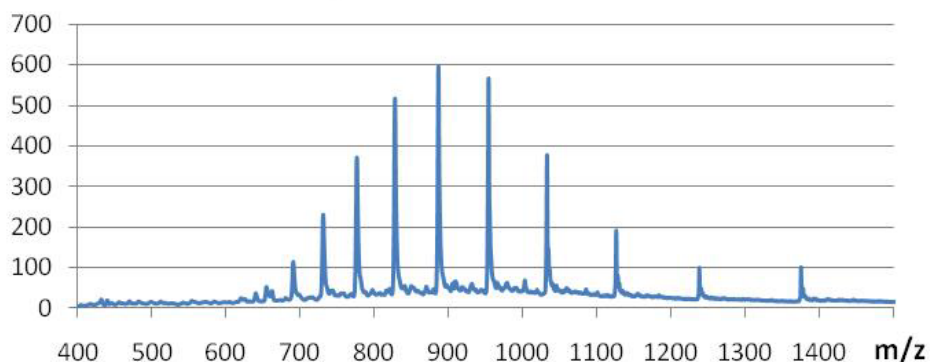


Figure 1-1. Example of mass spectrum

In the dimensionless mass-to-charge ratio (m/z), m is the unified atomic mass (in Dalton) and z is the number of elementary charges. Exact value of 1 Dalton is defined as 1/12 of the mass of the most abundant Carbon isotope (carbon 12), meaning that each proton will have a

mass of approximately 1 Da. For example, $C_7H_7^{2+}$ ions will have a mass of 91 Da and an elementary charge of 2 for a mass to charge ratio of 45.5.

$$C_7H_7^{2+} \rightarrow (7 \times 12_{\text{protons+neutrons}})_{\text{carbon}} + (7 \times 1)_{\text{protons}(H^+)} = 91\text{Da} \quad (1.1)$$

Abundance is proportional to the number of ion of that specific m/z detected by the mass spectrometer for a time period. However, due to the working principle of the instruments (described in more details in next section), it is not possible to relate that abundance value to a specific number of ions detected by the instrument. For that reason, it is very difficult to compare intensity measurements performed on 2 different instruments. Therefore, the most reliable figure of merit to compare the effect of the variation of some parameters on the performance of the instrument is to compare absolute intensity of subsequent measurement performed with the same instrument.

1.1.3 Mass spectrometer instrument

Mass spectrometer instruments use electric and/or magnetic field to measure the mass to charge ratio of molecules and their abundance. Figure 1-2 presents the workflow diagram with the typical components of modern mass spectrometers. Ion source is often interchangeable on mass spectrometer instrument. For the Air Amplifier project, only electrospray ionization was used and this ionization technique is described in detail in Section 1.1.4. Instruments with different mass analyzers and ion detection mechanisms are commercially available and each of them have their own set of advantage and disadvantage. Three types of mass spectrometer instrument were used in this project: a triple quadrupole mass spectrometer (QqQ), a Fourier Transform Ion Cyclotron Resonance Mass Spectrometer (FTICR or FTMS) and finally a hybrid instrument combining a FTICR with a Linear Ion Trap Mass Spectrometer (LTQ-FTMS). A brief description of the working principle of these instruments is presented in this section:

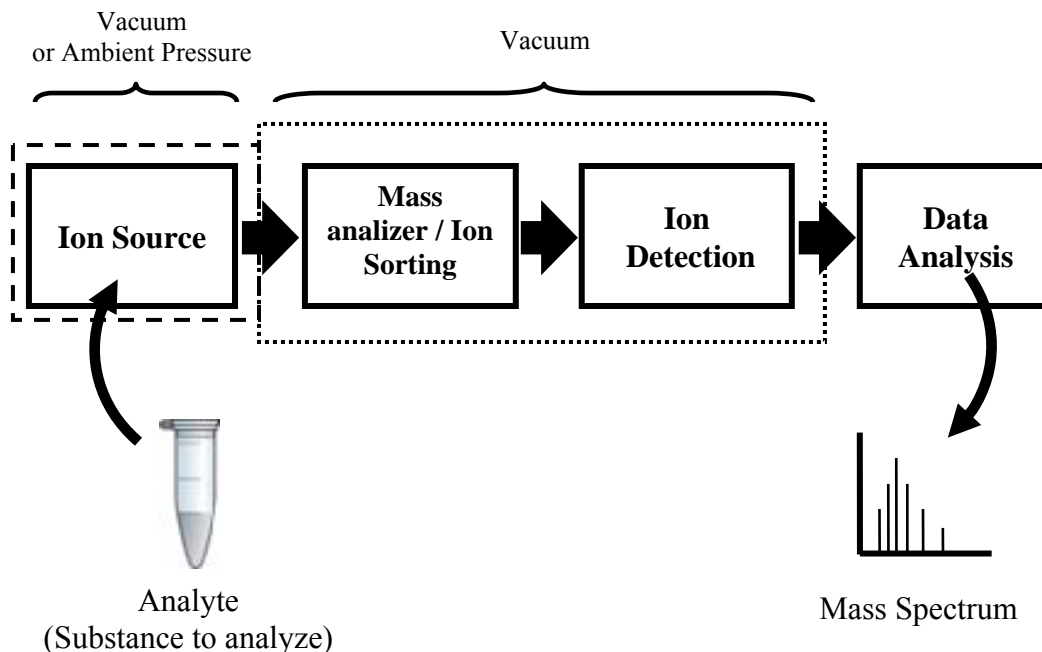


Figure 1-2. Mass Spectrometry workflow diagram

Triple Quadrupole Mass Spectrometer (QqQ)

In linear quadrupole instrument, quadrupoles are used to sort the ions according to their mass to charge ratio [1]. As shown on Figure 1-3 A), ions injected from the source are travelling under vacuum between two sets of opposite rods that are excited with a combination of DC voltage (U) and AC voltage (V). Figure 1-3 B) shows a typical Mathieu stability diagram for a certain m/z ratio. If the combination of DC and AC voltage within the stable zone for the ion, it will travel through the quadrupole and reach the ion detection plate where they neutralize. Current generated by ions neutralizing is analyzed and converted into an ion abundance value. It is therefore possible to measure only a specific m/z or, as shown on Figure 1-3 C), scan over a specific range of m/z by changing U and V as a function of time and generate a mass spectrum for that specific m/z range. As slope of the scan line gets smaller, stability regions of different m/z ions are overlapping and resolving power decreases. Ultimately, at low DC voltage, all ions are stable and the quadrupole is said to be in RF-

only or ion guide mode. This mode is widely used in mass spectrometer instruments to guide ions from different instrument sections.

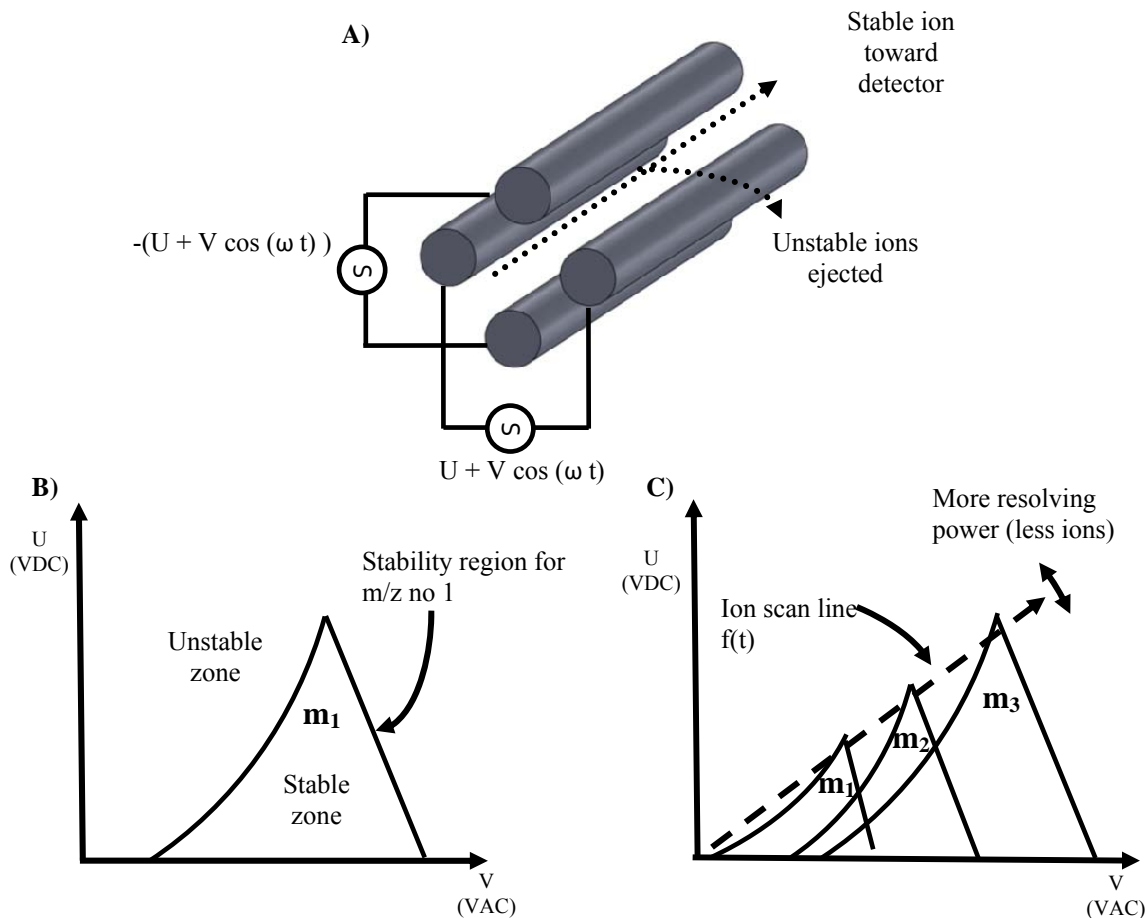


Figure 1-3. Working principle of quadrupole mass spectrometer

With multiple quadrupoles, it is possible to perform multiple steps of ion selection and fragmentation by introducing collision gas in one of the quadrupole. However, for the air amplifier experiments, only one of the quadrupole was used to select the m/z range to be analyzed and the two others were used as ion guides only. Linear quadrupole instrument typically have lower resolving power and a limited scan range. On the other hand, they are robust, compact, versatile and have a short analysis time.

Fourier Transform Ion Cyclotron Mass Spectrometer

As linear quadrupole instruments use electric fields to sort the ions of different m/z , a FTICR uses a combination of magnetic fields and electrical fields to separate the ions [2]. A pack of ions is first guided using quadrupoles from the ion source to the analyzer cell of the instrument. By controlling the potential at both end plates of the cell, the ions are trapped and forced to travel back and forth axially in the analyzer cell (see Figure 1-4). A large magnetic field in the axial direction of the analyzer cell (9.4 Tesla in the instrument used here) is then used to sort the trapped ions according to their mass to charge ratio.

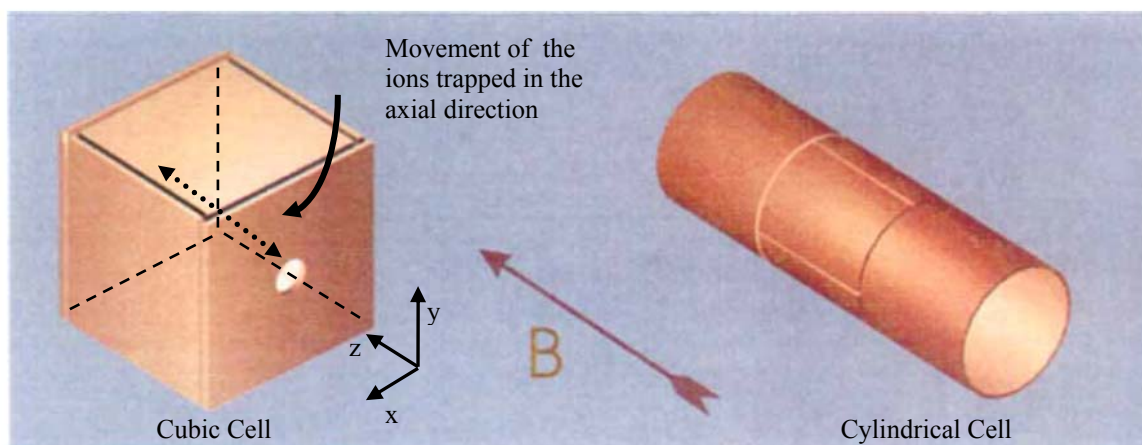


Figure 1-4. Analyzer cell of a FTICR [2]

Indeed, the analyzer cell walls consist of plates made of highly conductive material and are electrically insulated from each other. Opposite faces of the cells serve the purpose of either trapping (Z-direction), exciting (X-direction) or measuring the ions (Y-direction). Initially all ions are travelling back and forth in the center of the cell. An excitation potential along X-axis will force the ion to travel radially. Lorentz force (left of Figure 1-5) will then cause the ions to start rotating around the centerline (cyclotron motion) and frequency of rotation will be a function of the m/z ratio as Equation (1.2).

$$f_c = \frac{Bz}{2\pi m} \quad (1.2)$$

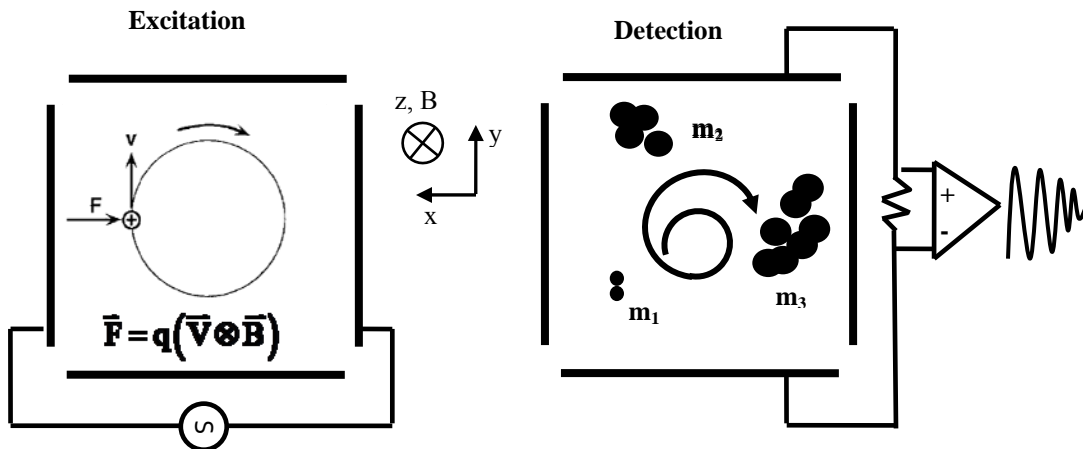


Figure 1-5. Excitation and detection in an ion cell (FTICR)

In the detection phase (right of Figure 1-5), difference in potential between upper and lower detection plate caused by movement of charged ions inside the cell are measured over a set period of time. Process through which the mass spectrum is obtained from the raw signal is showed on Figure 1-6. First, amplified raw signal or transient signal on the time domain is converted to the frequency domain using Fast Fourier Transform (FFT). Using Equation (1.2), frequency response is then converted in signal abundance vs m/z spectrum. Abundance scale is function of internal gain and calibration constants and cannot be interpreted as an absolute number of ions being measured. FT-ICR instruments have the greatest resolving power and sensitivity of all mass spectrometer instruments. However, they are also significantly more expensive due to the large magnet components and the pumping system needed to maintain the high vacuum necessary to extend their mean free path enough measure them for long period of time (second range). FT-ICR are often used in tandem instrument such as the Linear Ion Trap FT Mass Spectrometer.

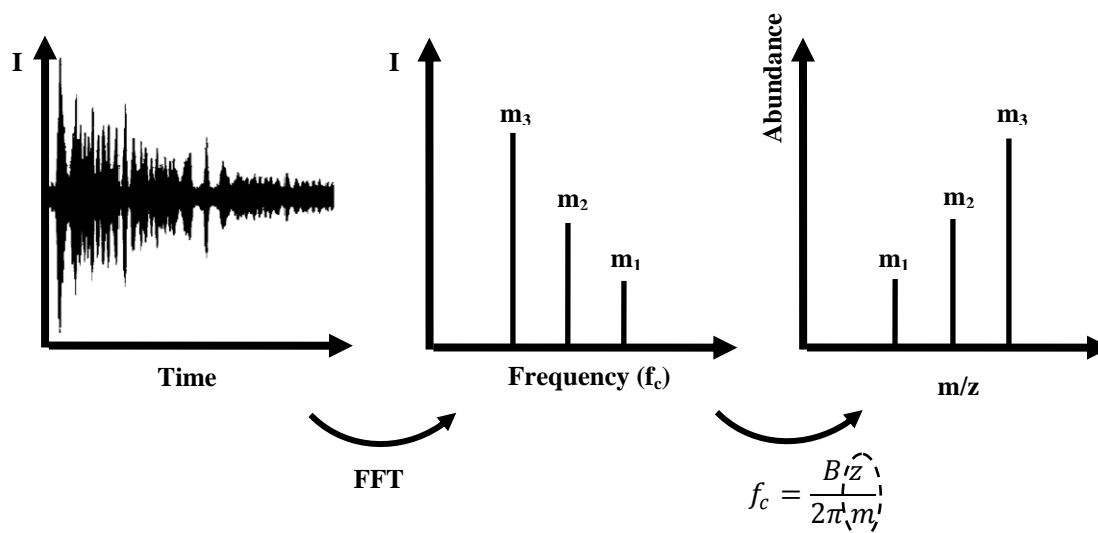


Figure 1-6. Conversion of signal from time domain to m/z in a FTICR

Linear Ion Trap Mass Spectrometer Fourier Transform Mass spectrometer (LTO-FTMS)

This type of instrument is a tandem instrument meaning that the back end is a FTMS instrument as described before. The front end is a linear ion trap. In this type of instrument (see Figure 1-7), ions from the ion source are accumulated in the trap and forced to travel back and forth on the centerline. Using combination of electrical fields [3], ions of specific m/z can be destabilized and sent toward a detector. As with the linear quadrupole instrument (QqQ), it is possible either to measure only a specific m/z ion or to scan and measure over a wider m/z range. Alternatively, specific ions can be sent toward the FTMS for higher resolving power measurement. When used for the Air Amplifier project, only the linear ion trap was used. As discussed later, it is possible to set the amount of trapped ion to a fixed value using the Automatic Gain Control feature (AGC). The time necessary to fill the trap can therefore be used as a figure of merit to compare the flow of ion getting in the instrument. Unfortunately, this gain value does not represent an absolute number of ions.

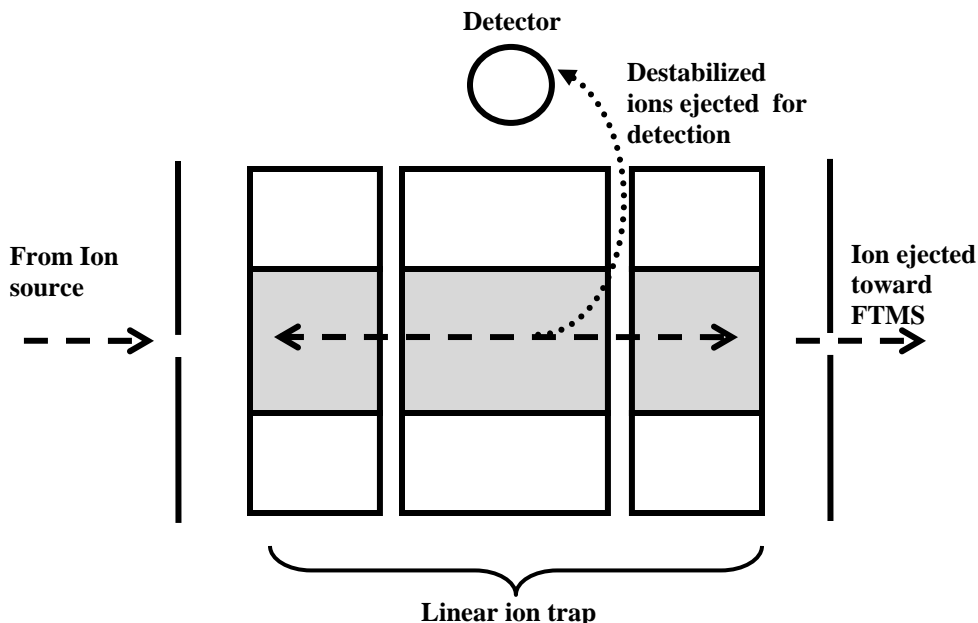


Figure 1-7. Working principle of linear ion trap mass spectrometer

1.1.4 Electrospray ionization

As discussed earlier, prior to be analyzed by the mass spectrometer, ions must first be put into gas phase using an ion source. Over the years, several methods have been developed and studied to move the ions from the liquid phase to the gas phase like fast atom bombardment (FAB), plasma desorption, laser desorption, corona discharge ionization, etc. However, one of the preferred methods for the analysis of large molecules is the electrospray ionization (ESI) [1]. ESI-MS was first developed by Yamashita and Fenn at Yale in 1984 [5-8] and allow large ions to be transferred directly to gas phase. ESI is known to be a relatively “soft” ionization technique, meaning that the energy transferred to the molecules during the ionization process is relatively small, reducing the risk of fragmentation of the molecules. A soft ionization technique allows the identification of larger molecule such as proteins and even proteins with weaker molecular chemical bonds (ex. non-covalent complex). Fenn received the Nobel Prize in chemistry for 2002 for his work on the ESI.

In ESI, analyte (sample being analyzed) is dissolved in a buffer solution consisting of a solvent often mixed with a low concentration of acid (to increase the number of ions in solution). The solution is pushed through a capillary which is connected to the ESI emitter tip, consisting of a metallic ferrule and a capillary extension with a precise ID as seen in Figure 1-8. Flow is very low, typically on the order of 0.1 to 100 $\mu\text{l}/\text{min}$. The ESI emitter tip is positioned few millimeters from the mass spectrometer inlet and an electrical potential between the ferrule and the mass spectrometer inlet is applied. The resulting electrical field causes a separation of the charge in the solution, increasing the concentration of H^+ near the end tip of the capillary (in case of positive ESI) as shown on enlarged view of the figure. The axial Coulomb force on the positive ions is eventually be large enough to deform the dilution surface which is held together by surface tension and form a cone. The shape of the Taylor cone will then be governed by a dynamic equilibrium between the surface tension on the protruded surface and the coulombic repulsion between the charged particle. As the field increases, the cone stretches and the radius of the tip decreases up to a point where the repulsive force between the ions will overcome the surface tension. This threshold is known as the Rayleigh limit of stability also shown in Figure 1-8. Passed that limit, a thin jet of highly charged droplets containing the analyte will be ejected from the tip of the cone.

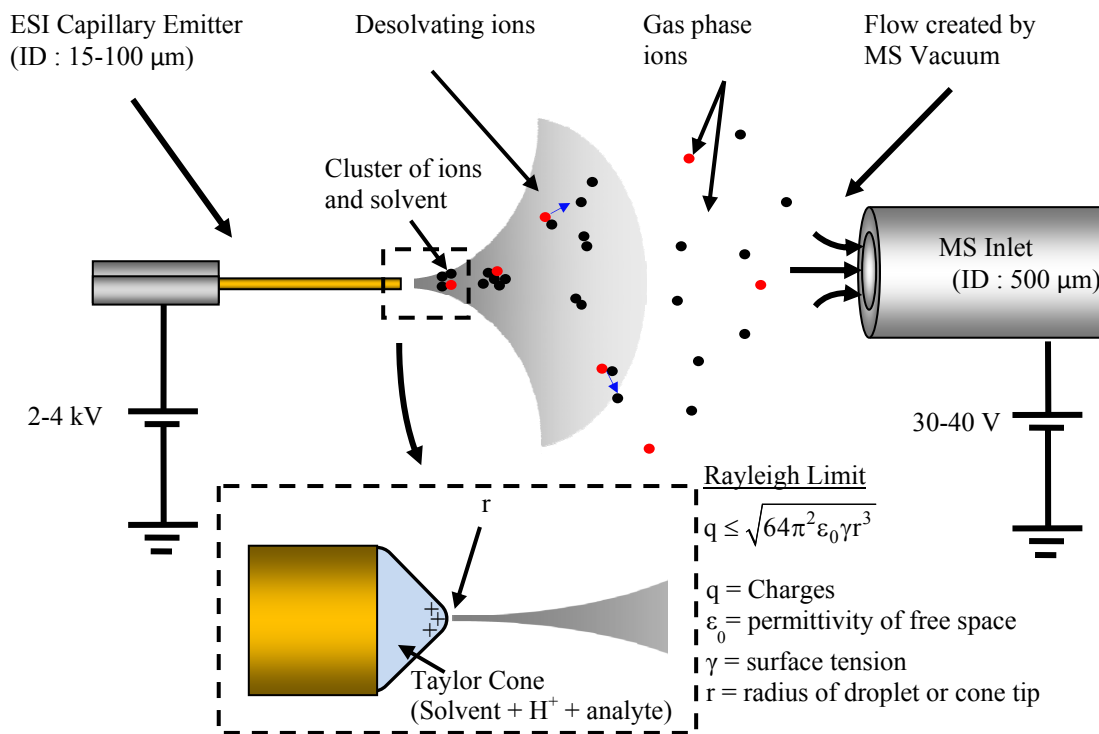


Figure 1-8. Electro Spray Ionization and desolvation process

The process by which gas phase ions are ejected from the charged droplet is not fully understood but two main models have been proposed. The first one, called the *charged residue model* (CRM), was put forward by Dole and coworkers [10]. According to this model, solvent will evaporate from the droplets and as they become unstable in the vicinity of the Rayleigh limit, fission will occur and smaller charged droplet will be created. This process will go on until droplets carry a single charged molecule of the analyte (can be multiple charges on the molecule). The rest of the solvent evaporate, leading to the formation of a gas-phase ion. The second mechanism, the *ion evaporation mechanism* (IEM), was presented by Iribarne and Thompson [11]. They suggested that when solvent evaporates and droplets have reached a critical size ($< 10\mu\text{m}$), the gas-phase ions can be ejected directly from the charged droplets instead than undergoing fission. It is important to understand the creation of singular ions during electro spray does not occur instantaneously at the tip of the capillary, but result from complex interaction between the size of the analyte molecule, the

flow rate, the nature of the solvent, the intensity of the electrical field, the concentration of the analyte in the solvent, temperature, etc. Desolvation process also continues inside the MS inlet capillary.

The efficiency of the ESI-MS does not only depend on the ability to create gas-ions from liquid analyte, but also depends on the efficiency of the transmission of these ions to the mass spectrometer. As gas phase ions produced during electrospray ionization are the same polarity they scatter away due to coulombic repulsive force, reducing significantly the number of ion captured by the mass spectrometer inlet. One approach to increase the number of ions getting in the air amplifier is to use a Venturi device or an air amplifier to aerodynamically focus the electrosprayed ions toward the inlet of the mass spectrometer inlet. The goal of the work presented in this thesis is to design, fabricate and test the performance of an aerodynamic focusing device, the air amplifier, as a method to increase the number of ion transferred to the mass spectrometer.

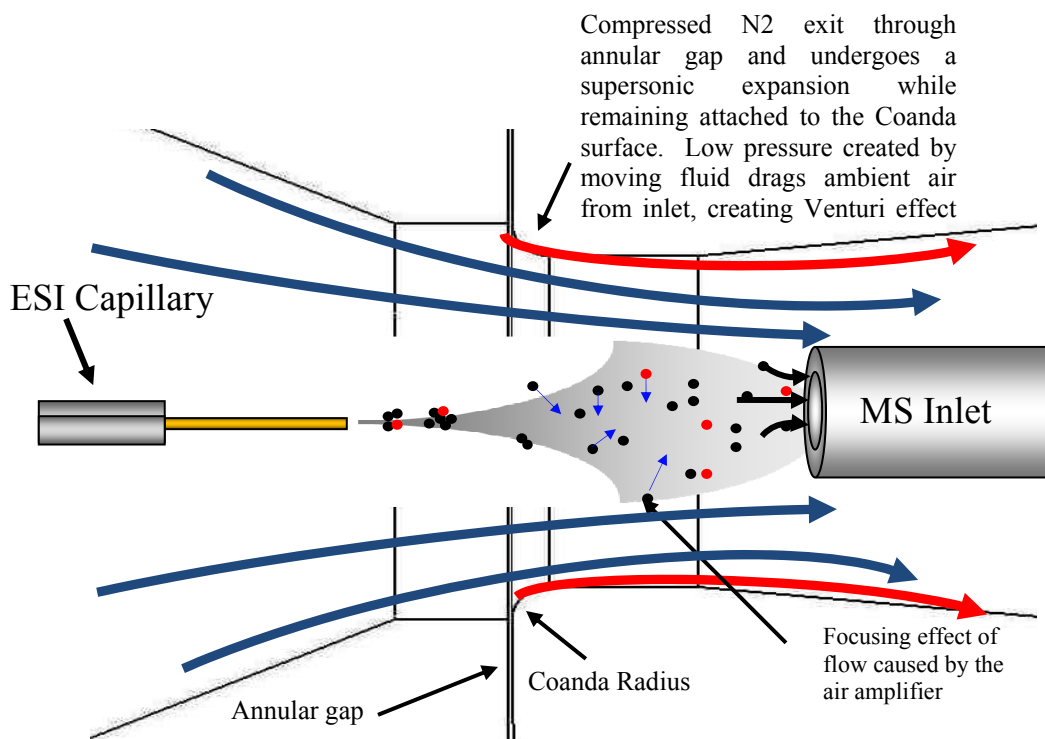


Figure 1-9. Focusing ions using an aerodynamic device

1.2 Previous work

To focus these scattering ions and therefore increase the number of ions captured by the mass spectrometer, method using electrical fields [13-17] and air flow [18-20] have been attempted and tested. These methods all showed improvements in ion abundance. Ion funnels, using a stack of coned shaped RF ring to focus the scattering ions toward the mass spectrometer inlet is now a device commercially available and offer some signal improvement. Apollo II® ESI source (Bruker, Billerica, USA), a ion funneling source claims 10 folds signal improvement on their original press release. Using aerodynamic devices such as an air amplifier to focus the ions has demonstrated comparable signal improvement [20] and ultimately, such device shows the potential to be a more robust and less expensive solution.

Attempts made with an air amplifier so far used a commercially available device. Due to its work principle, discussed in more details in Section 2, air flow control in an air amplifier is

very sensitive to annular gap adjustment or the gap controlling the flow of pressurized air. As shown on see Figure 1-10, commercial devices offer only limited adjustment. Indeed, the gap is adjusted by rotating a threaded insert and it is impossible to measure the annular gap. Also, geometry and alignment of annular gap are important factors as they affect the focusing capability of the device [21]. To efficiently focus the ions, it is imperative to have a flow distribution that is radially uniform. A non uniform gap or any imperfection in the air amplifier geometry will result in an asymmetric flow that can have the adverse effect and deflect the charged droplets away from the mass spectrometer inlet instead of focusing them. Early simulation performed by computational fluid dynamic show an asymmetrical velocity profile in the cross section of an air amplifier with geometric imperfections (Figure 1-11). As there is no way to precisely control or know the annular gap, it is extremely difficult to produce repeatable results, to characterize its performance in a defined experimental space and therefore find basis for improvement.

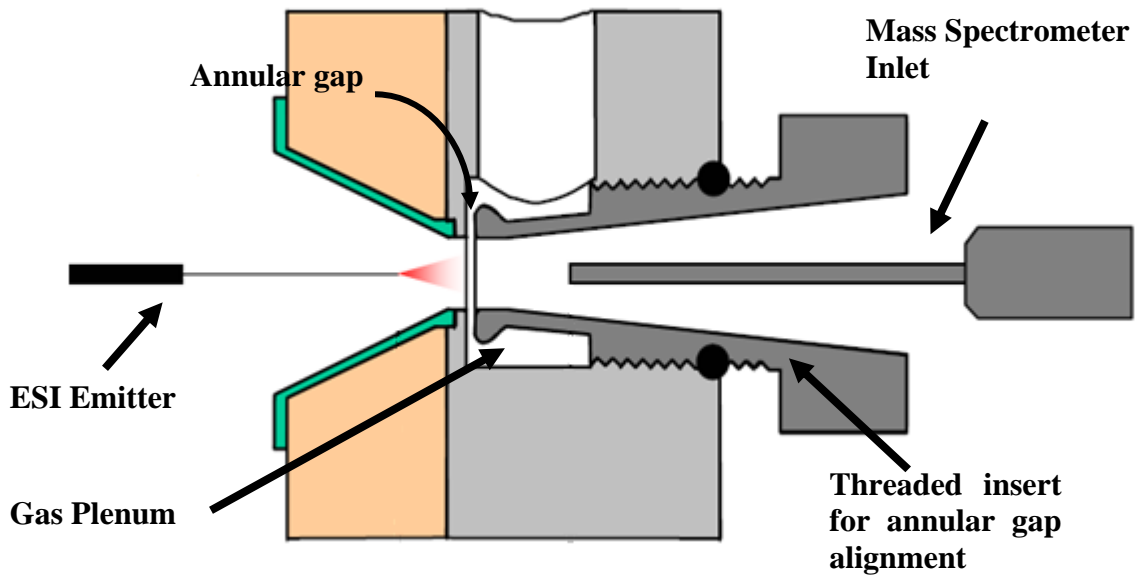


Figure 1-10. Section view of a commercial air amplifier

To better describe the effect of geometry on air flow and to improve the device, computational fluid dynamic simulations were developed by the Aerospace Engineering Computational Fluid Dynamics Laboratory (AECFDL) at North Carolina State University.

The software package used is a Navier-Stokes solver called REACTMB-MP that was developed in their laboratory. Preliminary results corroborated the 8 folds improvements previously obtained with the air amplifier [20-21] with a specific geometry and an annular gap width of 60 μm that was estimated from a commercial device. To improve the control on the annular gap adjustment and better understand and characterize the effect of the air amplifier on mass spectrometry, a precision engineered device with uniform and precisely adjustable annular gap is needed.

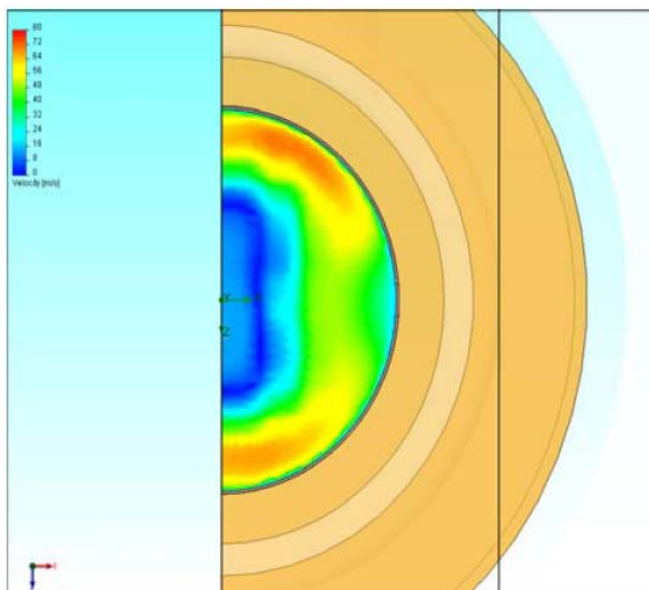


Figure 1-11. Cross section of commercial air amplifier [21]

1.3 Problem Statement

A commercially available air amplifier was used as a focusing device to improve signal and detection limit in ESI mass spectrometry. Precision engineering principles will be used to design and fabricate a new iteration of this device. Through air flow and mass spectrometer measurements, a series of experiments were used to study the effect of different parameters of the air amplifier on signal abundance. Results were used to improve the design, fabricate a second iteration and describe the experimental space where the best results can be obtained.

2. AIR AMPLIFIER I

2.1 Design

The Aerospace Engineering Computational Fluid Dynamics Lab worked together with the Precision Engineering Center to develop the first iteration of the surface profile that was suitable from both fabrication and performance points of view. The first calculations of the gas dynamics of the flow within the air amplifier devices was performed using a computational fluid dynamics code called REACTMB. The air amplifier uses the Coanda effect (tendency of a fluid to remain attached to a smooth curved surface) to create the Venturi effect. More precisely, the compressed nitrogen exits through an annular gap and undergoes a supersonic expansion while remaining attached to the Coanda surface. Low pressure created by moving fluid entrains ambient air from inlet, creating Venturi effect and ion focusing. Figure 2-1 shows the velocity plot and streamline of gas being entrained at the Coanda radius region (left). Focusing effect of the air amplifier is showed on the right where concentration of analyte (modeled as droplets) between ESI tip and MS inlet is plotted as well as the droplet streamlines.

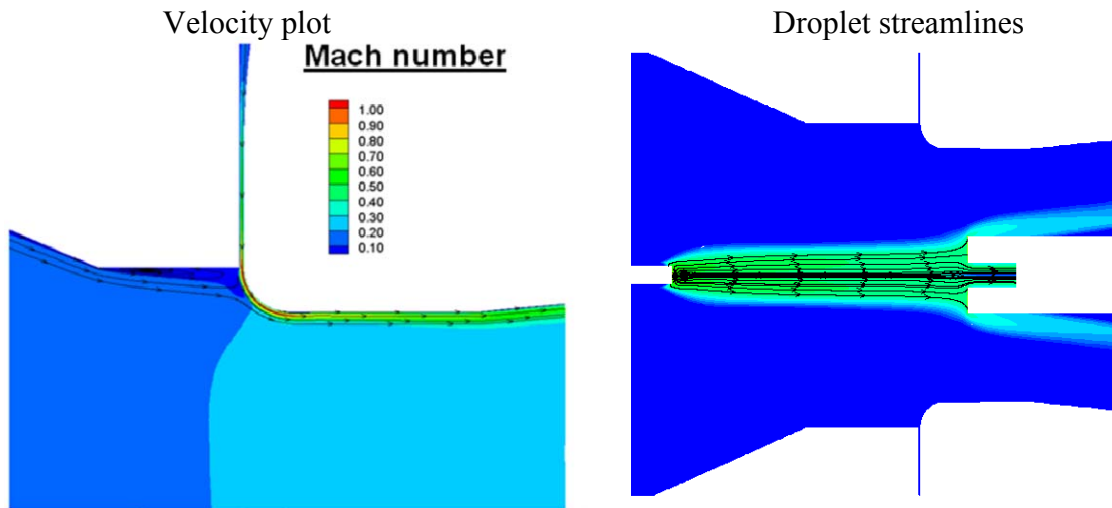


Figure 2-1. Aerodynamic model of the air amplifier

The hypothesis for efficient Coanda based geometry air amplifier operation is its sensitivity to the gap width. To determine experimentally the optimal annular gap, the device gap is controlled using 3 D1CM20 PZT actuators from Kinetic Ceramics. CFD modeling helped to determine that the Venturi effect and eventually ion focusing was obtained with an annular gap in the range of 50-70 μm . A section view of the first design showing the geometry of the aerodynamic profile as well as the principal parts is presented in Figure 2-2. Another design criterion was to have the possibility to test other Coanda profiles without having to fabricate an entirely new device. For that purpose, the top and bottom inserts were designed to be interchangeable parts. 6061 aluminum was selected as material in reason of its machinability and resistance to chemical corrosion. Exploded view of the assembly is presented on Figure 2-3.

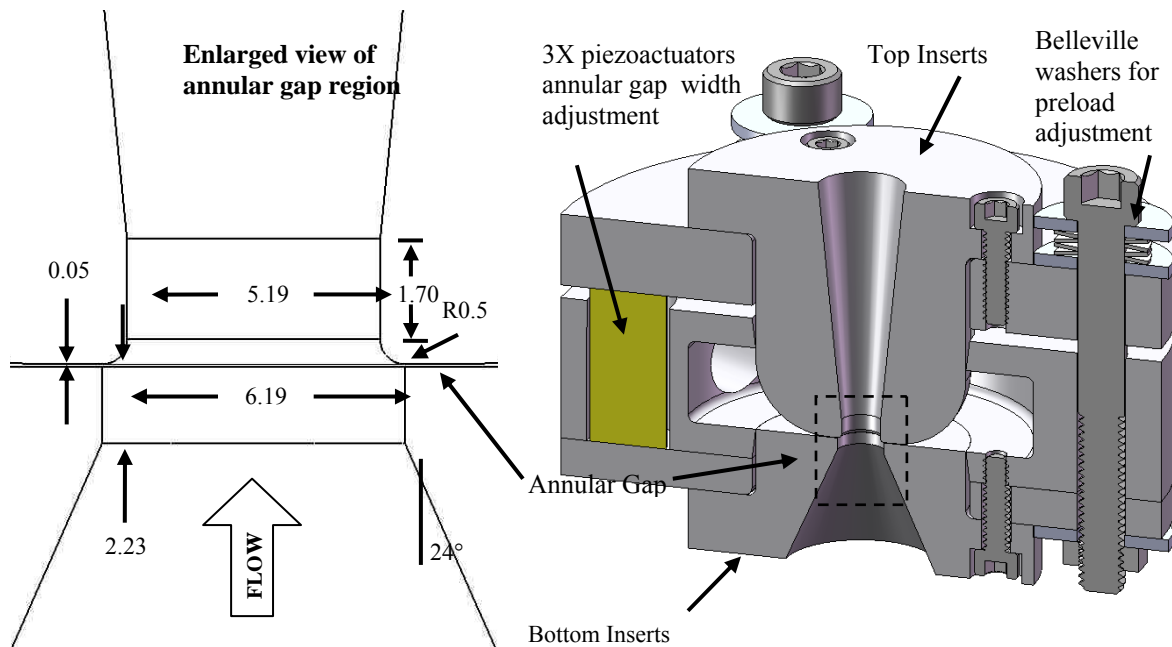


Figure 2-2. Section view of first iteration of air amplifier design

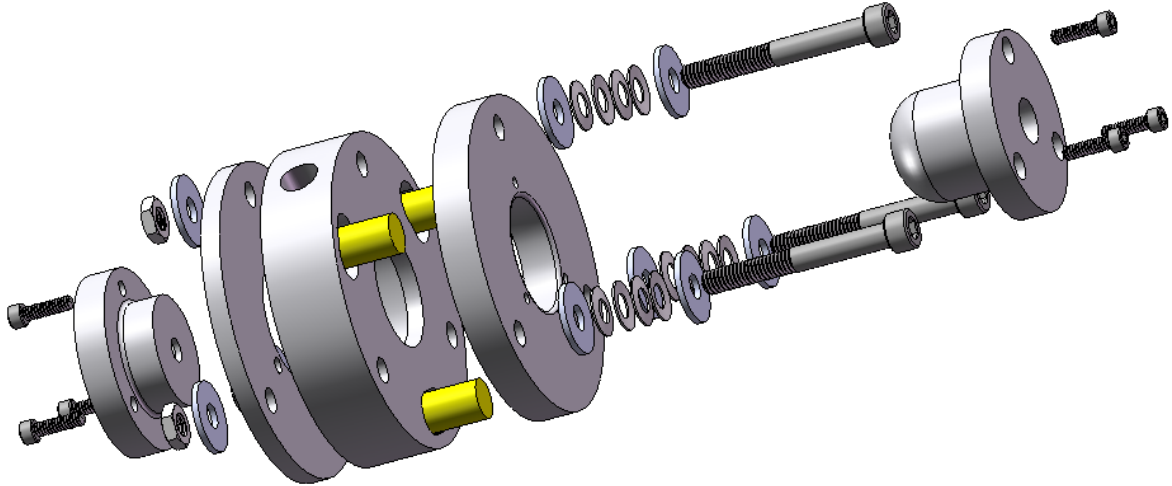


Figure 2-3. Exploded view of 1st iteration of air amplifier

The assembly is bolted together using Belleville washers to allow the actuators to change the annular gap while preventing the plenum pressure to change that gap. Because maximum operation pressure is 45 psi (310 kPa), so force generated by pressure is 190 N ($310 \text{ kPa} \times 615 \text{ mm}^2$) as shown in Figure 2-4. Choosing a conservative total preload of 400 N, each Belleville stack preload will have to be larger than 133 N. As rated force generated by each PZT stacks is 2800 N, preload will not prevent the actuation of the annular gap.

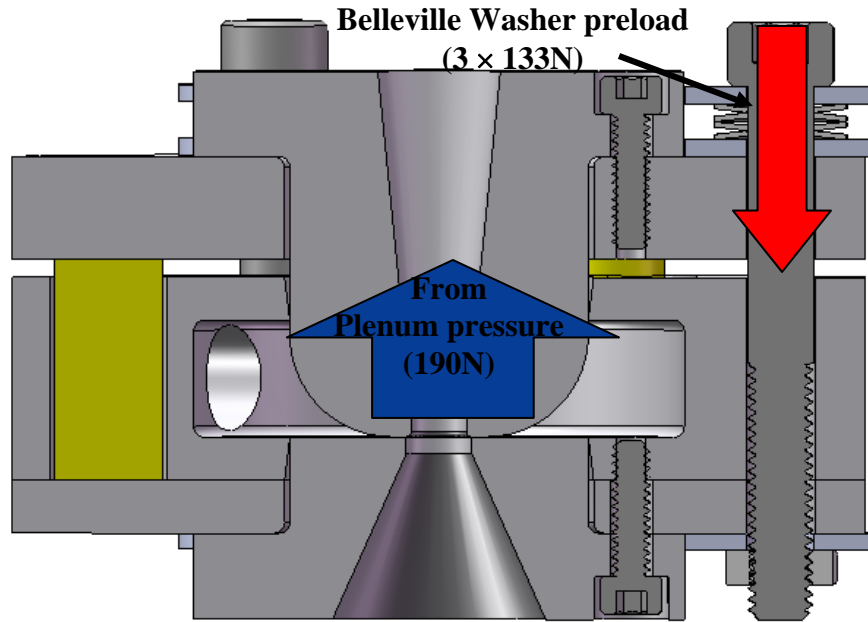


Figure 2-4. Force diagram for first iteration of air amplifier

The relation between load (P) and deformation (δ) in a Belleville spring is not linear due to the significant changes in shape during deflection. This relation is expressed by Equation (2.1) where E is the Young's modulus and ν is Poisson's ratio.

$$P = \frac{E\delta}{(1-\nu^2)Ma^2} \left[(h-\nu) \left(h - \frac{\delta}{2} \right) t + t^3 \right] \quad (2.1)$$

The force-deflection relation for Belleville spring used for the assembly is presented on Figure 2-5. Dimension of Belleville spring used can be found in APPENDIX A – First Iteration Air Amplifier Parts and Drawing.

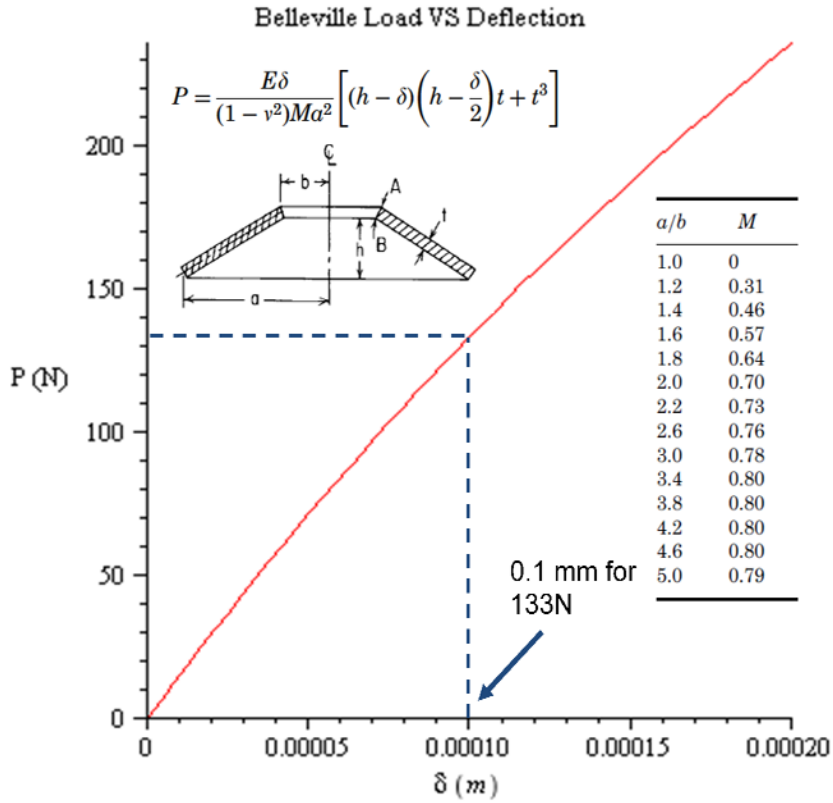


Figure 2-5. Belleville washer preload calculation

Deformation due to the required preload for a single Belleville Spring is 0.1 mm. To facilitate assembly and control on preload adjustment, a stack of four Belleville Springs were used, increasing the total deflection to a more convenient 0.4 mm for the same preload.

It was stated earlier that the main issue with the commercial amplifier design is the lack of control on the annular gap width, potential misalignment and other geometric defects on the Coanda surfaces that could lead to improper focusing of the ions. As parts are turned on a diamond turning machine, radial or rotational symmetry is ensured. However, one of the principal concerns is the possible radial misalignment between top and bottom insert as these two features are machined on separate parts and the concentricity rely on the precision of the assembly of these parts. To ensure proper radial alignment between top and bottom insert, a

design clearance of 1-2 μm (shown on Figure 2-6) is to be maintained between the inserts and the base.

The last important aspect that has to be considered is the parallelism between the 2 inserts that would result in a non-uniform annular gap. Some lack of parallelism is expected as there is a difference between piezoelectric stack heights. To ensure that parallelism between the 2 faces remains below 1 μm for the entire annular gap surface, 12 μm stainless steel shims (McMaster part no.19875A3) were added between top plate and piezoelectric stacks.

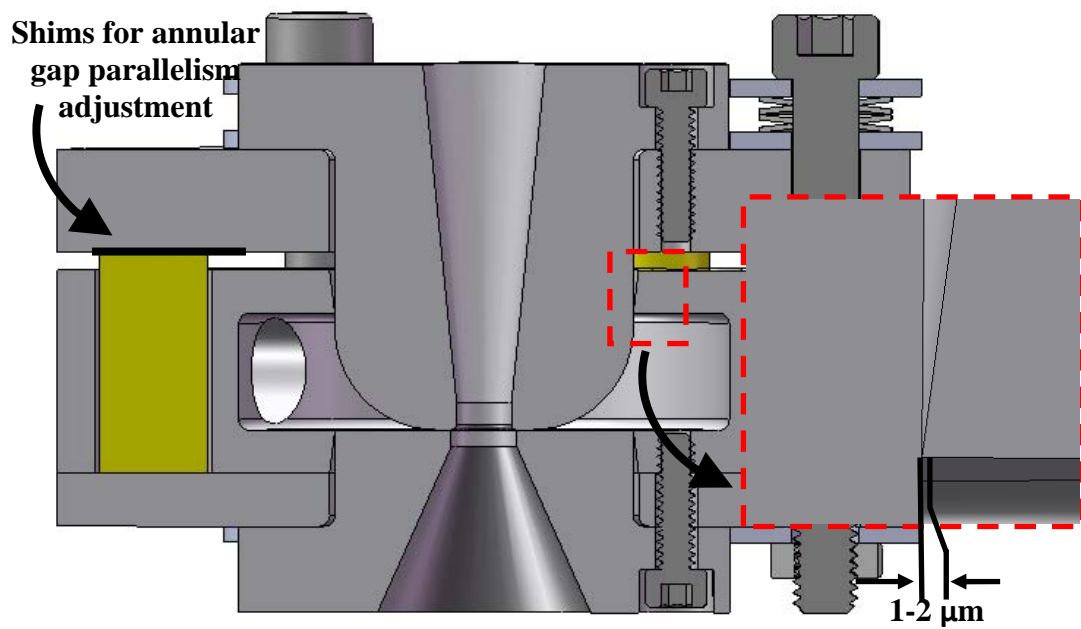


Figure 2-6. Design considerations to ensure axially symmetric flow

2.2 Fabrication

Rough machining of the first iteration of the air amplifier was performed by an external machine shop using CNC machine, leaving extra material for the final machining using a single point diamond turning machine at the PEC.

2.2.1 Setup and Tool Centering

The diamond turning machine (DTM) used for the final machining of the air amplifier is an ASG 2500 from Rank Pneumo. Tool coordinate system as well as general layout of machining setup is presented in Figure 2-7. Note that directions of positive axis are presented in the tool coordinate system. Hydrostatic oil bearings allow precise tool positioning of both X and Z axis. The work piece rotates on an air bearing spindle. Its in-house controller allows a resolution of the tool position of 2.5 nm and as a result the dimension of the parts can be fabricated better than 1 μm accuracy. The Y axis is fixed so tool height adjustment must be performed manually.

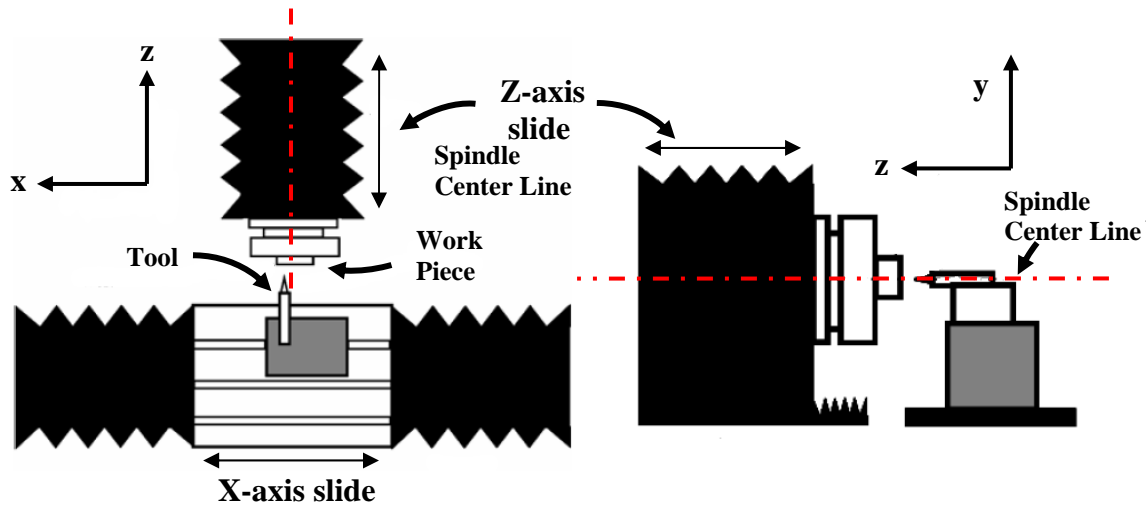


Figure 2-7. Coordinate System of Diamond Turning Machine ASG Rank Pneumo 2500

It is achieved by machining a flat in a test plug (acrylic) and then measuring the diameter of the feature left on the tool with an interferometer [22-23] that results from the difference between tool high and spindle centerline. In case of cylindrical turning, effect of vertical tool error on the final radius of the part is negligible for small error on vertical tool position (ΔY_{error}) and relatively large diameters (see Equation (2.2) and Figure 2-8 for geometry). For example, for a ΔY_{error} of 5 μm , it represents an error of 0.3 nm on a 19 mm nominal radius part. Sign of error depends if a ID or a OD is machined.

$$r_{error} = \sqrt{r^2 + \Delta Y_{error}^2} - r \quad (2.2)$$

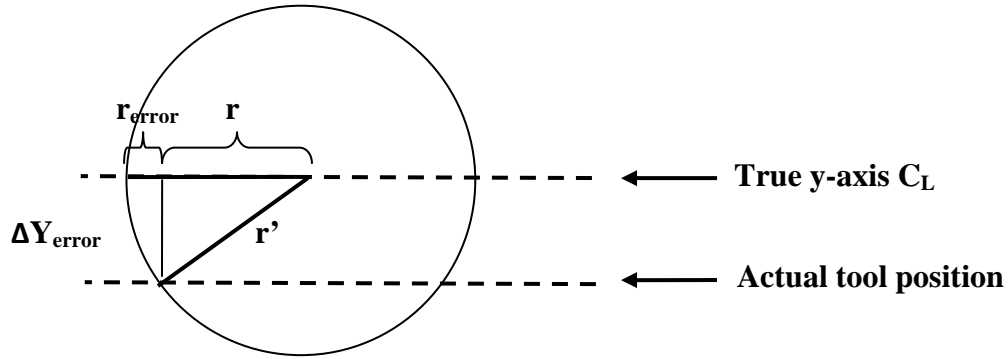


Figure 2-8. Effect of error on vertical tool adjustment on machined radius

To achieve the required cylindrical clearance of 1-2 μm the design is asking for, the laser interferometer used for axis positioning on the x-axis can be used to control the diameter of the parts. In case of cylindrical turning, this means that position of tool center on the spindle along the x axis has to be known to a high level of accuracy. To expose this technique, suppose 2 parts (one OD and one ID) have to be machined at the exact same radius r (see Figure 2-9). If coordinates of tool center are known ($CL_{x\text{-coord}}$), the tool position coordinates to machine an ID and OD of radius r (respectively $ID_{x\text{-coord}}$ and $OD_{x\text{-coord}}$) can be calculated using Equation (2.3).

$$\begin{aligned} ID_{x\text{-coord}} &= CL_{x\text{-coord}} - (r - r_{tool}) \\ OD_{x\text{-coord}} &= CL_{x\text{-coord}} + (r - r_{tool}) \end{aligned} \quad (2.3)$$

However, machining the OD and ID requires the tool tip to be positioned on both sides of the spindle centerline, any error (δ) in tool centering will result in a diameter difference of 4δ between the ID and the OD, resulting in a theoretical concentricity error of 2δ between both parts. This demonstrates the sensitivity of tool center line position ($CL_{x\text{-coord}}$) in determinint the absolute diameter of cylindrical part.

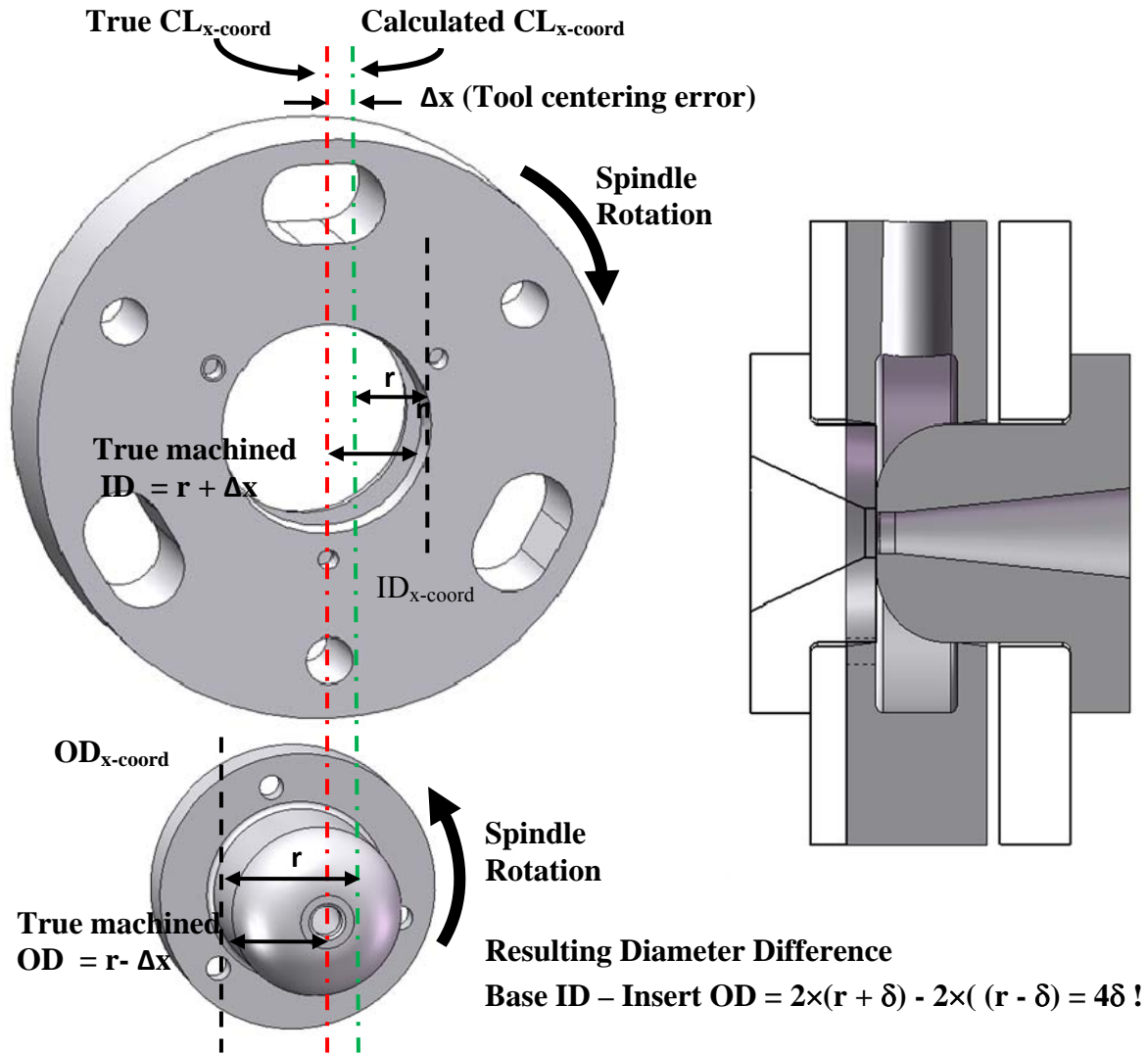


Figure 2-9. Effect of tool centering evaluation on cylindrical error

To find the tool centerline along the x-axis ($CL_{x-coord}$), a rough centering method commonly used at the PEC called the *Two circle method* [22] was used. After rough centering, error on tool centerline position is about 10 μm .

To determine more precisely the tool center position on the X axis, a common method is to measure the ogive error [24]. This method is particularly useful to find tool center needed to machine optical surfaces where the spindle centerline is included in the tool path. In case of

cylindrical turning, as the surface of interest is the outside or inside diameter of the part, it might not even be possible to machine through the part centerline and use the ogive error method. Even if it is possible, using this method could lead to significant error as tool radius section used to determine the centerline would be different than the one used to machine the critical surfaces. For the Air Amplifier, a tool centering method was developed by A. Sohn [25]. According to this method for cylindrical turning, if a circular path is machined on the outside diameter of a test plug and center of the interpolated radius (R_i) is different from the turned radius (R_t), a toroid shape will be produced (see Figure 2-10). The difference between the 2 radii of curvatures (Δx) represents the centering error. The deviation between these 2 radii (δ) over a given aperture (D) can be measured directly with a laser interferometer as it corresponds to the magnitude of the astigmatism (4th and 5th terms of Zernike serie). Δx can be derived R_i , D and the magnitude of the astigmatism (δ).

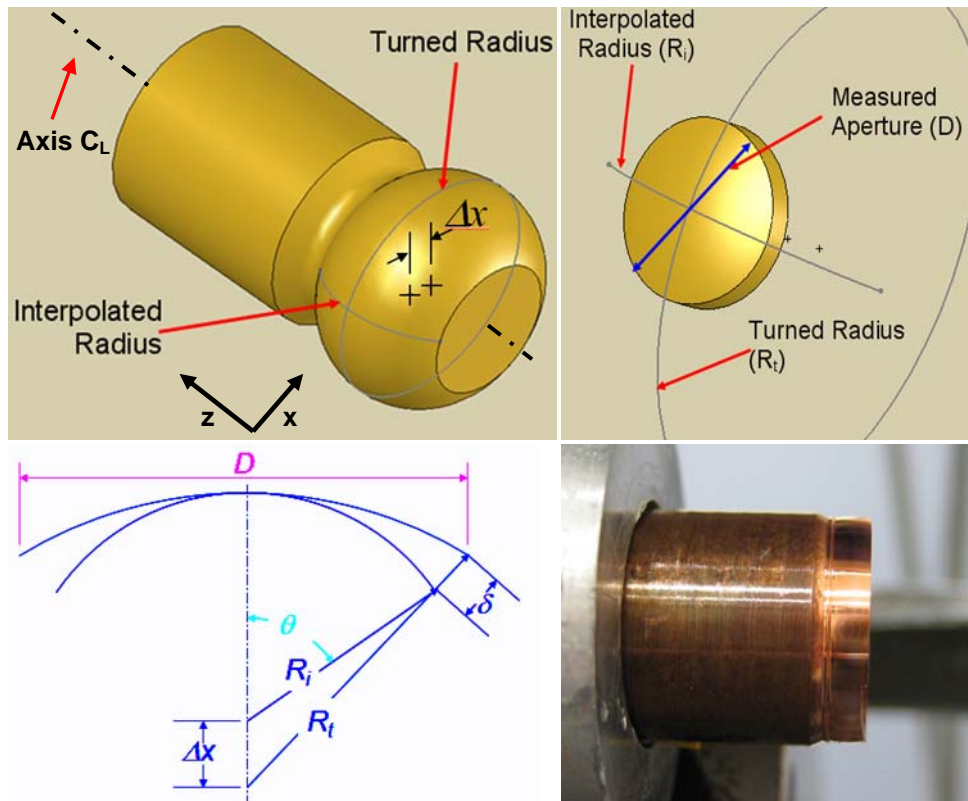


Figure 2-10. Tool centering for cylindrical turning [25]

A Zygo GPI XP interferometer with MetroPro analysis software was used to measure the In To test the method, a 12 mm diameter copper rod was used to machine a test plug. A program was written so that tool performs a circular radius R_i in the X-Z plane. R_i was purposely made larger than R_i by offsetting the centerline for the interpolated radius. By doing so, it was possible to evaluate the tool center multiple times using the same test plug simply by changing the centerline position for the interpolated radius. Test plug was machined and measured 4 times (different R_i), the calculated $CL_{x\text{-coord}}$ (centerline position) remained constant within 2 μm and as shown in Table 2-1.

Table 2-1. Results for tool centering calculation

| Step | Centerline for interpolated radius | Astigmatism | ΔX | Calculated Centerline position (mm) |
|-------------|---|--------------------|------------------------------|--|
| 1 | 142.6467 | 0.82 μm | 58.7 μm | 142.5880 |
| 2 | 142.6245 | 0.54 μm | 38.2 μm | 142.5863 |
| 3 | 142.6025 | 0.21 μm | 14.8 μm | 142.5877 |
| 4 | 142.5877 | 0.02 μm | 1.7 μm | 142.5860 |

Although astigmatism error after step 4 in Table 2-1 was low, a feature could still be observed on the astigmatism profile as shown on Figure 2-11. After further investigation and tracking the tool path error in the X axis, it was found that this feature was caused by backlash in slide driving mechanism as tool changes direction close to the apex of its circular trajectory as shown on Figure 2-12.

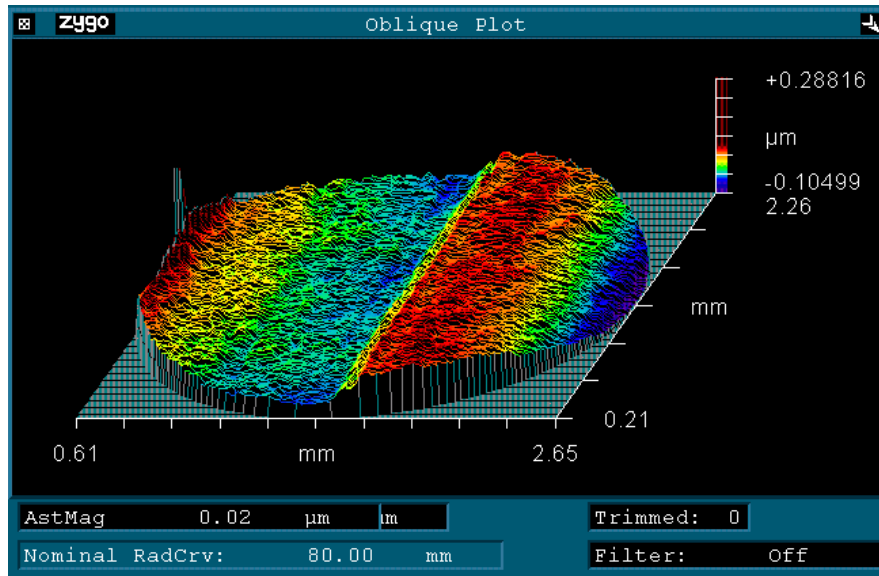


Figure 2-11. Astigmatism error profile after 4th tool iteration of tool centering

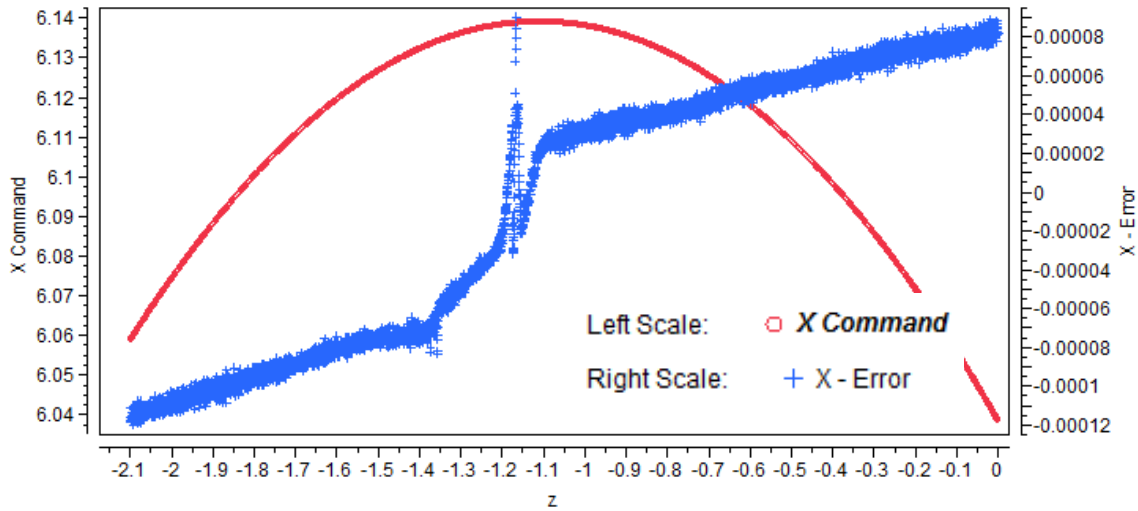


Figure 2-12. X-error and x-command as a function of Z command for test plug machining

Although the magnitude of this error is small (10-100 nm), it results in an error in the same order of magnitude as the astigmatism error (δ) that can be measured. This limits the accuracy of tool centering calculation to 2 μm and therefore the maximum possible misalignment to 4 μm . To avoid possible misalignment, OD was machined and then ID was machined 10 μm

smaller than the calculated value. 1 μm was removed at a time until parts can be assembled together successfully.

2.2.2 Machining and Assembly

Both dimensional and geometrical tolerances for rough part machining were designed to ensure that 20 μm of material was left to machine with the DTM. For example, outside diameter of top insert D1 must be machined concentric with the bore D4, while base diameter D2 has to be machined perfectly concentric with diameter D4 (see Figure 2-13). After machining these surfaces, insert outside diameter D1 still has to be larger than the base inside diameter D2 so that clearance GD1 can be adjusted.

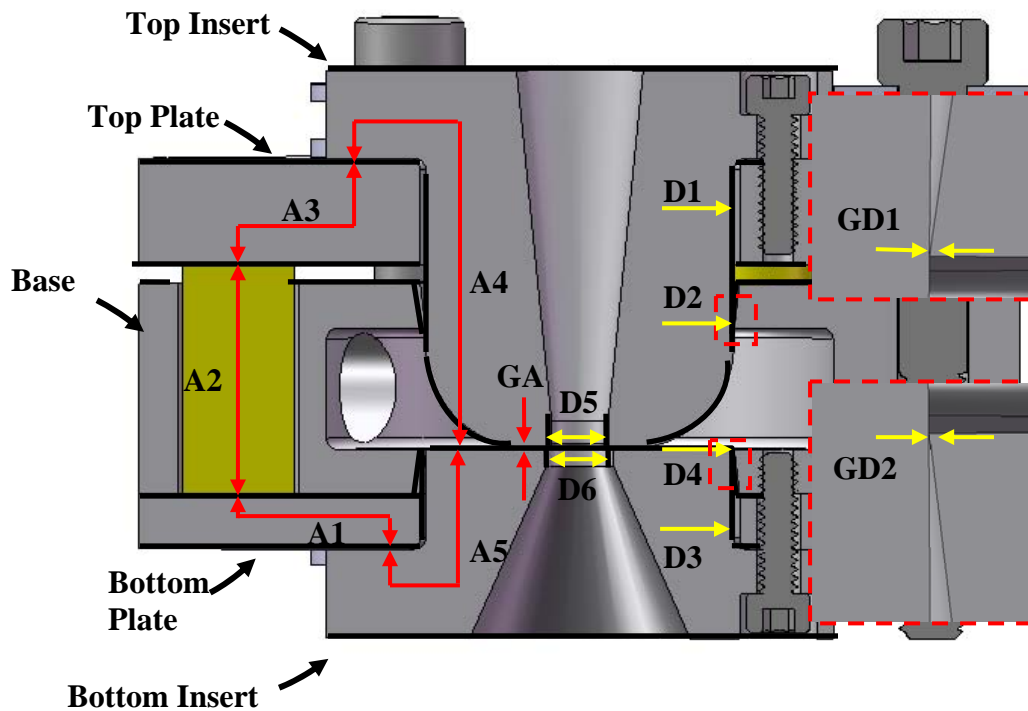


Figure 2-13. Machined surfaces (bold) and measurement chains on air amplifier

A summary of the machining and assembly steps is presented in Table 2-3 at the end of this section. The first parts machined with diamond tool were the faces of bottom plate, base and top plate (A1 and A3). The next part to be diamond turned was the bottom insert dimension

A5. To machine the outside face of the top and bottom insert, a special part holder was designed and machined. This part holder can be seen on Figure 2-14 and detailed drawing can be found in Appendix. Both faces of tool holder were diamond turned to ensure parallelism.

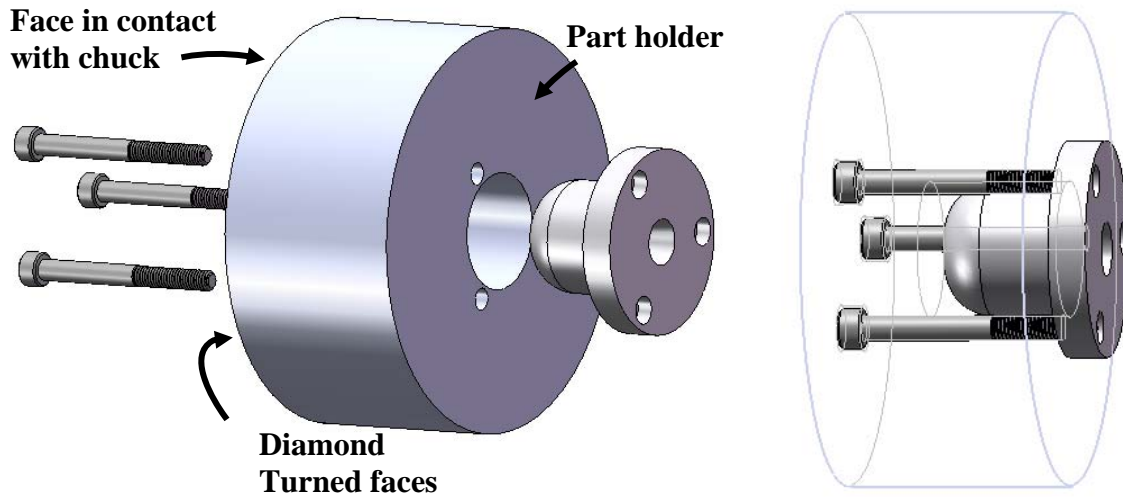


Figure 2-14. Tool holder used to machine top and bottom insert

The next machining step was the inside diameter of the base D4. As it is critical that D4 and D2 are concentric, base was first centered with reference to D4 taper. Then outside diameter of the part was diamond turned as a reference to center the part when D2 is machined. The conical section on D4 was first machined with the DTM. Because the inside faces of plenum are not diamond turned, lack of parallelism between the inner and outer faces of the plenum created resulting from rough machining cannot be corrected. After diamond turning the conical section, any misalignment between these faces will result in a circularity and concentricity defect on the inside diameter D4. For that reason and also to make it possible to perform direct measurement of the diameter D4 on the CMM, a flat was machined on the diameter D4 as shown on Figure 2-15. Once D4 was machined, part was flipped, centered about the reference previously made to maintained concentricity of features and D2 was machined using the same sequence (see Figure 2-13 for reference).

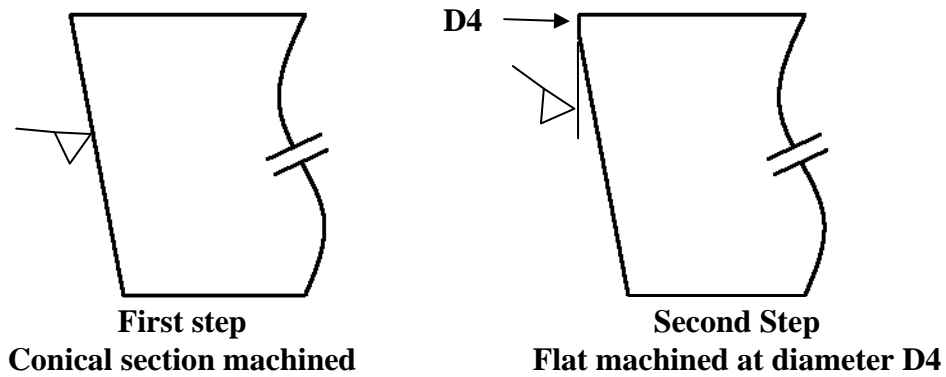


Figure 2-15. Machining of inside diameter on base

Diameter D3 was then machined on the bottom insert. The insert was first centered on the spindle with reference to the center orifice D6 and a reference surface was machined on the outer diameter of the flange. Diameter D3 was reduced until it was 10 μm larger than the diameter D4 found with the CMM. D3 was then reduced in step of 1 μm radially until it could be inserted in the base. Center orifice was then machined until its diameter reached 6.150 mm when measure with the ASG. Final X coordinate on the DTM controller was duly noted as it will be used to machine the diameter D1 1.000 mm smaller.

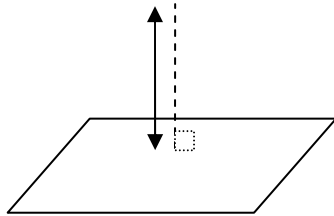
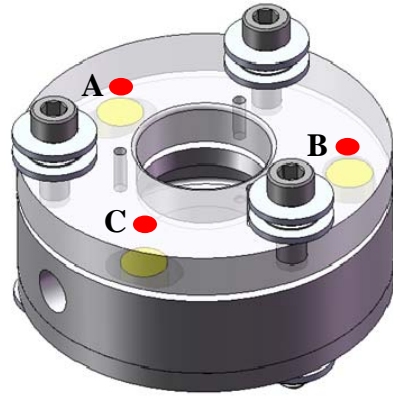
The top insert was then centered on the spindle with reference to D5. The part was touched off with the diamond tool on the ASG at multiple locations on the curved section, on the outside diameter (D1) and on the annular gap face. X and Z coordinates were recorded at every location. These positions were used to program the tool path to machine the outside diameter, the outer radius and the annular gap. Then, D1 was machined using the same approach as D2.

Tool path for the critical 0.5 mm radius was programmed and tool was approached along the Z axis until the Coanda radius was formed and the surface of the annular gap touched off. The part was then approached along the X axis to adjust the inside diameter D5 at 1 μm from its final dimension, i.e. 0.500 mm from the final X coordinate that was recorded when D6 was machined. A final pass was performed, removing 1 μm simultaneously on both the

inside diameter and the face of the annular gap, ensuring a smooth Coanda radius. Note that the tool could not reach the entire length of diameter D5, a thinner dead sharp tool was used to reach the end of the D5 hole. A 20 μm step remained after this operation and CFD analysis was performed by the AECFDL lab to make sure that flow was not affected by this defect.

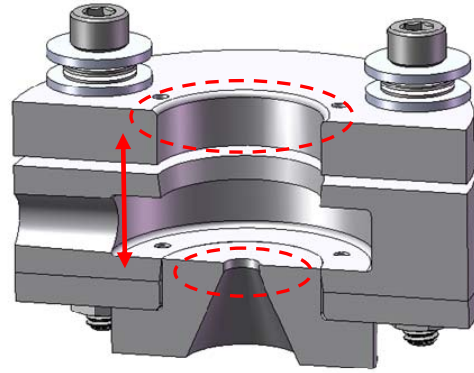
The final and most critical step is the machining of the flange of the top insert that defines A4 or the annular gap width. First, parallelism between the top plate and the top of the bottom flange had to be measured and adjusted using the 12 μm stainless steel shims (Section 2.1). Using the CMM, two different measurement methods were used, the parallelism between both planes calculated at the upper insert bolting diameter (using 12 points on each planes) and the perpendicular distance between the bottom insert face and a point on the top above each piezoelectric actuators. Results before and after shimming are presented on Figure 2-16.

Distance point –plane between PZT location and annular gap bottom face



| pzt | Before Correctio | Shim Used | After Correctio |
|-----|------------------|-----------|-----------------|
| A | 26.333 | 1 | 26.352 |
| B | 26.332 | 2 | 26.350 |
| C | 26.348 | 0 | 26.351 |

Plane-plane parallelism between annular gap bottom face and top insert flange mating face



| Measure no. | No shim | After shimming |
|-------------|---------|----------------|
| 1 | 0.008 | 0.002 |
| 2 | 0.008 | 0.002 |
| 3 | - | 0.002 |

Figure 2-16. Parallelism adjustment and annular gap measurement

After level correction, an out of parallelism of 2 μm over top insert bolting radius will result in an out of parallelism of 0.5 μm between the two annular gap faces, which satisfies the design criteria of 1 μm established earlier. Machining and assembly steps are summarized in Table 2-2.

Table 2-3. Summary of machining and assembly steps of the Air Amplifier I

| Step | Description |
|------|--|
| 1 | Machine both faces of top plate (A3) |
| 2 | Machine both faces of bottom plate (A1) |
| 3 | Machine both faces of base |
| 4 | Machine bottom insert (D3 and A5) |
| 5 | Machine D4 on Base to set GD2 |
| 6 | Machine flange of Top Insert and outside diameter (D1) |
| 7 | Machine D2 on Base to set GD1 |
| 8 | Machine Coanda radius and orifice D5 on Top insert |
| 9 | Machine orifice D6 on Bottom insert |
| 10 | Assemble Top Plate, Bottom Plate, Base, PZT. Level and measure A4. |
| 11 | Machine flange of Top Insert to set annular gap (GA) |

2.2.3 Piezoelectric Actuators Calibration

Once parallelism between annular gap bottom face and top insert flange mating face was established (see Figure 2-16 of previous section), the 3 piezoelectric actuators were connected in parallel to an adjustable DC voltage source and an amplifier for calibration. Setup is presented on Figure 2-17.

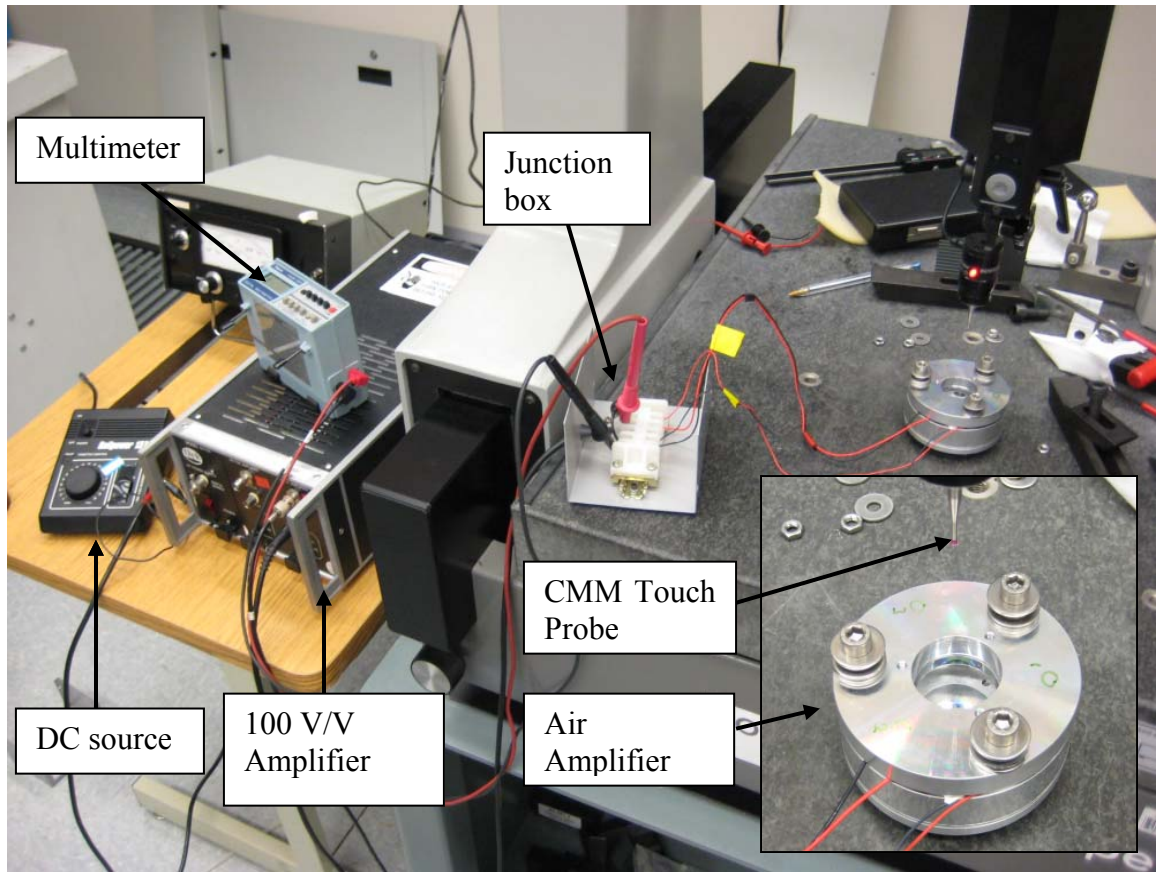


Figure 2-17. Setup for Air Amplifier Piezoactuators Calibration Curve measurement

Parallelism and plane/plane distance (Figure 2-16) for different applied voltage were measured to establish a calibration curve for the PZT. The hysteresis curve of motion vs voltage presented on Figure 2-18. The top insert was machined so that the annular gap is $50\ \mu\text{m}$ when plane/place distance is $26.351\ \text{mm}$, this curve can be used to determine indirectly the annular gap as a function of the voltage when operating the air amplifier. The hysteresis error between ascending and descending voltage is relatively large (up to $5\ \mu\text{m}$ at the mid range of the actuator). For that reason, voltage will be reduced to $0\ \text{V}$ before setting any voltage adjustment so that only the ascending section of the curve is used.

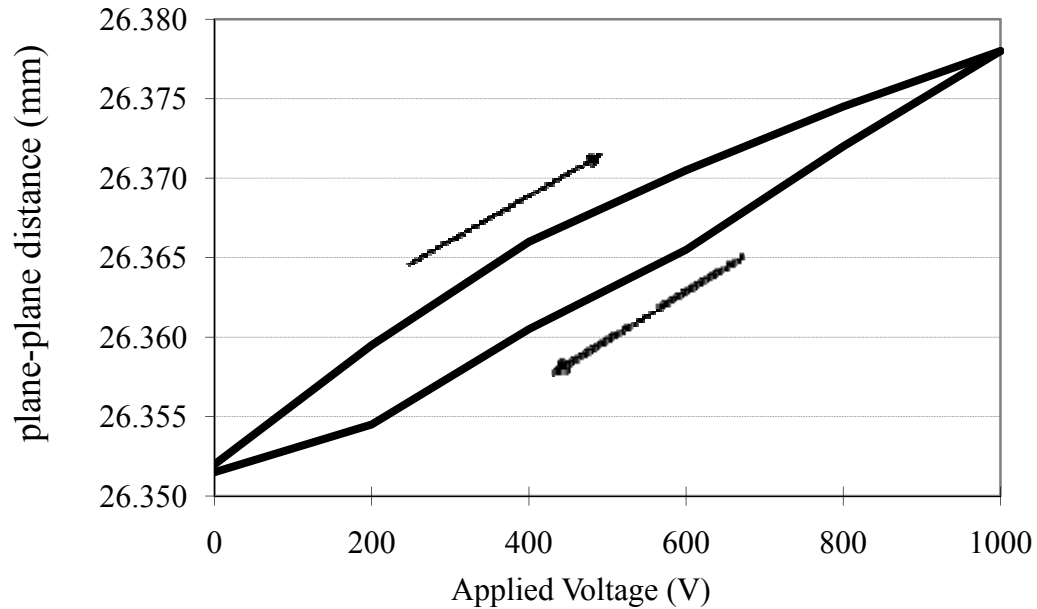


Figure 2-18. Relation between applied voltage and annular gap to top insert mating face

The maximum parallelism error that was measured over the top flange bolting diameter during these tests was 3 μm , ensuring an out of parallelism of less than 1 μm across the annular gap. All measurements can be found in APPENDIX B – Additional Measurements on First Iteration of Air Amplifier.

Using the CMM, the distance between annular gap face and flange of the top insert was measured and machined to be 50 μm less than the nominal distance (0 V applied) between the top insert mating face and the annular gap face on the air amplifier as shown on Figure 2-19. White light interferometry was used to inspect final geometry and make sure that there was no abrupt transition on the Coanda radius or any the sharp edge on the opposite face of the annular gap (see Figure 2-20). The surface finish was 10-20 nm Ra which is below the refinement of the CFD numerical calculation.

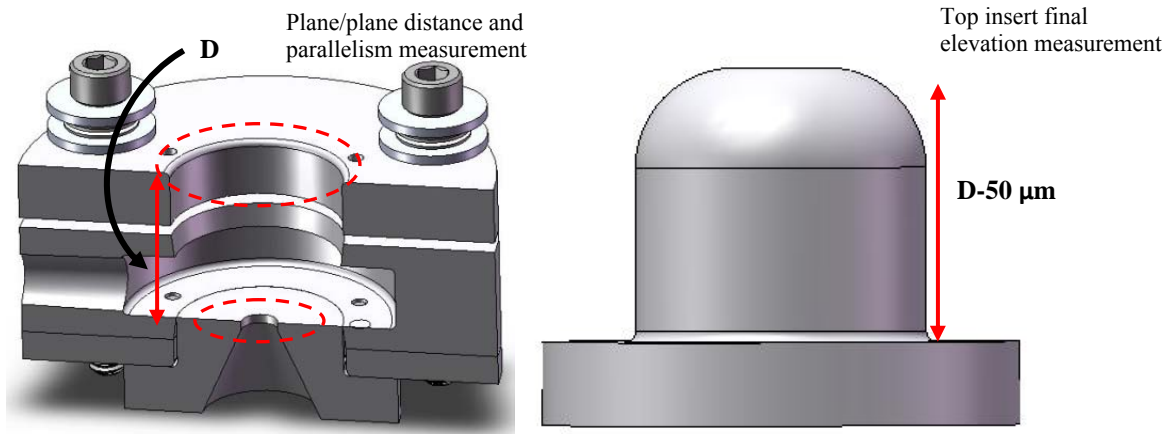


Figure 2-19. CMM machine used to measure annular gap indirectly

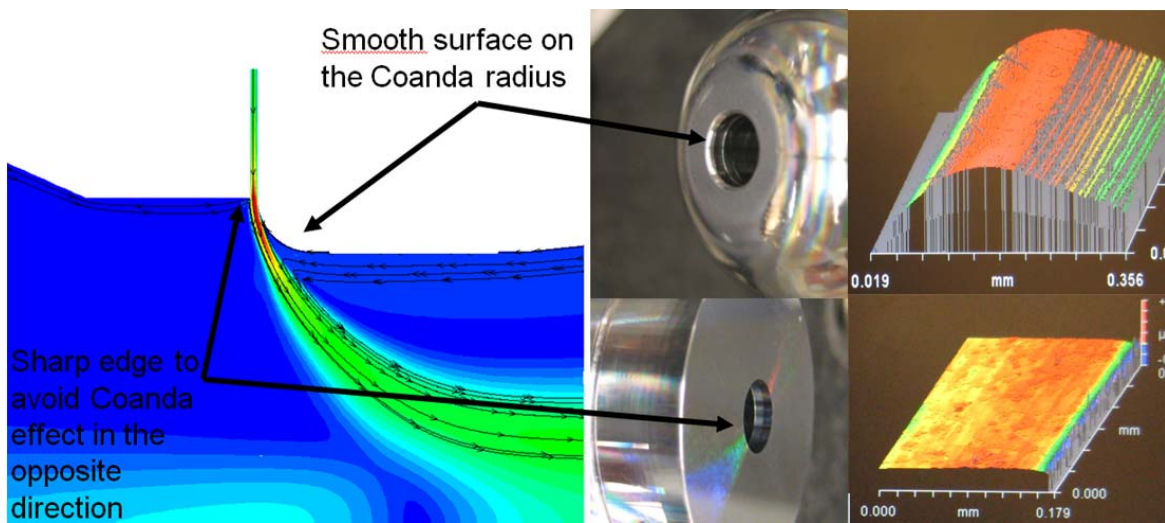


Figure 2-20. Diamond turning of critical surfaces and verification using New View (white light interferometer)

2.3 Testing

2.3.1 Static pressure measurements

To quantitatively describe the aerodynamic performances of the air amplifier, static pressure measurements were collected along the flow axis of the air amplifier. According to Bernoulli's equation for adiabatic incompressible flow, neglecting the effect of changes of elevation:

$$P_{\text{static}} + \frac{\rho V^2}{2} = P_{\text{total}} \quad (2.4)$$

Where V is the velocity of the fluid and ρ is its density. Since the CFD model predicts a gas (air) flow velocity of less than 100 m/s (0.3 Mach), the fluid can be considered incompressible. In the case of an adiabatic flow in a conduit, a decrease in pressure signifies an increase in velocity of the fluid. Measuring the static pressure (P_{static}) along the flow can be used to plot the velocity distribution along the axis of the air amplifier. The pitot tube was fabricated by drilling four axis-symmetric 0.020" holes in a 1/16 in OD stainless steel tube (0.020" ID). One end of the tube was plugged and the other end was connected to a digital manometer to measure the gauge pressure as shown on Figure 2-21. The pitot tube was held fixed and a xyz stage was used to move the air amplifier and measure the static pressure at multiple locations along its axis.

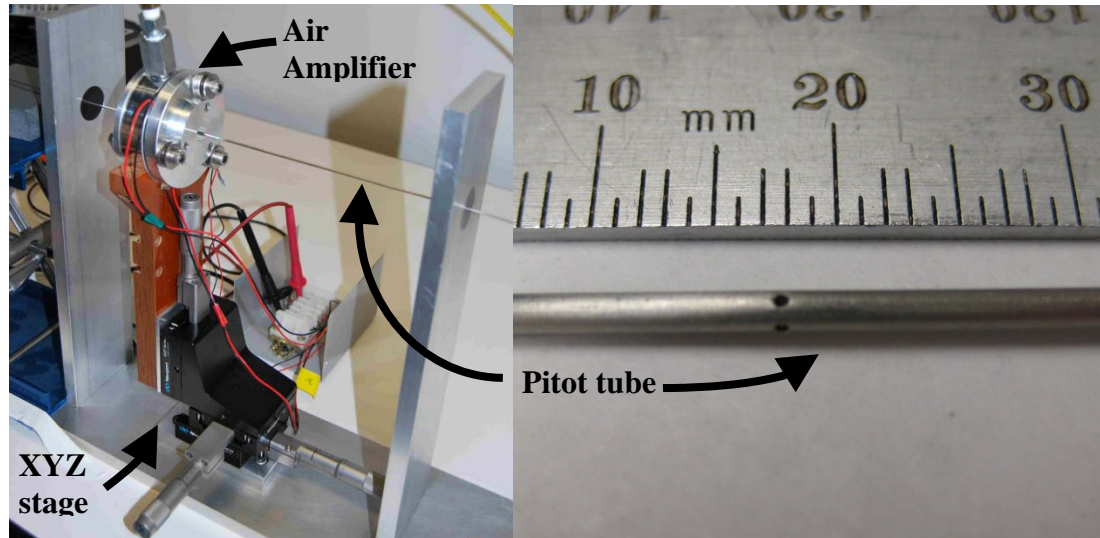


Figure 2-21. Setup for pitot tube pressure measurements

When pressurized, the air amplifier successfully created a Venturi effect and static pressure was measured along the flow axis for different supply pressures and annular gaps. These results showed that for every gap and plenum condition, the maximum vacuum pressure was located at 1 mm downstream of the annular gap. Also, as shown in Figure 2-22, increasing the plenum pressure or increasing the annular gap both increased the maximum vacuum pressure while keeping the pressure profile nearly the same. Even though a higher vacuum peak can be obtained with a larger annular gap if pressure is kept constant, the maximum vacuum obtained for each annular gap is the same as shown in Table 2-4. This is because the Coanda effect is eventually lost when a maximum plenum pressure or annular gap threshold is reached. For example, at 30 psi the annular nitrogen jet exiting from the 50 μm annular gap curves around the Coanda surface, remaining attached to the surface. In contrast, the annular jet formed through the 70 μm annular gap at 40 psi detaches from the Coanda surface, inhibiting the Venturi effect. This loss of the Coanda effect occurs instantaneously and can actually be heard during the experiments as a popping sound when either pressure or annular gap is increased over that threshold and the plenum gas starts exiting through both inlets.

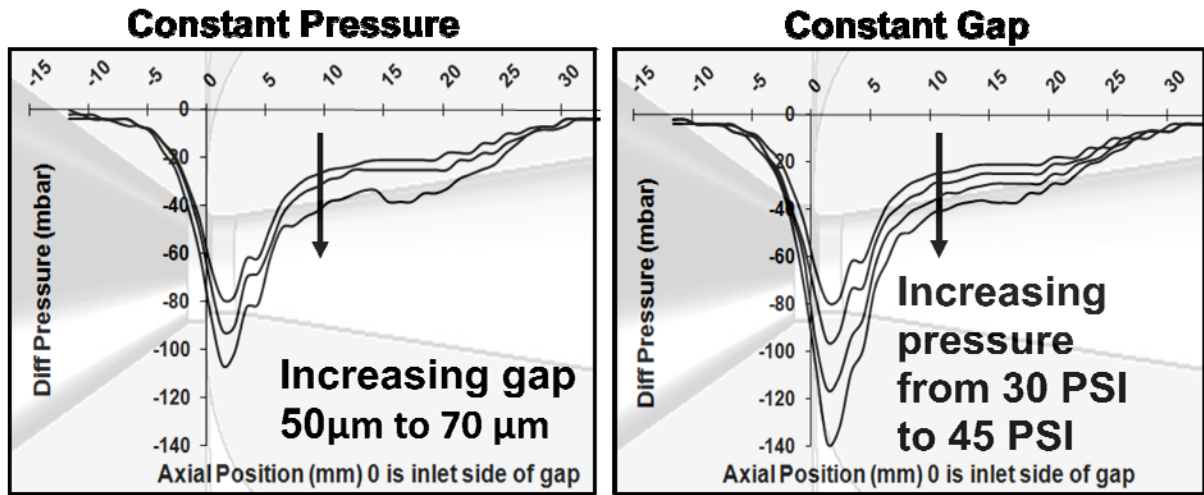


Figure 2-22. Effect of plenum pressure increase vs annular gap increase on pressure profile

Table 2-4. Maximum vacuum as a function of plenum pressure and annular gap width

| | | Annular Gap | | |
|-----------------|--------|-------------|-----------|-----------|
| | | 50 μm | 60 μm | 70 μm |
| Plenum Pressure | 30 psi | -79 mbar | -92 mbar | -107 mbar |
| | 35 psi | -96 mbar | -120 mbar | -144 mbar |
| | 40 psi | -116 mbar | -140 mbar | No Coanda |
| | 45 psi | -139 mbar | No Coanda | No Coanda |

Conclusion from these static pressure measurements is that piezoelectric actuators are not needed because the effect of increasing the gap can be created by increasing the plenum pressure. This simplifies significantly the fabrication and assembly of the device as well as its final cost. Furthermore, the results confirmed and reinforced the CFD model results.

2.3.2 Characterization Using Current Measurement

The first attempt to measure the effect of the air amplifier on the ion abundance was done using a vacuum enclosure containing a skimmer cone and quadrupoles. As explained in Section 1.1.3, one technique to measure ion abundance is to measure the current generated by

the ions being neutralized on the detector plate. The premise of this experiment is to use the skimmer cone in lieu of a detector plate and measure ion abundance. Normally, the purpose of a skimmer cone in a mass spectrometer is to collect the ions in a specific zone when they come out of the capillary and expand in the vacuum box as illustrated in Figure 2-23. Typically, a bias of the same polarity as the ions to be collected is applied to the skimmer cone to prevent the ions from colliding with it. However in this case, the skimmer cone was grounded and used in lieu of a Faraday cup to measure ion current. This current was measured using a Keithley 617 electrometer from Keithley Instrument (Cleveland, OH).

The current flowing between the cone and the ground is in ampere (or q/s) and is a direct measurement of the number of charge hitting the skimmer cone every second. Both the ESI emitter and the air amplifier were mounted on XYZ stages with micrometers so that their position can be controlled with precision (see Figure 2-24). A LVDT was also installed to record the position of the air amplifier. LVDT and the Keithley 617 were connected to a data acquisition system so that the current can be plotted as a function of the position of the air amplifier while exploring different condition of operation using Labview (National Instrument, Austin, TX).

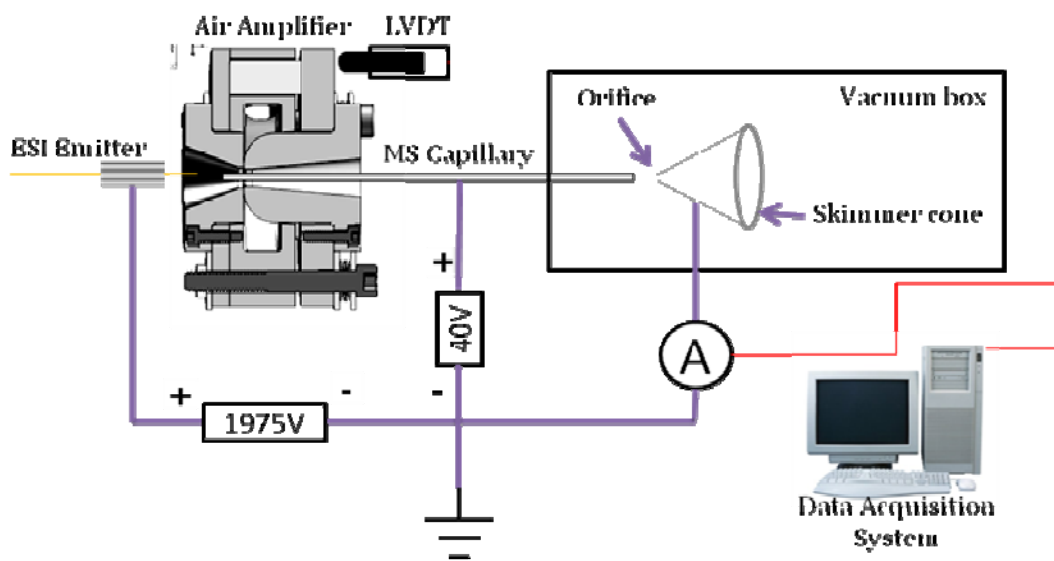


Figure 2-23. - Schematic of setup for current measurement on MS skimmer cone

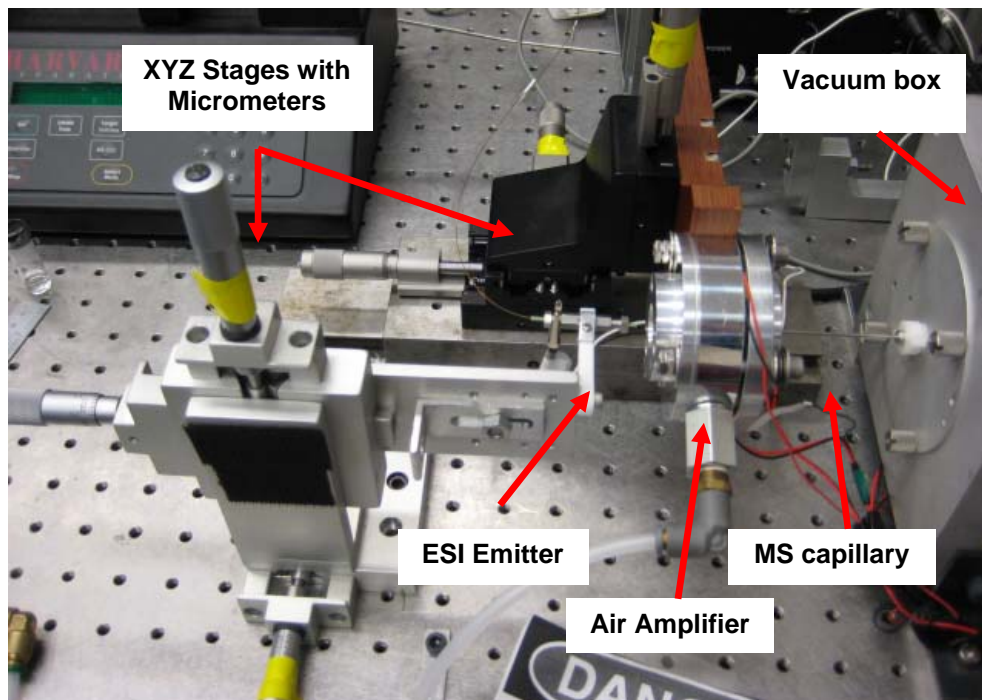


Figure 2-24. Setup for current measurement on MS skimmer cone

Pressure of the air amplifier was initially set at 30 psi and the annular gap was set at 50 μ m. Two different solutions (1:1:1 tetramethyl:tetrabutyl:tetraheptyl amines and 50:50:0.1 ACN:H₂O:FA) were electrosprayed at a flow rate of 1 μ L/min with electrospray gap of 3, 5, 7 and 9 mm. It was found that in all cases the maximum current was obtained when the ESI tip was positioned 1 mm downstream of the annular gap of the air amplifier (see Figure 2-25). This zone corresponds to the peak in maximum vacuum pressure that was measured in the air amplifier during pitot tube tests. Additional experiments were also performed to look at the effect of an increase of the plenum pressure on the skimmer cone current (from 30 psi to 45 psi) or the increase of the annular gap of the air amplifier (from 50 μ m to 70 μ m). Such a variation of pressure and gap resulted in an increase of the vacuum pressure in the region of the annular gap of the air amplifier by up to 75%. However, the increase on the skimmer cone current did not exceed 15%.

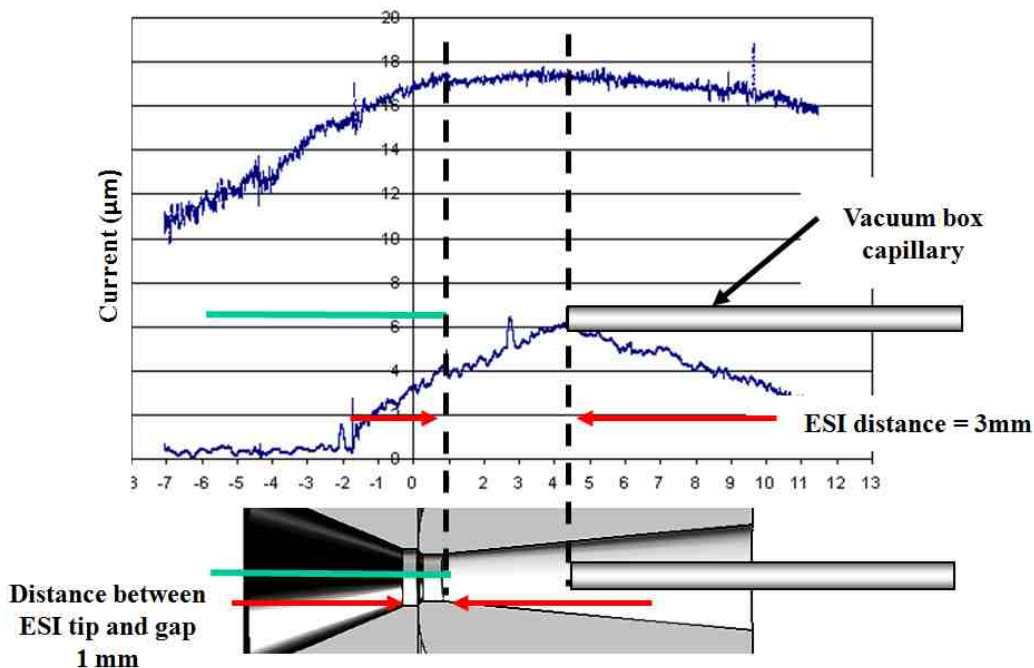


Figure 2-25. Skimmer cone current vs air amplifier position

One of the main drawback of using the skimmer cone current as a Figure of Merit for the transmission of the ions from the ESI tip to the mass spectrometer is that it is not possible to discriminate the ions hitting the skimmer cone that are single gas phase ions from those that are ions in droplets of solvent and poorly desolvated. As only the gas phase ions can be measured by the mass spectrometer, an increase in skimmer cone current does not necessarily translate in an increase in gas phase ion abundance on an actual mass spectrometer instrument. Also, it is not possible to tell if an increase in the skimmer cone current is due to an increase in the performance of the charge transmission from the emitter tip to the mass spectrometer or simply to an overall increase of the electrospray current (number of charge emitted from the ESI tip). Therefore, it was decided to test the air amplifier with an actual mass spectrometer so that a direct measurement of effect of the air amplifier on the abundance on gas phase ions measured by the mass spectrometer can be monitored.

2.3.3 Fourier Transform Mass Spectrometer (FTMS)

A FTMS 9.4T located at the W.M. Keck FTICR Mass Spectrometer Laboratory at North Carolina State University was used to perform the next set of experiments. The first attempt to characterize the air amplifier with the FTMS was made by monitoring the abundance of specific ions while varying different parameters of the FTMS. One of the main difficulties encountered was the instability of the abundance measurement. To obtain significant results, data had to be collected over a long period of time. A plot of the abundance of the 857 ± 1 m/z ion of a $1 \mu\text{M}$ (micromolar) ubiquitin in 50:50:0.1% acetonitrile:water:formic acid for a ESI gap of 9 mm revealed that the peak of abundance measurement was found when the MS tip was 1 mm downstream of the air amplifier annular gap (see Figure 2-26). This location corresponds to the location of the minimum static pressure found during the pitot tests measurement. This confirms that there is a correlation between the aerodynamic focal point and an increase in ion abundance.

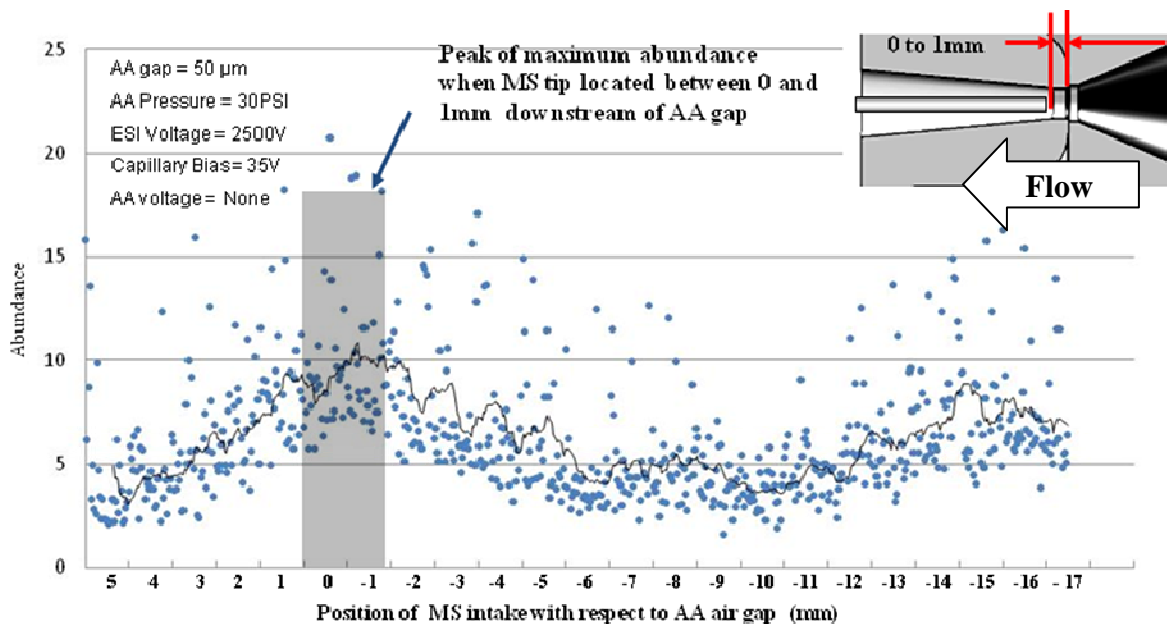


Figure 2-26 - Abundance as a function of AA along axis

After setting the position of the air amplifier at its optimal position, the abundance of the ions with and without the air amplifier was compared for different ESI gaps. Signal was acquired

during 5 minutes with the air amplifier turned off and then 5 minutes with the air amplifier turned on (50 μm annular gap and 30 psi pressure). Since the FTMS was performing 1 measurement every 4.11 seconds, 75 measurements were collected for each condition. Under these conditions, it was found that the air amplifier improved the signal for large ESI gap only. No improvement was measured at ESI gap of 3 mm and improvements up to 4.34 folds was measured for an ESI gap of 9 mm (see Figure 2-27). However, best signal obtained with the air amplifier at 9 mm ESI gap was still lower than the signal obtained without the air amplifier at 3 mm. This means that there was no absolute abundance increase, only relative improvement at larger ESI gap.

Abundance measured with the Fourier Transform Mass Spectrometer is very sensitive to instrument settings, making results harder to reproduce and harder to attribute to the addition of the air amplifier. These instrument settings are adding to the variable potentially influencing signal abundance, making it more difficult to characterize the effect of the air amplifier.. To better characterize the effect of the air amplifier, additional experiments was performed on a more robust type of mass spectrometer more commonly used in the industry (QqQ). Also, a more systematic approach was taken using design of experiment to better quantify the effect of each variable and make sure that the entire experimental space is explored.

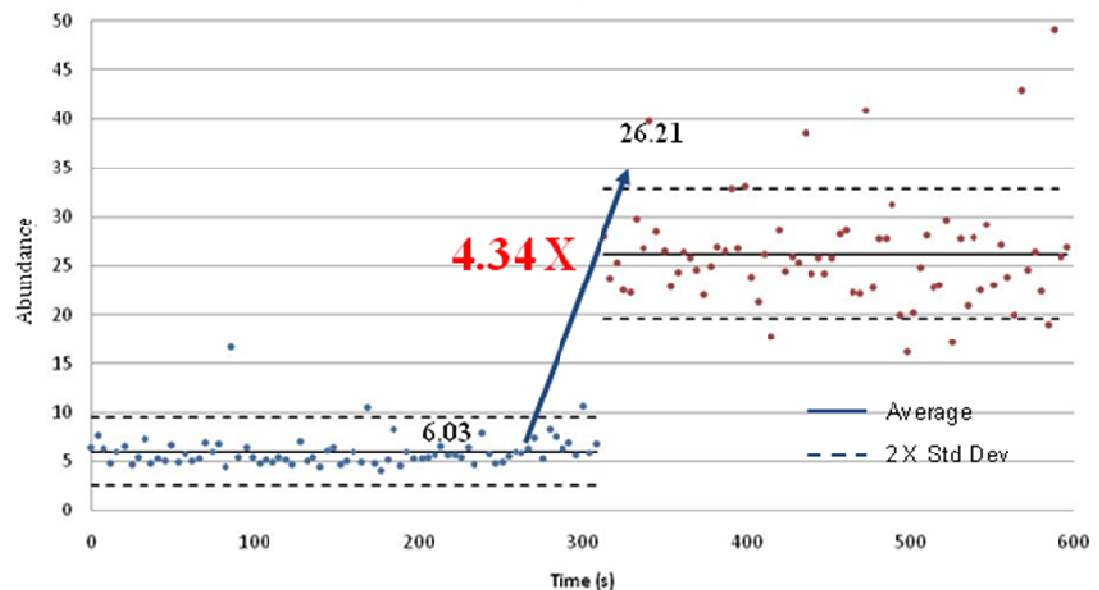


Figure 2-27 – Improvement of 4.34 folds of abundance measured for a ESI gap of 9mm

2.3.4 Design of Experiment

During the preliminary tests performed with the air amplifier on a FTMS Spectrometer, 10 different variables or parameters were identified as potentially having an effect on the performance of the air amplifier. Clearly identifying the parameters that do have an effect on the output by randomly tuning each of the parameters individually will give no guarantee that all the experimental space was covered. For this reason, a more systematic approach was implemented through a experimental strategy to screen the variables and determine their effects on the performance of the air amplifier.

One way to cover the entire experimental space is to experimentally test all of the possible combination of settings. Although very effective in theory, it is unrealistic to use this approach. If for example, 2 values for each variable, high (+) and low (-), are chosen for n variables suspected to have an effect on a given output, 2^n experiments will be needed to identify the main effects and the all the possible interactions between variables that have an impact on the results. The number of experiment increases exponentially with the number of variables tested, it quickly becomes unrealistic to test all possible combinations. This

approach is called a Full Factorial Design. If one accepts allows the confounding of the main effects with some interactions, the number of experiments can be reduced significantly. This is achieved using a Fractional Factorial Design (FFD): allowing the setting of one or more variable to be defined by the combination of other variable throughout the experiments. For example, if the effects of 5 variables are investigated, say ABCDE, all level combinations (+ and -) of the 4 first variables can be tested (ABCD) and the level of the fifth variable E can be defined as the combination of ABCD (ex. If ABCD = ++++ or ---+ → E = -). Consequently, the number of experiments will be reduced to 16. This scenario is presented in Table 2-5. Each of the 16 experiment are performed setting ABCDE at the low or high value as set by the table. Analysis of the results of FFD can be performed as follow: each effect or interaction contrasts can be extracted by adding or subtracting for each column the results Y_i , depending of the sign it was assigned for each experiment. A large positive value would mean that the variable assigned to the “+” level has a positive effect on the output when compared to the value assigned to the “-” level. A large negative would mean the opposite, i.e. that the value assigned to the “-” level has a positive effect on the output. A value close to 0 would mean that the choice of the “-” or “+” value has a minimal impact on the results. For example, the effect of variable E is calculated as follow:

$$E_E = \frac{Y_1 - Y_2 - Y_3 + Y_4 - Y_5 + Y_6 + Y_7 - Y_8 - Y_9 + Y_{10} + Y_{11} - Y_{12} + Y_{13} - Y_{14} - Y_{15} + Y_{16}}{16} \quad (2.5)$$

P-values, t-ratio or other statistical hypothesis tests can then be calculated for each to weight and compare significance of the different effects and interactions. JMP version 8.0 from (SAS, Cary, North Carolina) was used to generate the experimental pattern and perform the screening analysis.

Table 2-5. Representation of a resolution V fractional factorial design for 5 variables

| | A | B | C | D | E = ABCD | AB | AE | ABC | ... | Y |
|----|---|---|---|---|----------|----|----|-----|-----|-----|
| 1 | + | + | + | + | + | + | + | + | ... | Y1 |
| 2 | + | + | + | - | - | + | - | + | ... | Y2 |
| 3 | + | + | - | + | - | + | - | - | ... | Y3 |
| 4 | + | + | - | - | + | + | + | - | ... | Y4 |
| 5 | + | - | + | + | - | - | - | - | ... | Y5 |
| 6 | + | - | + | - | + | - | + | - | ... | Y6 |
| 7 | + | - | - | + | + | - | + | + | ... | Y7 |
| 8 | + | - | - | - | - | - | - | + | ... | Y8 |
| 9 | - | + | + | + | - | - | + | - | ... | Y9 |
| 10 | - | + | + | - | + | - | - | - | ... | Y10 |
| 11 | - | + | - | + | + | - | - | + | ... | Y11 |
| 12 | - | + | - | - | - | - | + | + | ... | Y12 |
| 13 | - | - | + | + | + | + | - | + | ... | Y13 |
| 14 | - | - | + | - | - | + | + | + | ... | Y14 |
| 15 | - | - | - | + | - | + | + | - | ... | Y15 |
| 16 | - | - | - | - | + | + | - | - | ... | Y16 |

However, with FFD it is not possible to differentiate the effect of some variables with the effect of combination of other variables. The following confounding structure will be created in this specific case : A & BCDE, B & ACDE, C & ABDE, D & ABCE, ABCD & E, AB & CDE, AC & BDE, etc. As some 2-variables interactions are confounded with 3-variables interactions, it is by definition a FFD of resolution V. The number of experiments can be reduced to 8 experiments if variable D is defined by AB and variable E is defined by BC. However, resolution will then be reduced to III as the main effect of a variable will be confounded with some 2-variables interactions (D & AB for example) and 2-variables interactions will be confounded with other 2-variables interactions. Any 2-levels with n variables that would be a full factorial design with 2^n experiments can be converted in a fractional factorial design with 2^{n-k} experiments, with k being the number of variable settings that will be defined by the combination of others. The resolution of the resulting FFD is defined by the variables that are confounded as follow [26] :

Resolution III Designs: Main effects are confounded or confounded with 2-variables interactions and two-factor interactions are confounded with each other.

Resolution IV Designs: No main effects are confounded with 2-variables interactions, but 2-variables interactions are confounded with each other.

Resolution V Designs: No main effect or two-factor interaction is confounded with and other main effect or 2-variables interaction, but 2-variables interactions confounded with 3-variables interactions

Comparing the resulting number of experiments required for full factorial design with n variables and a fractional factorial design experiments of different resolutions, it is obvious that for large number of variable (n) a FFD becomes a necessity as shown on Figure 2-28.

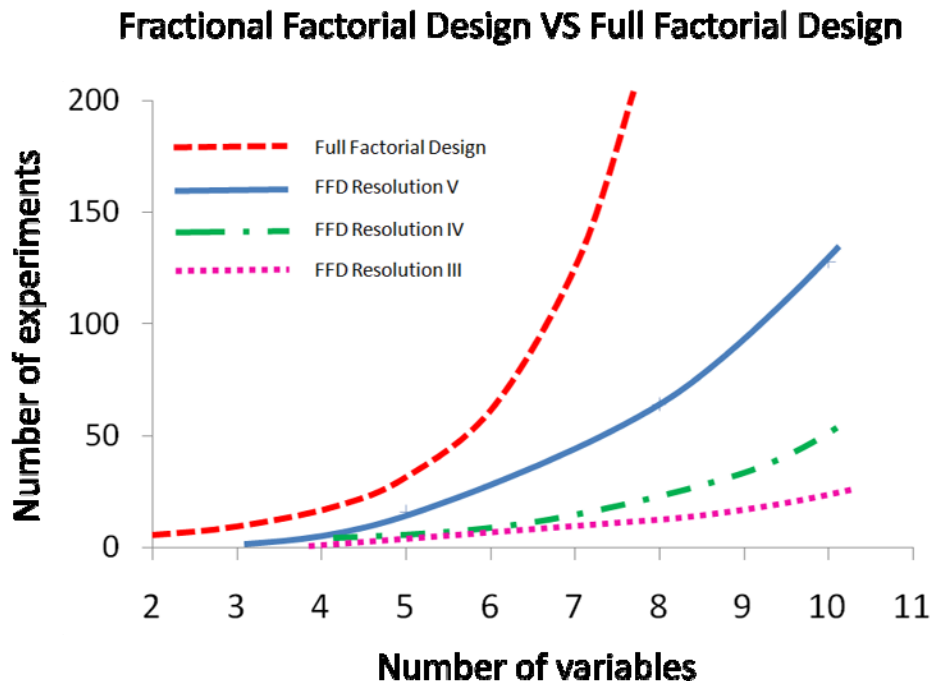


Figure 2-28. Full factorial design vs fractional factorial design of different resolution

2.3.5 Results on a QqQ Mass Spectrometer

To find the variables that could potentially have an effect on the air amplifier performances. Resolution V FFD with 9 variables was performed. The variables and the 2 levels evaluated for each of them are presented in Table 2-6 and motivation for each choice of variable is also

indicated. The experiments were performed at high flow rates and ESI tip sizes (75-100 μm tip and 1-2 $\mu\text{L}/\text{min}$ of 1 μM melittin) as prescreening experiments showed significant improvement in that range.

Table 2-6. Variable definition for FFD experiments

| Variable | Level + | Level - | Motivation |
|---------------------------------------|----------------------------|------------------------------|--|
| Position of vacuum peak | 1 mm from ESI Capillary | 1 mm from MS inlet | Previous experiments showed that these 2 parameters could have a positive impact |
| ESI Gap | 9 mm | 6 mm | As no improvement was found at 3m m with the amplifier during previous experiment, larger space was explored |
| ESI Voltage | 3200 V | 2800 V | Range that showed good performance in previous experiments |
| N2 Temperature | 100°C | 25°C | Hot N ₂ can improve desolvation |
| Air amplifier pressure | 45 Psi | 30 Psi | Amplifier pressure range |
| Composition | 100% H ₂ O | 25% H ₂ O/75% ACN | Test the hypothesis that the air amplifier can improve desolvation of aqueous solvents. |
| Air amplifier radial alignment | Centered | 0.75 mm offset | Further investigate results obtained with FTMS |
| ESI Tip size | 100 μm | 75 μm | As previous experiments showed no overall signal improvement with air amplifier. This is to test the hypothesis that better results can be obtained with larger tips |
| Flow | 2 $\mu\text{L}/\text{min}$ | 1 $\mu\text{L}/\text{min}$ | ESI droplet size increases at higher flow. See effect of air amplifier on droplet desolvation. |

Results of these experiments are presented in Figure 2-29. Top of figure shows a half normal quantile plot where absolute contrast (effect) of each variable (vertical) is compared to expected value assuming effect of variable is null (horizontal). Therefore, variable away

from the normal line are those having an effect on the abundance. Below the half normal plot is presented the calculated effect of each variable as well as their p-value (indication of their statistical significance). For example a p-value of 0.001 signifies that there is only a 0.1% chance that the observe effect purely coincidental.

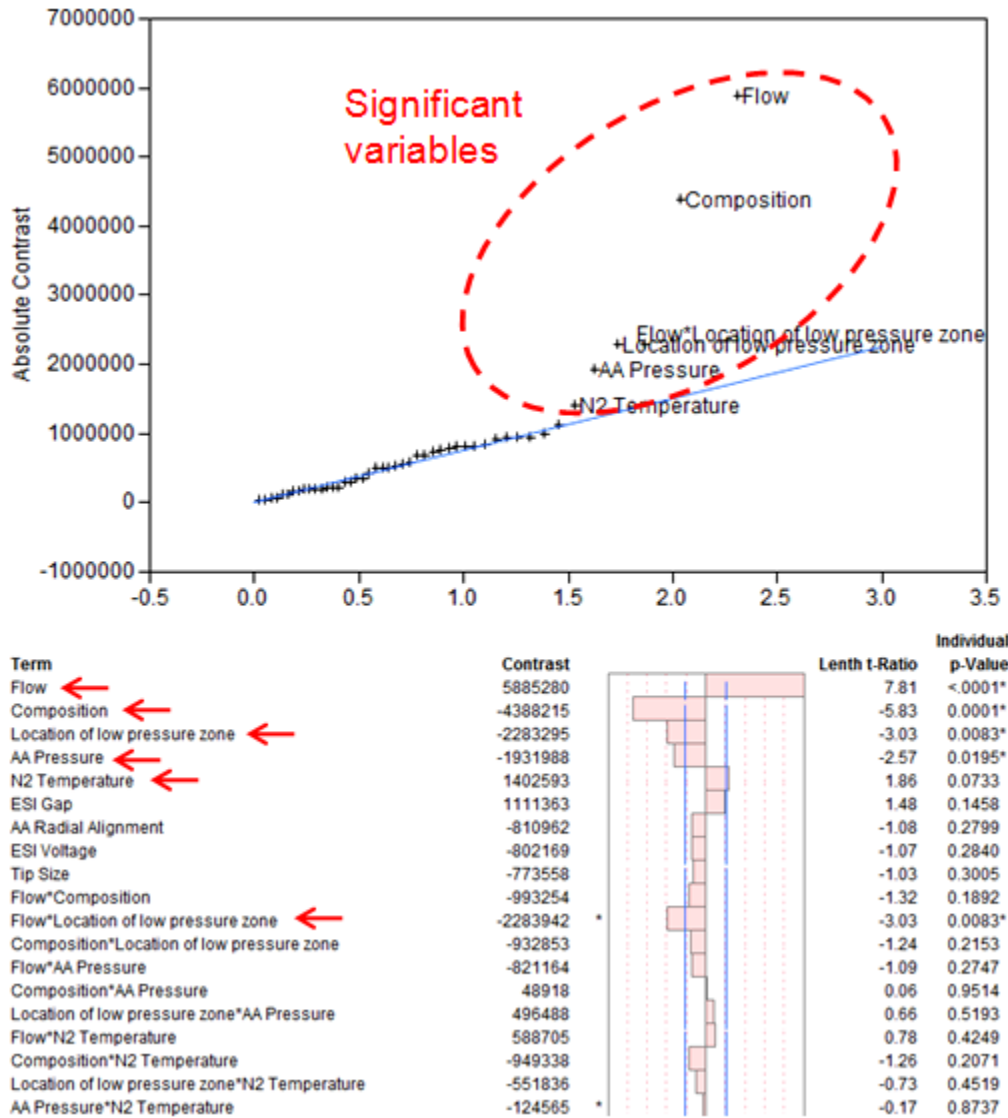


Figure 2-29. Half normal plot for FFD experiment

The conclusion of these experiments was:

- 1- It confirmed that better signal is obtained when the low vacuum zone is focused on the mass spectrometer inlet (radially and axially).
- 2- Value of ESI voltage does not have a significant impact on the results. Once electro-spray is established, increasing or lowering the voltage does not have a significant effect on the performance of the air amplifier. Voltage should be adjusted slightly above electrospray onset voltage for each experiment.
- 3- Tip size, flow size and solvent composition have an important contribution on the performance of the air amplifier. Better results were obtained were obtained with a 75 μm ESI tip, 2 $\mu\text{L}/\text{min}$ flow and higher organic solvent composition.

The objective of the next set of experiments was to compare the performance of the air amplifier at different combinations of flow and capillary tip size to the best performance without the air amplifier with a ESI gap of 3 mm (distance between emitter and MS inlet). 100% H_2O and 50% $\text{H}_2\text{O}/50\%$ ACN solvent compositions were both tested with 75 μm and 30 μm ESI emitter tips. For all tests, ESI voltage was set at 100 V above the electrospray onset voltage. Table 2-7 shows the different variable combinations that were tested for each of these 4 solvent/ESI emitter tip combinations. No significant signal improvement was achieved by using the air amplifier for 50% $\text{H}_2\text{O}/50\%$ ACN solvent composition when compared to the best result that can be obtained without using the air amplifier. At 100% H_2O solvent composition and 75 μm ESI emitter tips, the signal obtained without the air amplifier was below the noise level. However, using the air amplifier, it was possible to obtain a signal superior or equal to the signal obtained with a 30 μm tip and no air amplifier (see Figure 2-30). By averaging the sum of $(\text{M}+4\text{H})^{4+}$ and $(\text{M}+5\text{H})^{5+}$ signal for 124 measurements, a 34 fold improvement was obtained using the air amplifier under these conditions [27]. This result is important as it shows that ESI-MS can be performed at high flow regime and larger ESI tip using the air amplifier.

Table 2-7. Variable combinations that were tested during second serie of experiment

| | Pattern | ESI Gap (mm) | Temp (°C) | Flow (μL/min) | Pressure (psi) |
|----------|----------------|---------------------|------------------|----------------------|-----------------------|
| 1 | -+ -+ | 6 | 100 | 1 | 45 |
| 2 | ++++ | 9 | 100 | 2 | 45 |
| 3 | ++-- | 9 | 100 | 1 | 30 |
| 4 | --++ | 6 | 25 | 2 | 45 |
| 5 | ---- | 6 | 25 | 1 | 30 |
| 6 | -++- | 6 | 100 | 2 | 30 |
| 7 | +--+ | 9 | 25 | 1 | 45 |
| 8 | +--+ | 9 | 25 | 2 | 30 |

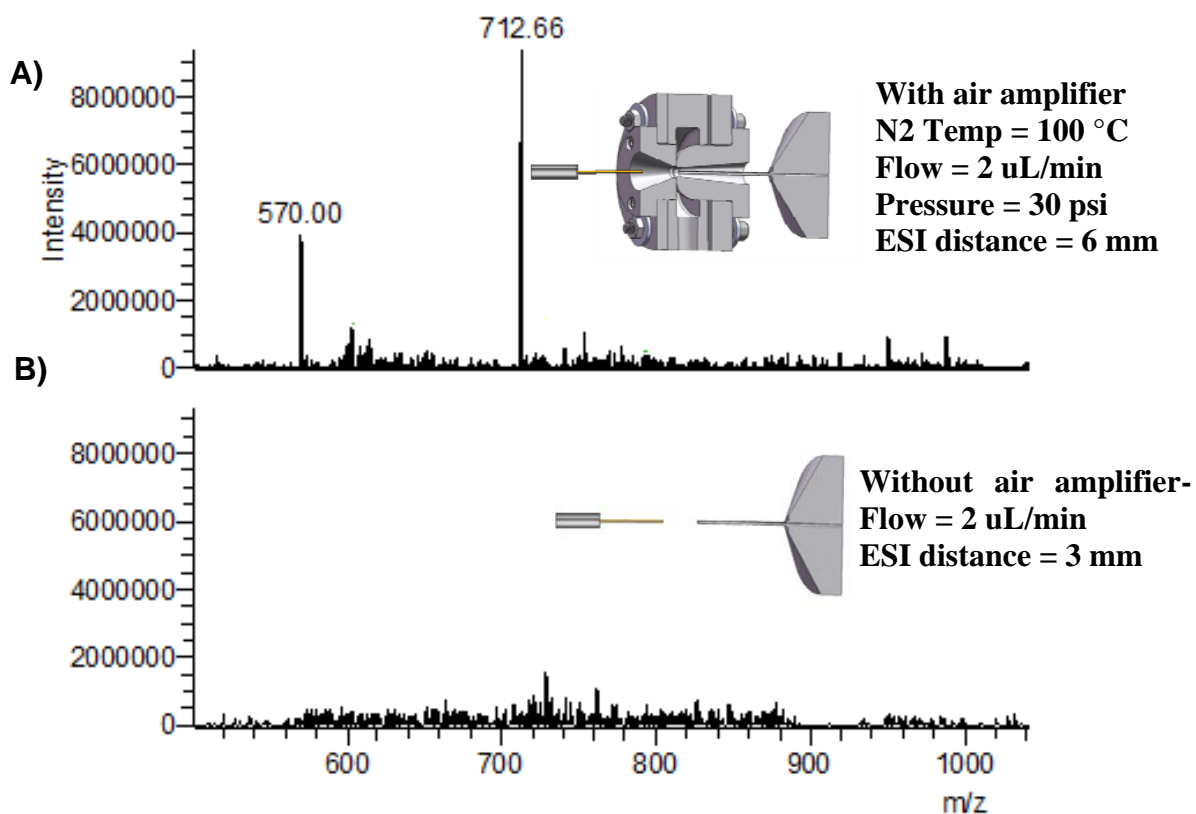


Figure 2-30. Mass spectrum comparison at 2 μL/min with and without the air amplifier

The ESI emitter tip size and solvent composition had a significant effect on the observed signal. Analysis of the results for each composition/tip combinations showed that except for the flow, none of the variables had a considerable effect on the results. This indicates that previous screenings successfully identified that the important variables and that the air amplifier was operating very close to its optimal condition.

3. AIR AMPLIFIER II

3.1 Design

A second iteration of the air amplifier was designed, fabricated and tested. One of the main objectives was to make the device more compact to reduce the length of the mass spectrometer inlet tube as shown on Figure 3-1. A longer tube significantly reduces the maximum signal that can be detected as it gives more opportunity for the ion to collide with walls during transportation. Also droplet desolvation process is slowed down in a cold capillary. A more compact air amplifier is now possible since it was demonstrated that the piezoelectric actuators could be taken out of the assembly. The CFD model was used to test different aerodynamic profiles and configurations. Because changes in the Coanda profile showed no significant signal improvement, the aerodynamic profile of the device stayed the same. Only the length of the inlet and outlet cones changed in to allow a shorter MS inlet tube. CFD model was also used to verify the effect of these changes in geometry on the signal and also how close the air amplifier could be positioned with respect to the MS inlet before it obstructed the flow. With the new design, it will now be possible to reduce the MS tube length by up to 75% (134 mm to 23 mm, depending on final outlet cone length).

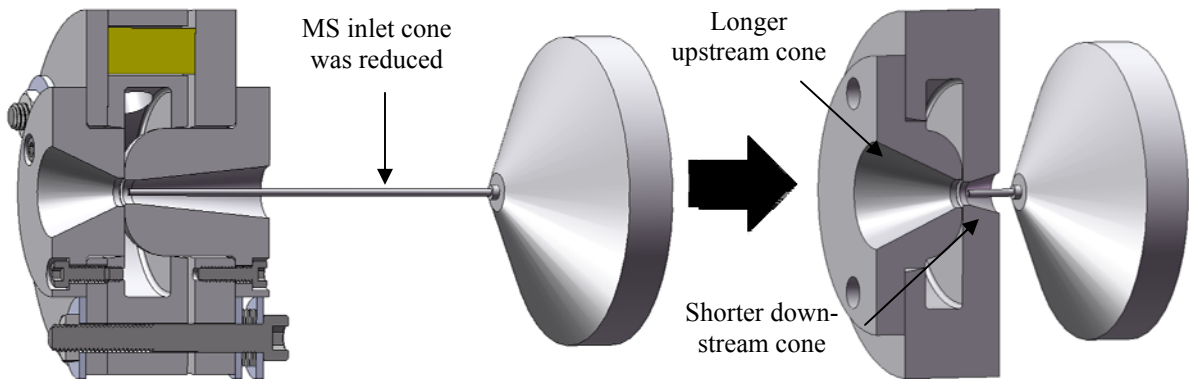


Figure 3-1. Reduction of MS inlet tube length

Air Amplifier II was also fabricated using Al 6061-T6. To minimize the outlet cone length, the focal point of the device (which was found earlier to be 1-2 mm downstream from the annular gap) was positioned as close to the MS inlet tip as possible. In other words, the outlet cone length was reduced. The annular gap was therefore moved from the upstream face of the plenum to the downstream face. Also, the new design has only one insert and the outlet cone was machined directly in the base plate. Not only does this allow a shorter outlet cone but it also eliminates the risk associated with the misalignment of the insert. To keep the plenum size the same, the upstream cone length had to be extended. Observation of pitot tube measurement performed on the first iteration indicated that the length of the upstream (intake) cone had little influence on the air flow profile. This hypothesis was also confirmed using the CFD model. However, the model indicated that a shorter outlet cone length would have a greater influence on the aerodynamic profile. According to model, a shorter outlet cone would mean that Coanda gas would be forced to be at atmospheric pressure before it had the chance to decelerate, creating vortices and back pressure that would interfere with the flow passing through the air amplifier.

Extensive work was made by the AECFD laboratory to include the charged particles in the model so that ion abundance can be predicted. The model did not predict a significant drop in abundance due to the shorter outlet cone. However, the charged particle model had not been fully validated at that time so it was decided to fabricate an air amplifier that had removable outlet so that effect of cone length can be determined experimentally.

Finite element analysis of the structure was used to verify that the plenum pressure would not cause significant increase of the annular gap. COSMOSWorks design analysis tool imbedded in SolidWorks® was used to perform the FEA. Final results are presented on Figure 3-2. Minimum cone length was determined to be 12 mm, for an expected increase in annular gap of 1.2 μm when plenum is pressurized to 45 psi (maximum operating pressure).

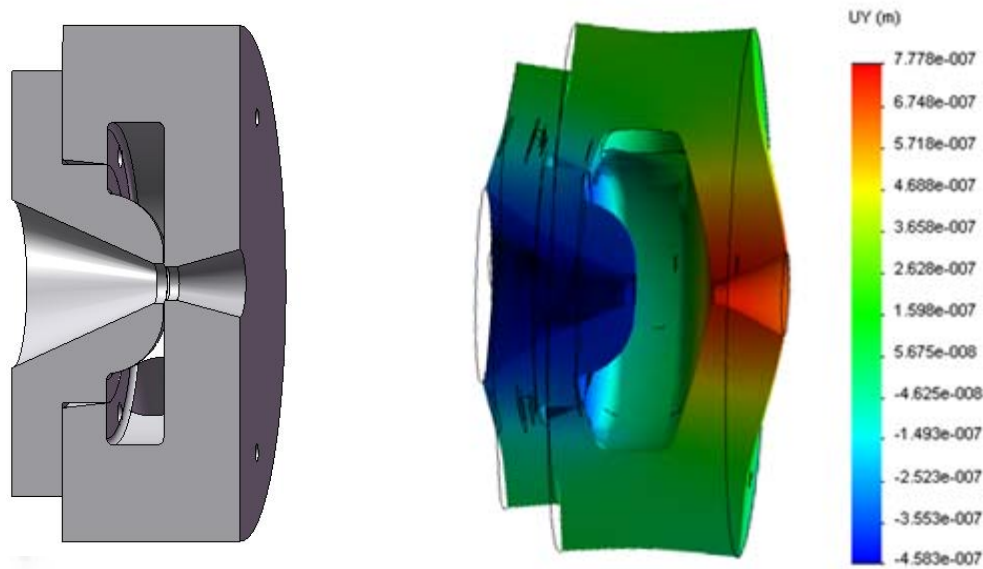


Figure 3-2. Next air amplifier outline and FEA results for a plenum pressure of 45 psi

3.2 Fabrication

Since there is no longer an insert at the outlet of the air amplifier (recall Figure 3-1), the Coanda radius is machined directly in the base of the device. As access is limited through the plenum, a custom diamond tool had to be designed to machine this radius. Machining simulation was performed using Solidworks® to ensure that there would be no interference between the tool holder and the part during machining of the Coanda radius. The tool needed a small included angle and a large sweep angle to machine the entire radius (90°) and also small enough to reach the back of the bore. The clearance under the tool tip also had to clear the lower part of the tool while machining the 5.15 mm OD. Additional lapping was required to create a relief angle under the tool to ensure that this clearance was achieved. Images of these simulation as well as details of custom made diamond tool are showed on Figure 3-3

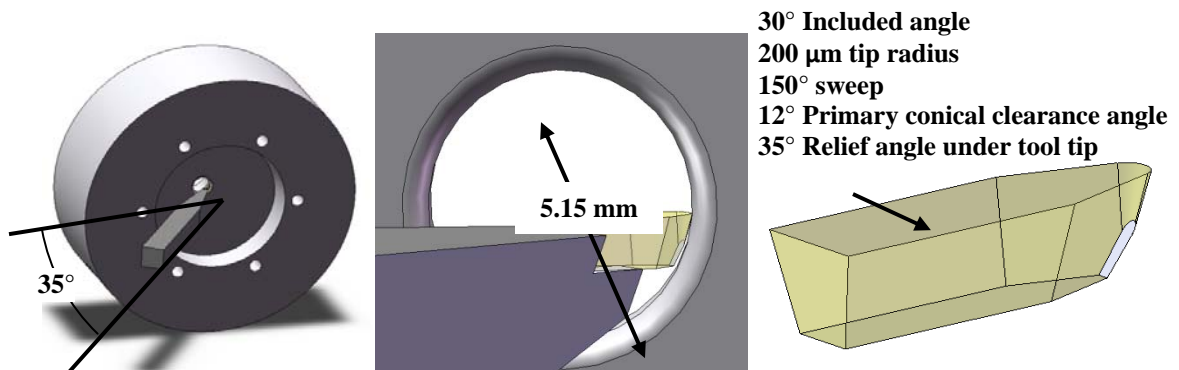


Figure 3-3. Simulation used to design custom made diamond tool and determine tool setup

The same procedure described in section 2.2 was used to machine the Coanda radius and the diametrical clearance GD1 (see Figure 3-4). The only major difference was the technique used to determine A1 and A2 that set the nominal annular gap of 50 μm . In Air Amplifier I, the presence of the piezoelectric actuators influenced the final height of the insert and the annular gap had to be measured using a Coordinate Measurement Machine. In this case, the tool position given by the Z axis encoder of the diamond turning machine was used to precisely measure A1 and A2 and set the annular gap to 50 μm .

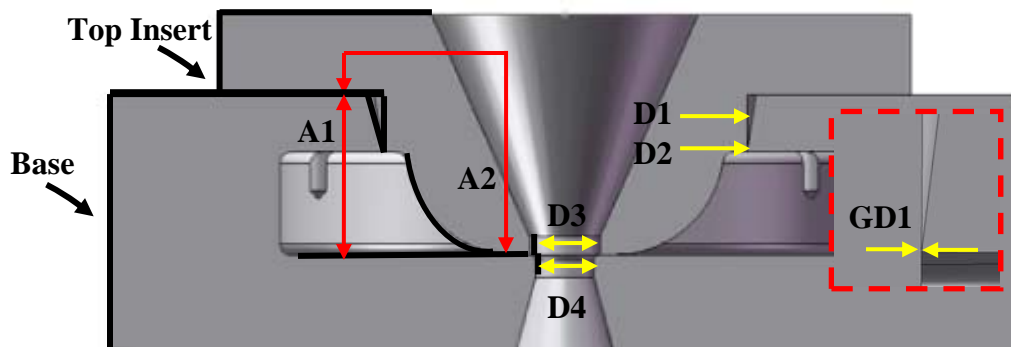


Figure 3-4. Diamond turned surfaces (bold) and measurement chain on new design of air amplifier

3.3 Testing

3.3.1 Static pressure measurement

Static pressure measurement for the Air Amplifier II were performed using a compound pressure transducer from Omegadyne (Sunbury, Ohio) with a range of ± 5 psig (± 5 V) and the same LVDT used in Section 2.3.2. A U-tube manometer was used to verify the accuracy of the pressure transducer when compared to the theoretical pressure generated by a column of water at 20°C (max measured error was 0.2%). With this setup it was possible to measure with greater resolution the pressure as a function of the position in the air amplifier.

In a first series of measurements, the static pressure profile was measured for different cone length. Results are presented on Figure 3-5. First it can be observed that the location of the focal point remains relatively unchanged (1-2 mm downstream of the annular gap) for different cone length. It can also be observed that the minimum pressure (maximum vacuum) decrease significantly as the cone length decreases. This phenomenon had been predicted by the CFD models. The back pressure causing interference with the flow can be clearly seen on measurement with cone length of 11.85 mm and 17.85 mm.

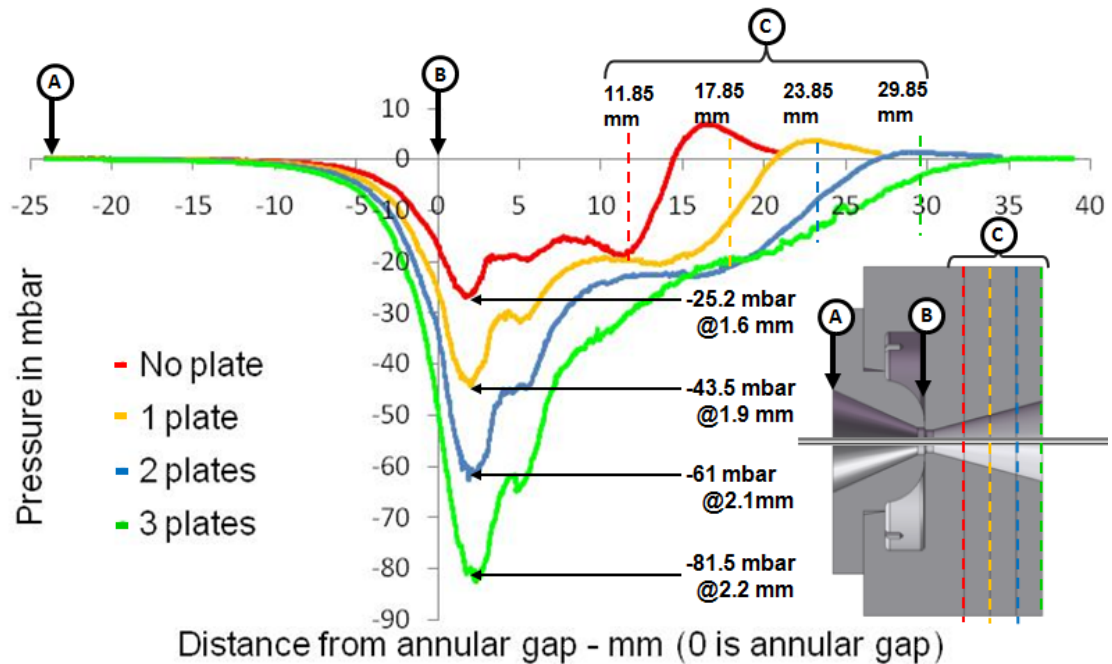


Figure 3-5. Static Pressure Measurement for 2nd iteration of air amplifier

Figure 3-6 shows the superposition of the pressure profiles for the first iteration of the air amplifier and the second iteration with all 3 extended cone sections (29.85 mm cone length). As the only difference in the geometry of both iterations of the air amplifier is the cone length, it is expected that the pressure profile of both iterations will be very similar, except for the maximum vacuum to be larger as cone length is longer. In **Figure 3-7**, maximum vacuum (minimum pressure) is plotted against the outlet cone length for 1st iteration of air amplifier and all 3 cone lengths measured for the Air amplifier II (same results as in Figure 3-5). The fact that results of Air Amplifier I and II lie on the same curve is a strong indication that annular gap width and Coanda profile is the same for both iteration and that precision of fabrication and dimensional control was adequate.

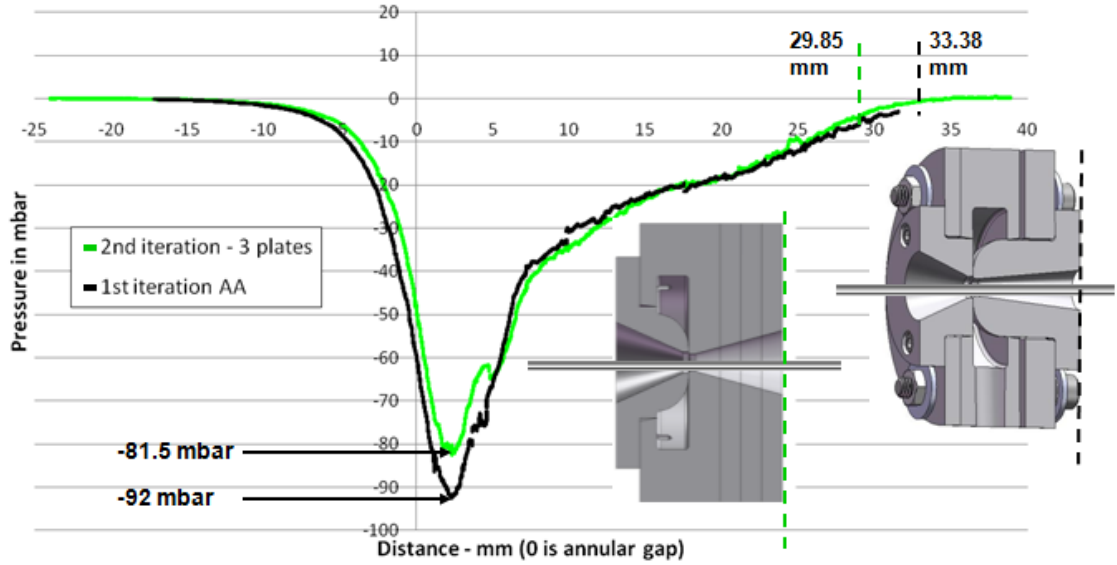


Figure 3-6. Pressure profile - 1st vs 2nd iteration

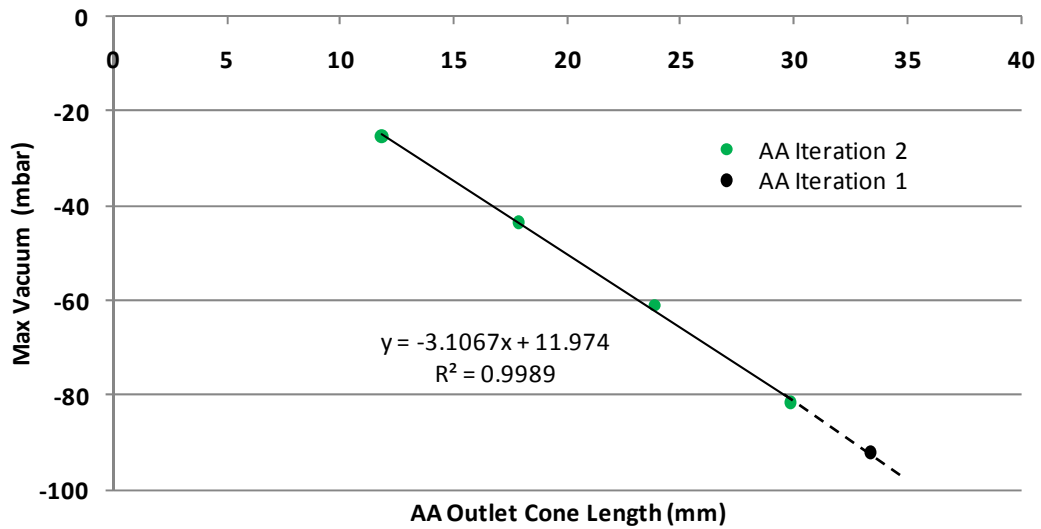


Figure 3-7. Maximum vacuum vs outlet cone length

As stated previously one of it was important to determine the minimum distance between the outlet of the air amplifier and the mass spectrometer inlet before it starts interacting with the flow in the air amplifier. To perform this measurement, the mass spectrometer inlet of a

LTQ MS from Thermos Fisher Scientific was mounted in front of the air amplifier on a xyz stage. The MS inlet xyz stage was mounted on the same stage than the air amplifier so that the inlet can be move either with respect to the air amplifier or together with it. The setup can be seen on Figure 3-8.

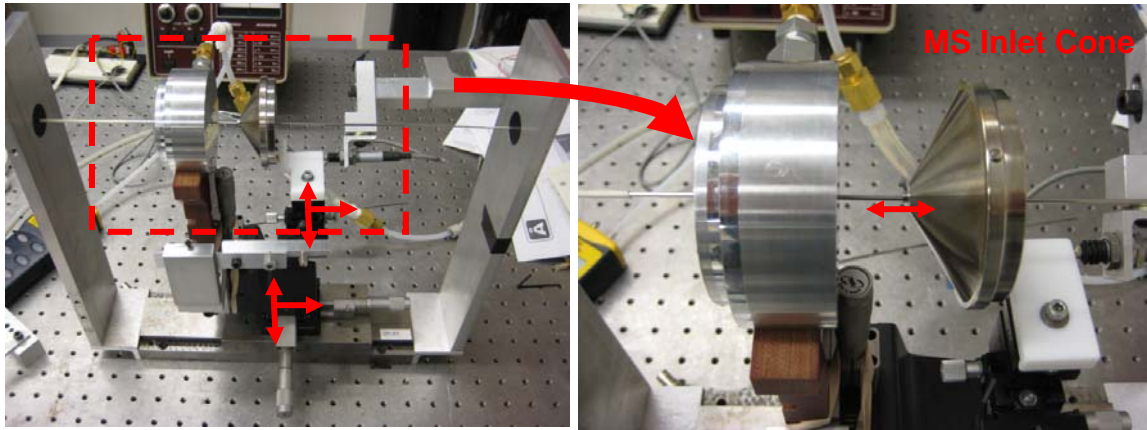


Figure 3-8. Test bench to measure the effect of MS inlet cone on aerodynamic profile

To see the effect of the distance between MS inlet and outlet cone shown on that figure, the pitot tube was first positioned at the point of maximum vacuum (1-2 mm downstream of annular gap). Then minimum static pressure as a function of the distance between the air amplifier outlet and the MS inlet was measured and plotted as show in Figure 3-9. This experiment was performed with different cone length (by adding outlet cone extensions). It was found that for every outlet cone lengths, the MS inlet was starting to obstruct the flow when gap between MS inlet and air amplifier outlet was smaller than 12 mm.

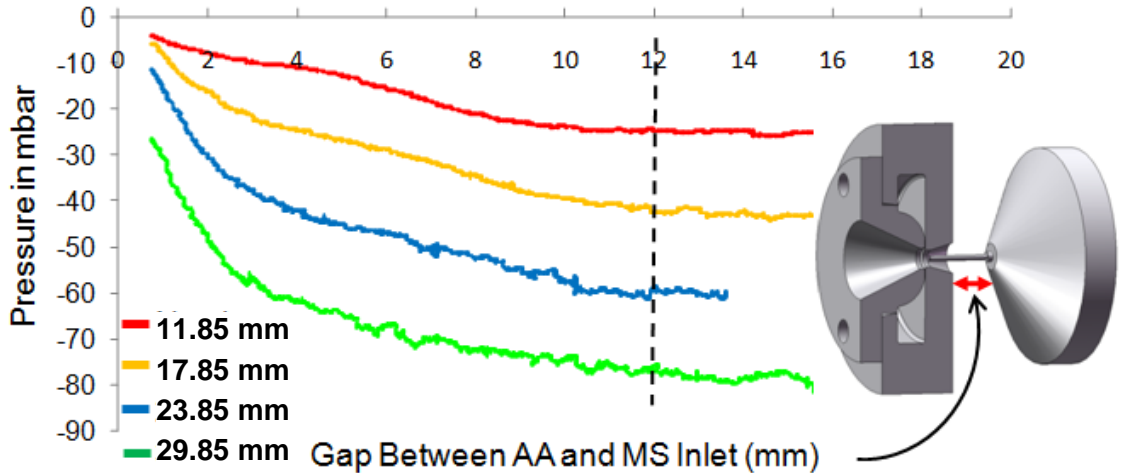


Figure 3-9. Pressure at focal point as a function of gap between MS inlet and air amplifier

One of the major issues with the commercial air amplifier that was used in previous experiments was the non-symmetrical radial air flow caused by the threaded design. A symmetrical air flow affects the consistency of the aerodynamic focal point. To measure the radial symmetry of the flow, stagnation pressure was measured at 1 mm from the outlet of the air amplifiers along the vertical and horizontal axis. These measurements were performed on both the new precision engineered air amplifier (Figure 3-10) and the threaded commercial version (Figure 3-11). For each figure, a 3D plot of the stagnation pressure as a function of the position is shown on the left. On these figures, the center of the air amplifier is 0 mm. Measurements were performed with a plenum pressure of 30 psi. Annular gap width for the new air amplifier was fixed at 50 μm and the one for the commercial air amplifier was estimated to be 60 μm . The pressure profiles in the 4 directions are superposed on the chart on the right. Pressure profile with commercial air amplifier is not symmetrical as radial location and magnitude of stagnation pressure profile are different in the 4 directions. Clear improvement is achieved with the precision machined air amplifier (test performed with Air Amplifier II).

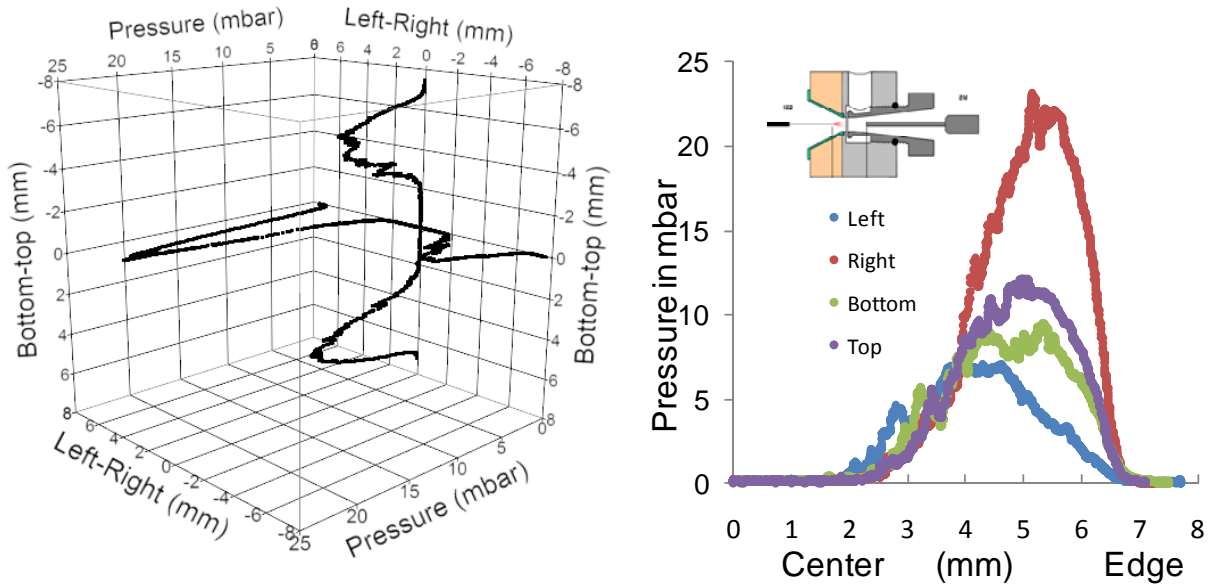


Figure 3-10. Stagnation pressure measured 1 mm from commercial air amplifier outlet (Left: 3D representation; Right: 4 axis superposed)

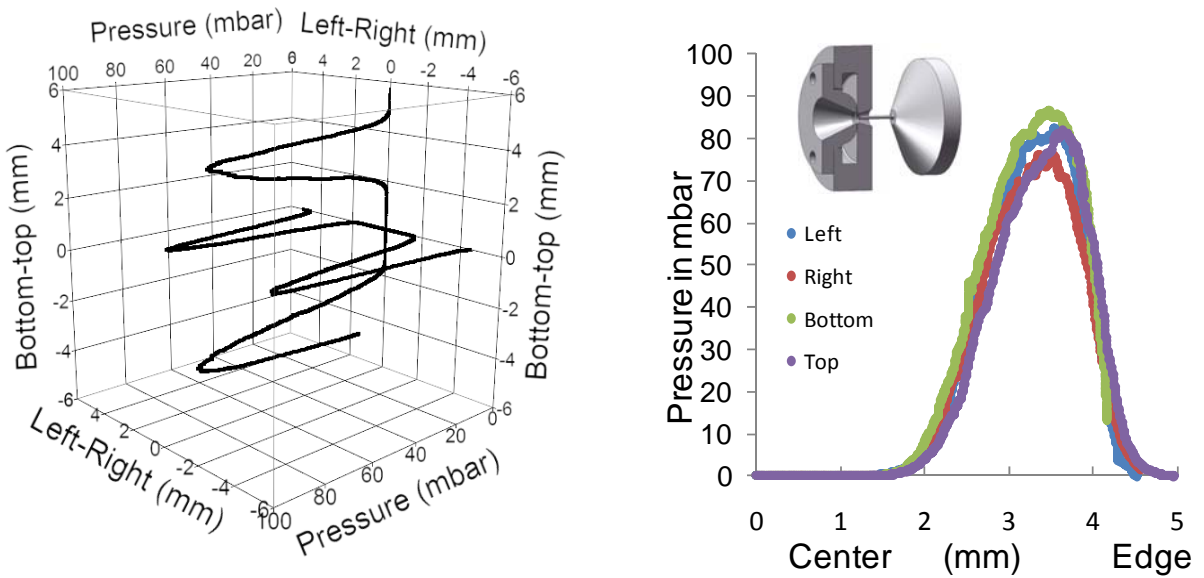


Figure 3-11. Stagnation pressure measured 1 mm from Air Amplifier II (Left: 3D representation; Right: 4 axis superposed)

3.3.2 LTQ-FTMS tests

The LTQ-FTMS has automatic gain control capability (AGC), meaning that it has the capability to collect a constant number of ions before performing the analysis. In other words, the higher the flow of ions getting into the mass spectrometer, the shorter the ion injection time will be. Therefore, the ion injection time can serve as a figure of merit to measure the ion abundance in the mass spectrometer and the performance of the air amplifier. Because there is significant abundance variation from scan to scan, quantile box plots were used to present these AGC data as shown on Figure 3-12.

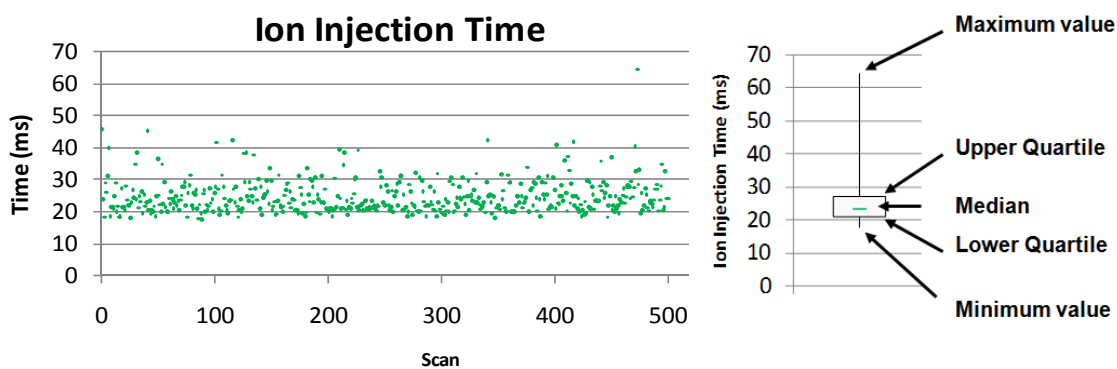


Figure 3-12. LTQ injection time data sample

One of the principal motivations for designing the Air Amplifier II was to reduce the length of the MS inlet tube. To obtain a point of comparison for the ion abundance, the base reference for abundance measurement without the air amplifier was performed. These measurements used the regular mass spectrometer inlet and not the extended mass spectrometer inlet designed to be used with the air amplifier. As shown on Figure 3-13, ion abundance decreased by about 3x when using the extended MS inlet of 43 mm is used.

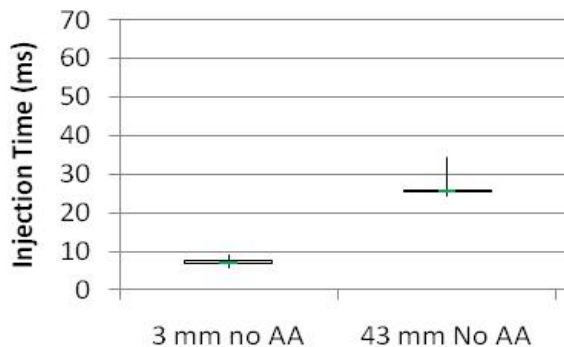


Figure 3-13. Ion injection time comparison with regular capillary

The 43 mm MS inlet length is only necessary if maximum air amplifier cone length is used. If cone extension lengths are removed, the MS inlet extended length can be reduced to 23 mm. Static pressure measurements performed in Section 3.3.1 showed that outlet cone length had a significant impact on the flow inside the air amplifier. To determine the effect of this change in flow inside the air amplifier on the ion abundance, measurements were performed under the same conditions, varying only the cone length of the air amplifier. Figure 3-14 shows that reducing the air amplifier cone length does not have any significant impact on the ion injection time or the abundance. For that reason, the remainder of the experiments will be performed without the cone length extension (total cone length of 11.85 mm) and the mass spectrometer inlet extension of 23 mm. A test identical to the one of Figure 3-13 was performed to determine once again the loss in signal due to 23 mm mass spectrometer inlet. The results showed slight but no significant improvement from the previous 43 mm inlet.

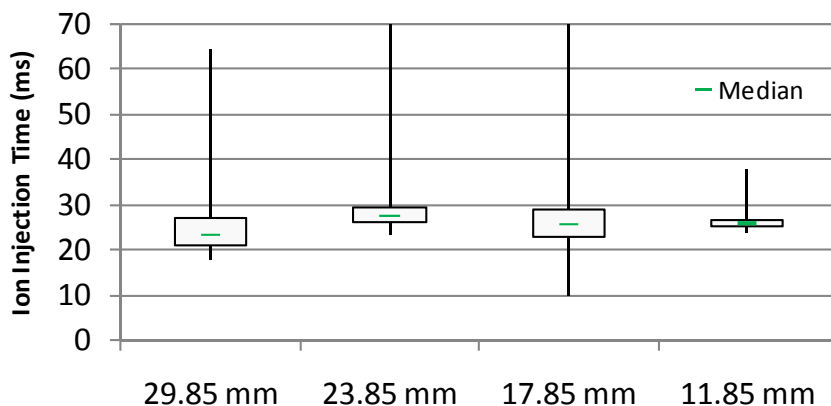


Figure 3-14. Ion injection time as a function of air amplifier cone length

As one of the possible causes for the loss in signal due to an extended capillary was the impact that the non heated capillary could have on the desolvation of the analyte. In order to test this hypothesis, a heating element was used to generate additional heat to the extended capillary. Several experiments have been performed with different heat inputs and results showed that no additional improvement could be obtained by heating the capillary. Pictures and results are presented in APPENDIX D – Heating of the Mass Spectrometer inlet. Results showed a loss in signal when additional heat was applied. This is a strong indication that the loss in signal caused by the extended capillary is not caused by a lack of desolvation. If analyte is already completely dissolved, additional heat energy will more likely cause analyte fragmentation. It therefore means that the loss in signal is only caused by the fact analyte has more opportunity to neutralize in a longer capillary and that the only way to resolve this issue would be to be able to use the regular inlet capillary with the air amplifier which is not possible when using the Air Amplifier.

A full factorial design was performed with the Air Amplifier II to validate the results found with Air Amplifier I. Experiments were performed with 500 nM concentration Cytochrome-C (equine) in a 100% H₂O / 0.2% formic acid buffer. The purpose was to verify the effect of the following variables: the ESI gap (1-3-6 mm), the flow (1-2 μ L), the presence of

the air amplifier (ON-OFF) and the ESI capillary size (30-100 μm). The different combinations tested are presented in

Table 3-1. Note that experiments have been performed in a random sequence. Results are presented in Figure 3-15.

Table 3-1. Full factorial performed on the second iteration of the air amplifier

| | ESI gap (mm) | Flow ($\mu\text{L}/\text{min}$) | AA | cap size (μm) | | ESI gap (mm) | Flow ($\mu\text{L}/\text{min}$) | AA | cap size (μm) |
|----|--------------|-----------------------------------|-----|----------------------------|----|--------------|-----------------------------------|-----|----------------------------|
| 1 | 1 | 1 | Off | 30 | 13 | 1 | 2 | Off | 100 |
| 2 | 1 | 2 | Off | 30 | 14 | 1 | 1 | Off | 100 |
| 3 | 3 | 1 | Off | 30 | 15 | 3 | 1 | Off | 100 |
| 4 | 3 | 2 | Off | 30 | 16 | 3 | 2 | Off | 100 |
| 5 | 6 | 1 | Off | 30 | 17 | 6 | 2 | Off | 100 |
| 6 | 6 | 2 | Off | 30 | 18 | 6 | 1 | Off | 100 |
| 7 | 1 | 2 | On | 30 | 19 | 1 | 1 | On | 100 |
| 8 | 1 | 1 | On | 30 | 20 | 1 | 2 | On | 100 |
| 9 | 3 | 1 | On | 30 | 21 | 3 | 1 | On | 100 |
| 10 | 3 | 2 | On | 30 | 22 | 3 | 2 | On | 100 |
| 11 | 6 | 2 | On | 30 | 23 | 6 | 2 | On | 100 |
| 12 | 6 | 1 | On | 30 | 24 | 6 | 1 | On | 100 |

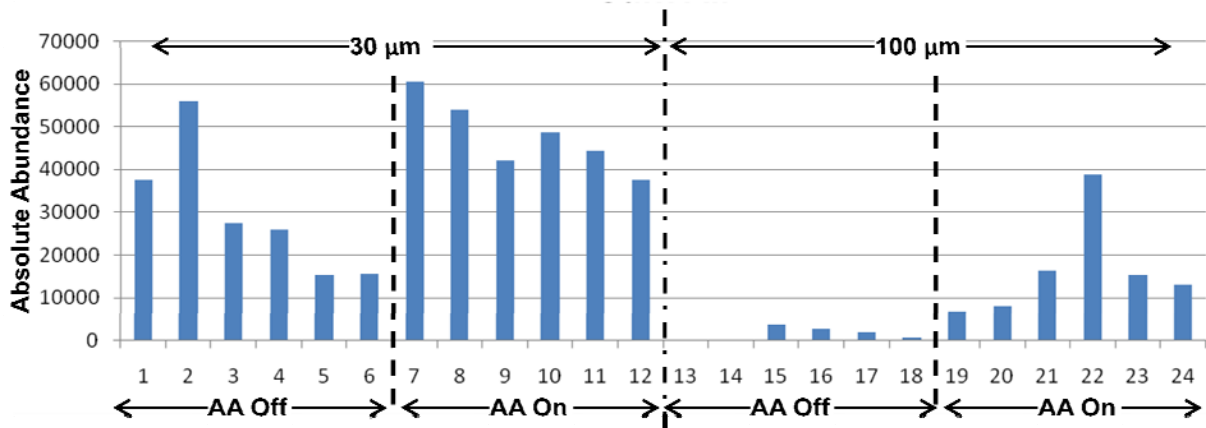
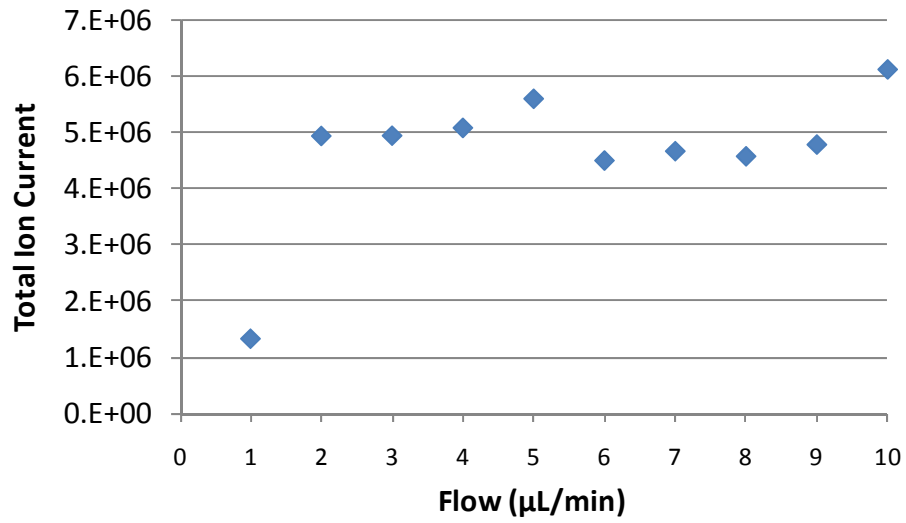


Figure 3-15. Full Factorial Design experiment results (sum of 19^+ , 9^+ and 8^+ of Cyt-C)

Those results are in accordance with what was discovered with the Air Amplifier I, i.e. that very little improvement was obtained with 30 μm ID ESI capillary and significant improvement is obtained at 100 μm ID ESI capillary, where no signal can be obtained without the air amplifier. This signal improvement for a larger tip opens the door to electrospray at higher flow. The maximum flow in a 30 μm capillary is 3 $\mu\text{L}/\text{min}$ but flow as high as 10 $\mu\text{L}/\text{min}$ are possible with the 100 μm capillary tip. However, the greater the flow rate, the larger the initial droplets formed during electrospray. Equation (3.1) shows the relationship between the capillary radius and the flow rate where ρ is the fluid density, Q is the flow rate and γ the surface tension of the fluid.

$$r \propto (\rho Q^2 \gamma)^{\frac{1}{3}} \quad (3.1)$$

This increase in initial droplet size signifies that more desolvation is necessary for the droplet to release their gas phase ions. Signal as a function of flow rate was measured at 2 different ESI distance with a 500 nM concentration Cytochrome-C (equine) in a 100% H_2O / 0.2% formic acid buffer. As can be seen on Figure 3-16, an increase in flow rate at 3 mm does not necessarily translate into an increase in abundance as total ion current remains constant. This indicates that a maximum desolvation threshold was reached and that even if flow and droplet size increase, 3 mm does not leave enough time/space for the droplet and desolvate. On the other hand, results at 6 mm ESI gap (Figure 3-17) show that total ion current still increase linearly with flow rate at 10 $\mu\text{L}/\text{min}$. Some losses are attributable to ESI distance, however increase in desolvation at larger ESI distance assisted by the air amplifier eventually compensate for the losses due to distance. As desolvation limit has not been reached yet at 6 mm, even better signal could be obtained at larger flow.



c

Figure 3-16. Total Ion Current as a function of flow rate at 3 mm ESI gap

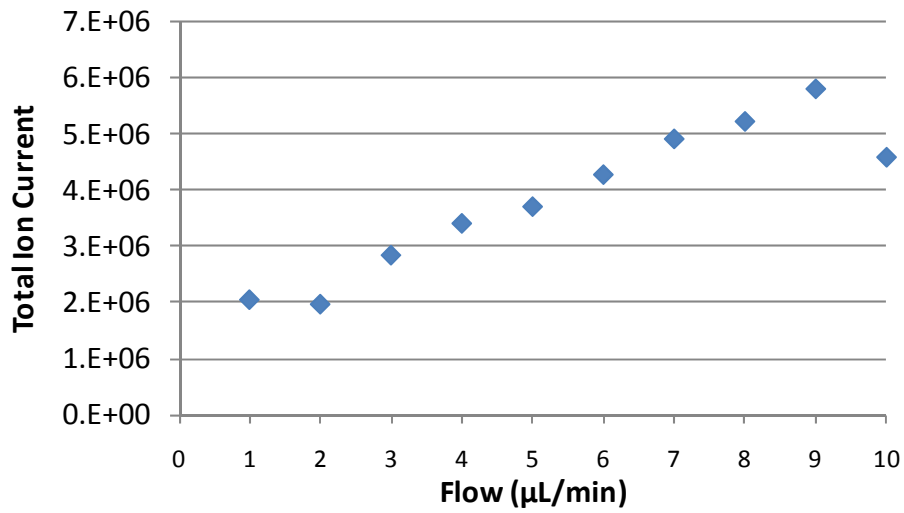


Figure 3-17. Total ion current as a function of flow rate at 6 mm ESI gap

4. CONCLUSION AND FUTURE WORK

- Air amplifier with piezoactuated annular gap was designed and successfully fabricated. This device allowed the effect of the annular gap width and plenum pressure on the velocity profile to be compared. It was determined that modulating the annular gap had the same effect on the aerodynamic profile as increasing the plenum pressure. Therefore, air amplifier can be fabricated with a fixed annular gap.
- Correlation between aerodynamic focal point (where gas velocity is maximum) and optimal axial position for MS inlet was established (1-2 mm downstream for both Air Amplifier I and II).
- Using fractional factorial design, variables that influence the performance of the air amplifier were identified. The experimental space where the air amplifier produced the best performance as been identified. Indeed, the result suggested that significant signal improvement (up to 34x) could be obtained when using the air amplifier with larger electrospray capillary tip and 100% H₂O buffer solvent composition. These results support the hypothesis that air amplifier does not only focus the ions but also helps with the desolvation of the droplets.
- A new iteration of the air amplifier, Air Amplifier II was designed and fabricated with a fixed annular gap of 50 μm and a shorter outlet cone so that signal losses due to MS capillary can be reduced. Additional experimental results confirmed that the air amplifier offers better signal improvement under conditions where desolvation rate is typically low (larger ESI capillary, larger flow and aqueous ESI solvent composition).
- Axial symmetry of precision engineered air amplifier was significantly improved when compared to the commercial device.

- Additional signal improvement could be obtained if the air amplifier could be used without having to change the mass spectrometer inlet capillary.

REFERENCES

1. Jonscher KR, Yates JR, "The Quadrupole Ion Trap Mass Spectrometer, A Small Solution To A Big Challenge", *Analytical Biochemistry*, Volume 244 (1997) pp. 1–15
2. Amster J, "Fourier Transform Mass Spectrometry", *Journal of Mass Spectrometry*, Vol. 31 (1996) pp. 1325-1337
3. Schwartz et Al., "A Two-Dimensional Quadrupole Ion Trap Mass Spectrometer", *J Am Soc Mass Spectrom*, Volume 13 (2002) pp. 659–669
4. Nadja, C. and Christie, E., "Practical Implications of Some Recent Studies in Electrospray Ionization Fundamentals", *Mass Spectrometry Reviews*. Volume 20 (2001) pp. 362-387.
5. Yamashita, M. and Fenn, B, "Electrospray Ion Source. Another Variation on the Free Jet Theme", *The Journal of Physical Chemistry*. Volume 88 Issue 20 (1984) pp. 4451-4459.
6. Fenn B. and Al., "Electrospray Ionization for Mass Spectrometry of Large Biomolecules", *Science*, Vol. 246 (1989) pp. 64-71.
7. J.B. Fenn, M. Mann, C.K. Meng, S.F. Wong and C.M. Whitehouse, Electrospray ionization for mass-spectrometry of large biomolecules, *Science* 246 (4926) (1989), pp. 64–71
8. J.B. Fenn, M. Mann, C.K. Meng, S.F. Wong and C.M. Whitehouse, Electrospray ionization—principles and practice, *Mass Spectrom. Rev.* 9 (1) (1990), pp. 37–70
9. A. P. Bruins, "Mass Spectrometry with Ion Sources operating at Atmospheric pressure", *Mass Spectrometry Review*. Volume 10 (1991) pp. 53-77.
10. Dole M., Mack L.L., Hines R.L., Mobley R.C., Ferguson L.D. and M.B. Alice, "Molecular beams of macroions", *The Journal of Physical Chemistry*. Volume 49 Issue 5 (1968) pp 2240–2249.

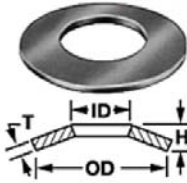
11. Iribarne J.V. and Thomson B.A. "On the evaporation of small ions from charged droplets" *The Journal of Chemical Physics*. Volume 64 Issue 5 (1976) pp 2287-2294.
12. 57th American Society for Mass Spectrometry Conference 2009, Philadelphia, PA. "Development of an Air Amplifier Assisted Protein-Cleavage Isotope Dilution Mass Spectrometry Method for Prostate Specific Antigen in the Nano-Flow Regime", R. B. Dixon, D. K. Williams Jr., D. Cassidy, J. R. Edwards, G. Robichaud, A. Sohn, T. A. Dow, D. C. Muddiman.
13. Shaffer SA, Tang KQ, Anderson GA, Prior DC, Udseth HR, Smith RD. "A Novel Ion Funnel for Focusing Ions at Elevated Pressure Using Electrospray Ionization Mass Spectrometry" *Rapid Commun Mass Spectrom* Volume 11 Issue 16 (1997) pp. 1813–1817.
14. Him T, Tolmachev AV, Harkewicz R, Prior DC, Anderson G, Udseth HR, Smith RD, Bailey TH, Rakov S, Futrell JH. Design and Implementation of a New Electrodynamic Ion Funnel." *Anal Chem*. Volume 72 Issue 10 (2000) pp. 2247–2255.
15. Kim T, Udseth HR, Smith RD." Improved Ion Transmission from Atmospheric Pressure to High Vacuum Using a Multicapillary Inlet and Electrodynamic Ion Funnel Interface". *Anal Chem*. Volume 72 Issue 20 (2000) pp. 5014–5019.
16. Buryakov IA, Krylov EV, Nazarov EG, Rasulev UK. "A New Method of Separation of Multi-Atomic Ions by Mobility at Atmospheric-Pressure Using a High-Frequency Amplitude-Asymmetric Strong Electric-Field". *Int J Mass Spectrom Ion Phys*. Volume 128 Issue 3 (1993) pp. 143–148
17. Purves RW, Guevremont R. Electrospray Ionization High-Field Asymmetric Waveform Ion Mobility Spectrometry-Mass Spectrometry. *Anal Chem* Volume 71 Issue 13 (1999) pp. 2346–2357
18. Dixon, R.B., Muddiman, D.C., "Probing the Mechanisms of an Air Amplifier using a LTQ-FT-ICRMS and Fluorescence Spectroscopy" *Rapid Commun. Mass Spectrom*. Volume 21 Issue 19 (2007) pp3207-3212
19. Zhou L, Yue BF, Dearden DV, Lee ED, Rockwood AL, Lee ML. "Incorporation of a Venturi Device in Electrospray Ionization" *Anal Chem*. Volume 75 Issue 21 (2003) pp. 5978–5983.

20. Adam M. Hawkrige, Li Zhou, Milton L. Lee, and David C. Muddiman, “Analytical Performance of a Venturi Device Integrated into an Electrospray Ionization Fourier transform Ion Cyclotron Resonance Mass Spectrometer for Analysis of Nucleic Acids” *Anal. Chem.* Volume 76 Issue 14 (2004) pp 4118–4122
21. Dixon, R.B., “The Development and Utilization of Aerodynamic Devices in Biological Mass Spectrometry” Ph.D. Thesis, North Carolina State University, 2009
22. Zdanowicz, E.M., “Design of a Fast Long Range Actuator – Flora II” M.S. Thesis, North Carolina State University, 2010
23. Dow, Thomas A. and Sohn, A. “Metrology in Precision Manufacturing – Laboratory Notes.”
24. Gerchman, Mark Craig: “Optical Tolerancing for Diamond Turning Ogive Error”, Rank Taylor Hobson, Inc., Keene, NH 03431
25. Sohn A., “Diamond Tool Centering for Diamond Turning”, *Proceedings of Annual Meeting of the ASPE*, (2009)
26. NIST/SEMATECH, e-Handbook of Statistical Methods, <http://www.itl.nist.gov/div898/handbook/>, 7/18/2006
27. Robichaud G. et al., Design, Modeling, Fabrication, and Evaluation of the Air Amplifier for Improved Detection of Biomolecules by Electrospray Ionization Mass Spectrometry, *Int. J. Mass Spectrom.* Issue 300 (2011) pp. 99-107

APPENDIX

APPENDIX A – First Iteration Air Amplifier Parts and Drawings

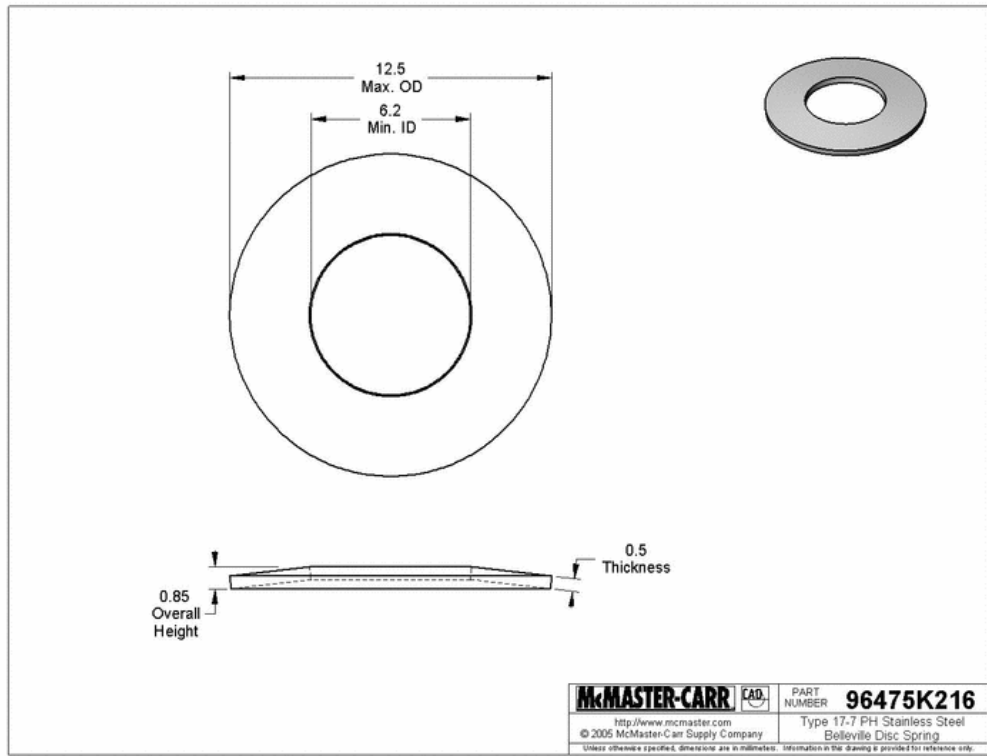
Disc Springs



Part Number: **96475K216**

\$7.71 per Pack of 12

| | |
|--------------------------|---------------------------------|
| Type | Belleville Disc Springs |
| Material | Stainless Steel |
| Stainless Steel Type | 17-7 PH Stainless Steel |
| Minimum Inside Diameter | 6.2 mm |
| Maximum Outside Diameter | 12.5 mm |
| Thickness | .50 mm |
| Overall Height | .85 mm |
| Load | 357 N |
| Load Tolerance | ±20% |
| Deflection at Load | .32 mm |
| Flat Load | 387 N |
| Specifications Met | Deutsche Industrie Normen (DIN) |
| DIN Specifications (DIN) | DIN 2093 |



PZT Stack Actuators

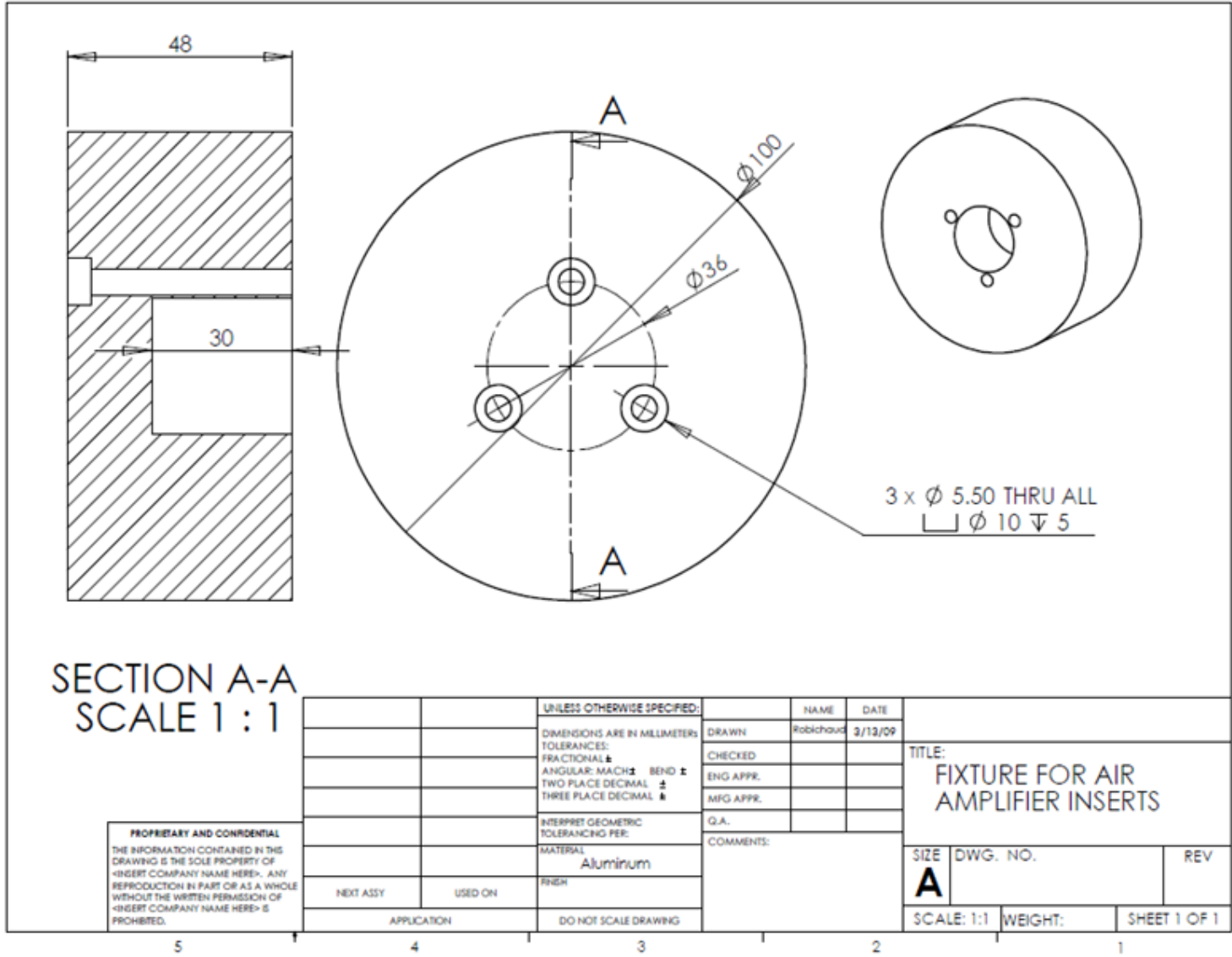
In addition to a wide range of standard sizes, Piezomotor® actuators can be fabricated in custom configurations to exactly match special requirements with fast turnaround times. Standard sizes range from 700 to 28,000 Newtons force and from 10 to 200 microns displacement.



| PZWT100 Properties | | | |
|--------------------|------------------------|-----------------------|------------------------|
| K_p | 0.64 | Y_{11D} | $6.9E10 \text{ N/m}^2$ |
| K_{31} | 0.37 | Tan δ | 0.027 |
| K_t | 0.56 | ρ | 7.8 g/cc |
| d_{31} | -170E-12 m/V | T_{curie} | >360°C |
| d_{33} | 370E-12 m/V | Poisson's ratio: | 0.3 |
| g_{31} | -13E-3 m/N | Dielectric Constant: | Krel=2500 |
| Y_{11E} | $6.2E10 \text{ N/m}^2$ | Strain: 0-2.0 Mv/m | 1500 microstrain typ. |
| Y_{33E} | $4.8E10 \text{ N/m}^2$ | Strain: -0.6-2.4 Mv/m | 2800 microstrain |

| Part No | Block Force | Displacement | Stack Length | Capacitance | Res. Freq. kHz |
|---------|-------------|--------------|--------------|-------------|----------------|
| D1CM20 | 2800N | 20 μ m | 0.815" | .13 μ F | 68 |

Kinetic Ceramics, Inc.
 Telephone: 510-264-2140
 Fax: 510-264-2159
 26240 Industrial Blvd. Hayward CA 94545
WWW.kineticceramics.com

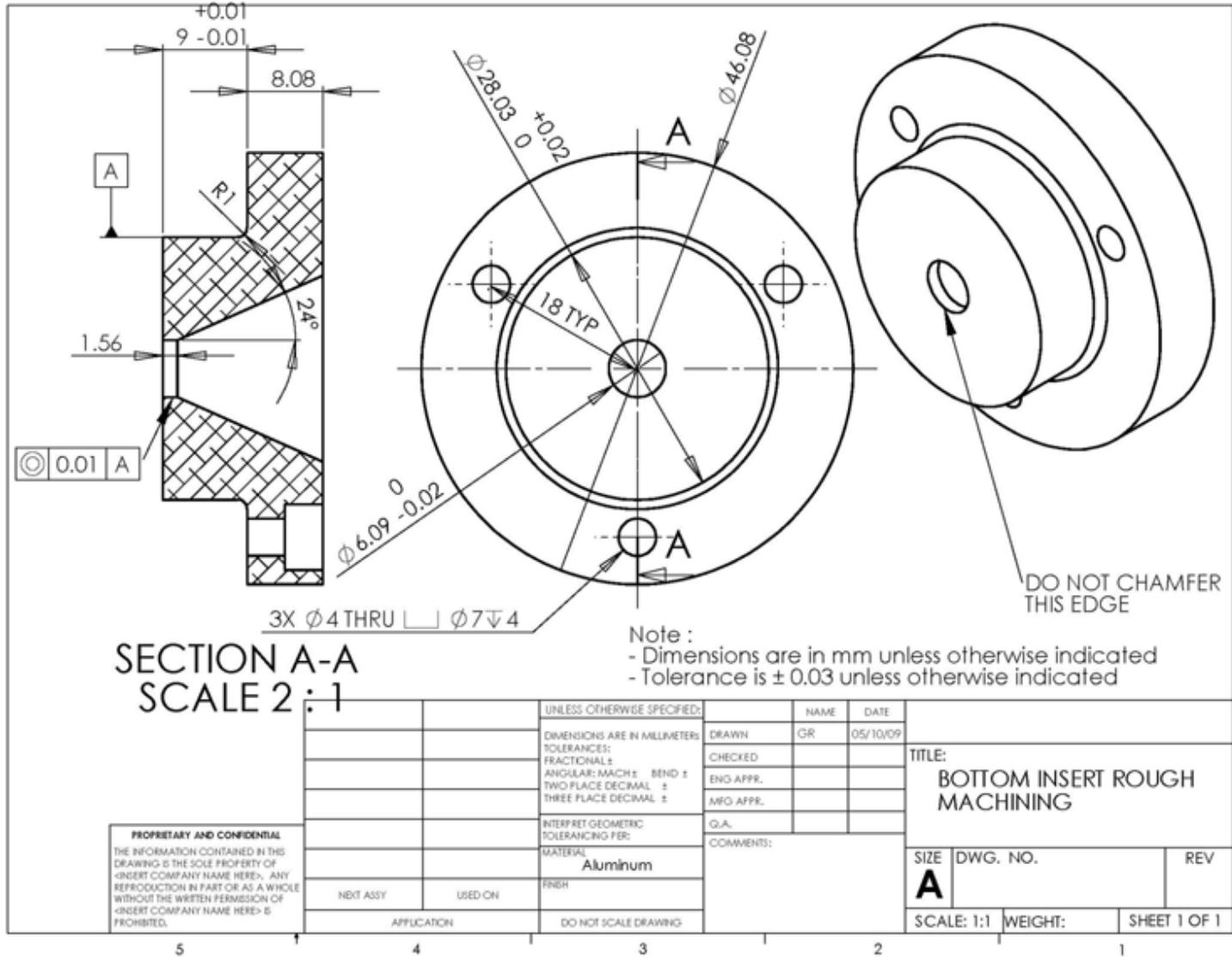


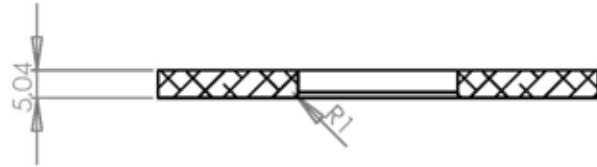
SECTION A-A
SCALE 1 : 1

PROPRIETARY AND CONFIDENTIAL
THE INFORMATION CONTAINED IN THIS DRAWING IS THE SOLE PROPERTY OF <INSERT COMPANY NAME HERE>. ANY REPRODUCTION IN PART OR AS A WHOLE WITHOUT THE WRITTEN PERMISSION OF <INSERT COMPANY NAME HERE> IS PROHIBITED.

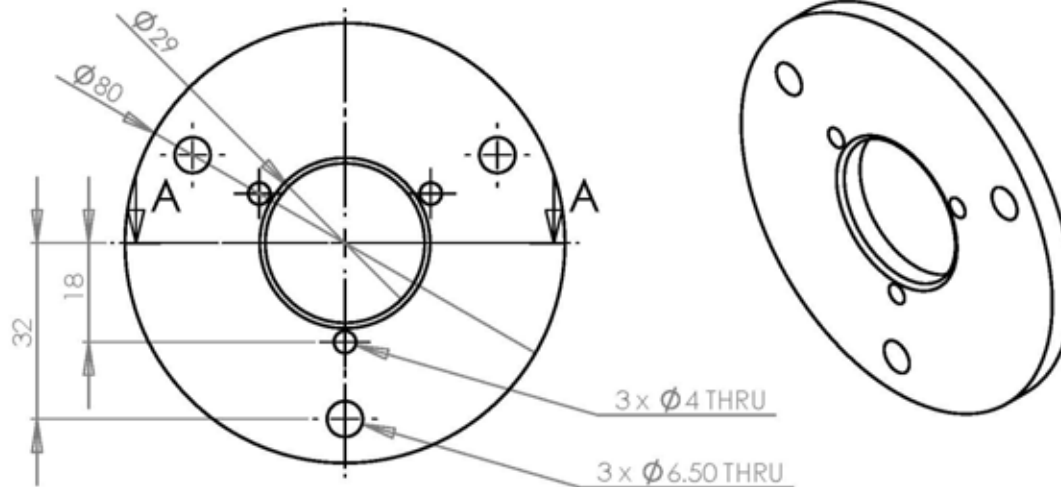
| | | | | | | | |
|-------------|--|--|--|-----------|-----------|--|--|
| | | UNLESS OTHERWISE SPECIFIED: | | NAME | DATE | | |
| | | DIMENSIONS ARE IN MILLIMETERS | | DRAWN | Robichaud | 2/13/09 | |
| | | TOLERANCES: | | CHECKED | | TITLE: FIXTURE FOR AIR AMPLIFIER INSERTS | |
| | | FRACTIONAL ± | | ENG APPR. | | | |
| | | ANGULAR: MATCH ± BEND ± | | MFG APPR. | | | |
| | | TWO PLACE DECIMAL ± THREE PLACE DECIMAL ± | | Q.A. | | | |
| | | INTERPRET GEOMETRIC TOLERANCING PER: | | COMMENTS: | | SIZE DWG. NO. REV | |
| | | MATERIAL | | | | A | |
| | | Aluminum | | | | | |
| NEXT ASSY | | USED ON | | | | | |
| APPLICATION | | DO NOT SCALE DRAWING | | | | SCALE: 1:1 WEIGHT: SHEET 1 OF 1 | |

5 4 3 2 1





SECTION A-A
SCALE 1:1



| | | | | | | |
|-------------|---------|--------------------------------------|--|------------|----------|--------------|
| | | UNLESS OTHERWISE SPECIFIED: | | NAME | DATE | |
| | | DIMENSIONS ARE IN MILLIMETERS | | DRAWN | Furst | 12/2/06 |
| | | TOLERANCES: | | CHECKED | | |
| | | FRACTIONAL: \pm | | ENG APPR. | | |
| | | ANGULAR: MACH: \pm BEND: \pm | | MPG APPR. | | |
| | | TWO PLACE DECIMAL: \pm | | Q.A. | | |
| | | THREE PLACE DECIMAL: \pm | | COMMENTS: | | |
| | | INTERPRET GEOMETRIC TOLERANCING PER: | | | | |
| | | MATERIAL: Aluminum | | | | |
| | | FINISH: | | | | |
| NEXT ASSY | USED ON | | | | | |
| APPLICATION | | DO NOT SCALE DRAWING | | | | |
| | | | | SIZE | DWG. NO. | REV |
| | | | | A | BottomM | |
| | | | | SCALE: 1:1 | WEIGHT: | SHEET 1 OF 1 |

PROPRIETARY AND CONFIDENTIAL
THE INFORMATION CONTAINED IN THIS DRAWING IS THE SOLE PROPERTY OF <INSERT COMPANY NAME HERE>. ANY REPRODUCTION IN PART OR AS A WHOLE WITHOUT THE WRITTEN PERMISSION OF <INSERT COMPANY NAME HERE> IS PROHIBITED.

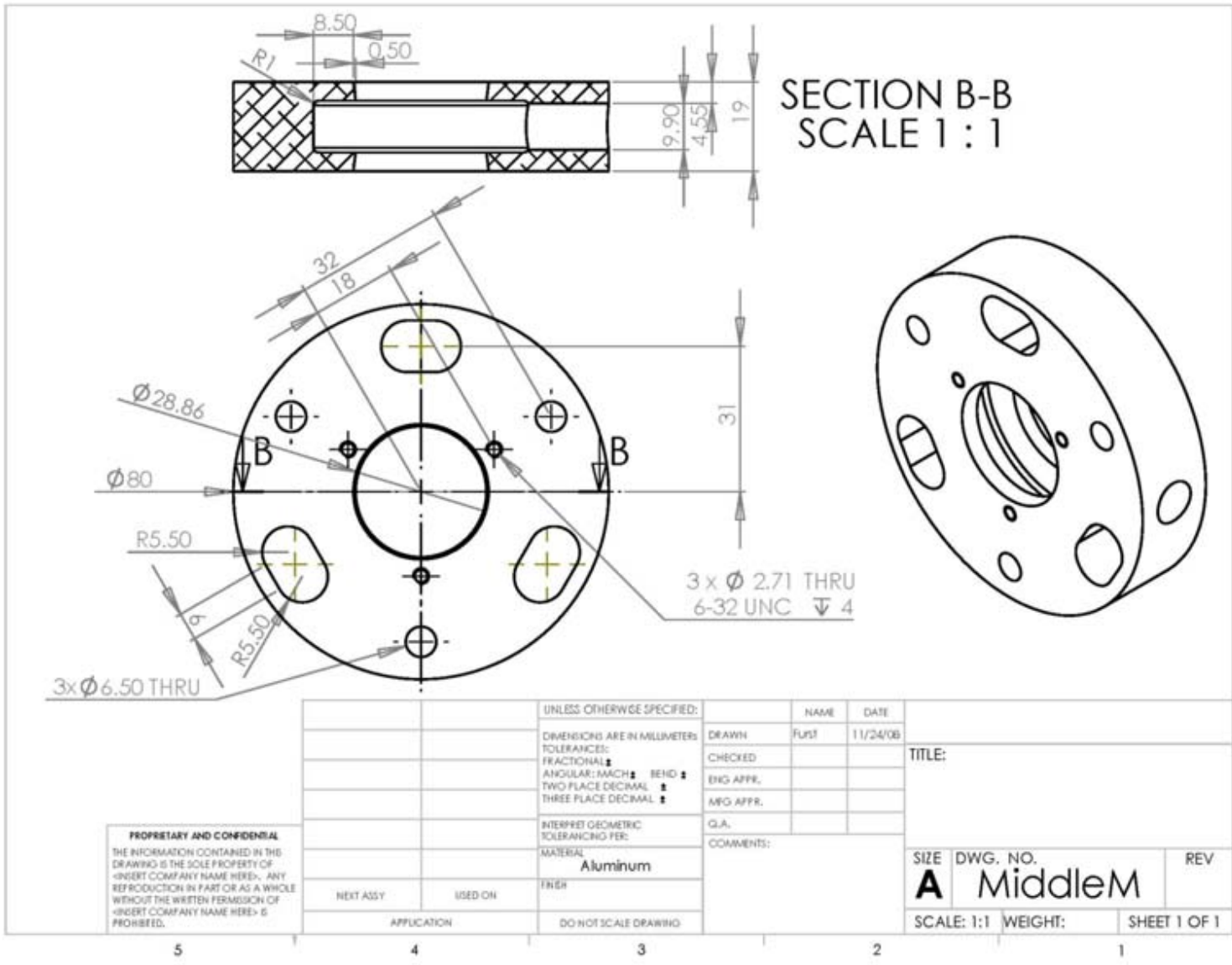
5

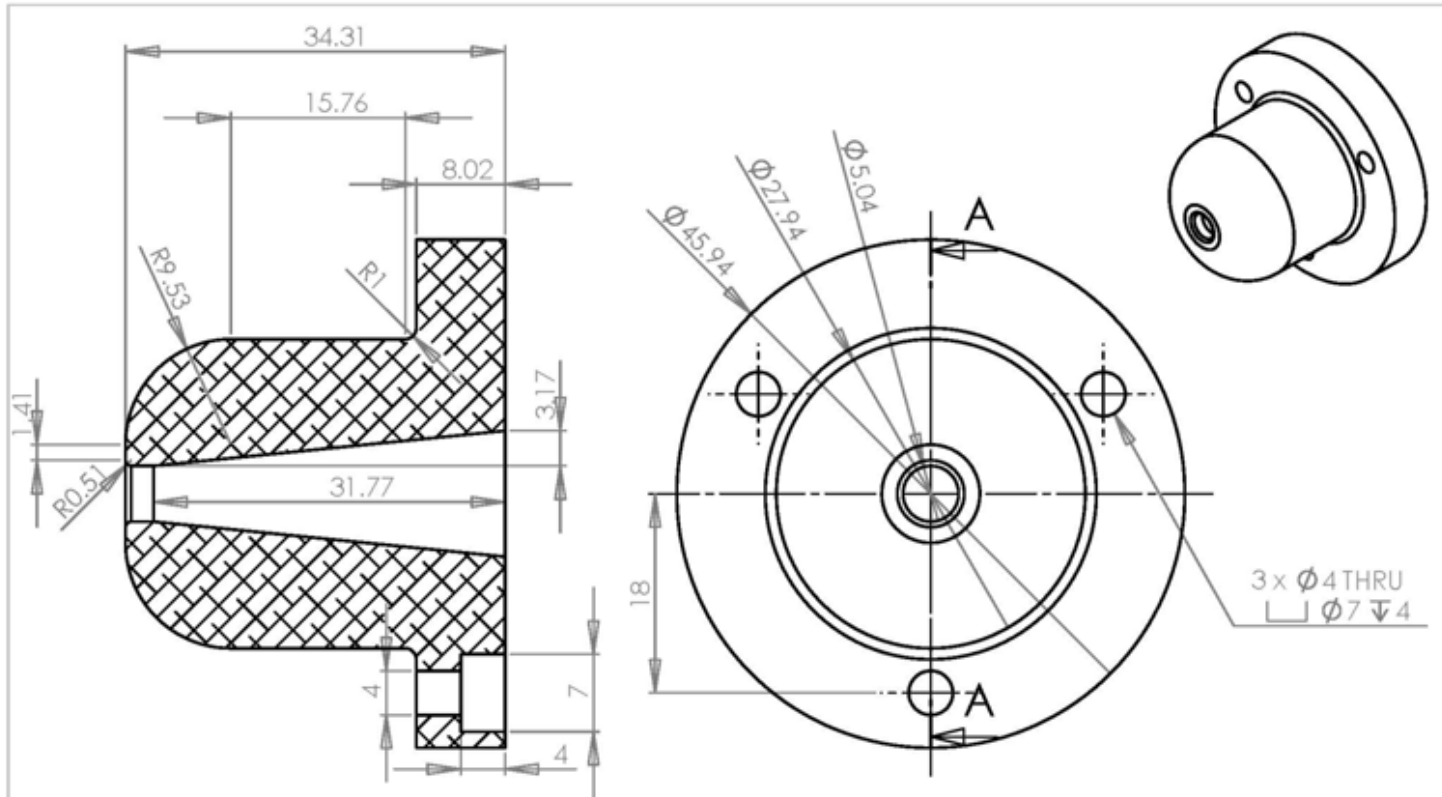
4

3

2

1





SECTION A-A
SCALE 2:1

PROPRIETARY AND CONFIDENTIAL
THE INFORMATION CONTAINED IN THIS DRAWING IS THE SOLE PROPERTY OF <INSERT COMPANY NAME HERE>. ANY REPRODUCTION IN PART OR AS A WHOLE WITHOUT THE WRITTEN PERMISSION OF <INSERT COMPANY NAME HERE> IS PROHIBITED.

| | | | | | |
|--------------------------------------|---------|----------------------|------|----------|---------------------------------|
| UNLESS OTHERWISE SPECIFIED: | | NAME | DATE | | |
| DIMENSIONS ARE IN MILLIMETERS | | DRAWN | Fus1 | 11/24/08 | |
| TOLERANCES: | | CHECKED | | | TITLE: |
| FRACTIONAL: $\frac{1}{16}$ | | ENG APPR. | | | |
| ANGULAR: MACH: \pm BEND: \pm | | MFG APPR. | | | |
| TWO PLACE DECIMAL: \pm | | Q.A. | | | |
| THREE PLACE DECIMAL: \pm | | COMMENTS: | | | |
| INTERPRET GEOMETRIC TOLERANCING PER: | | | | | |
| MATERIAL: | | | | | SIZE DWG. NO. REV |
| Aluminum | | | | | A TopInsertM |
| NEXT ASSY | USED ON | | | | SCALE: 2:1 WEIGHT: SHEET 1 OF 1 |
| APPLICATION | | DO NOT SCALE DRAWING | | | |

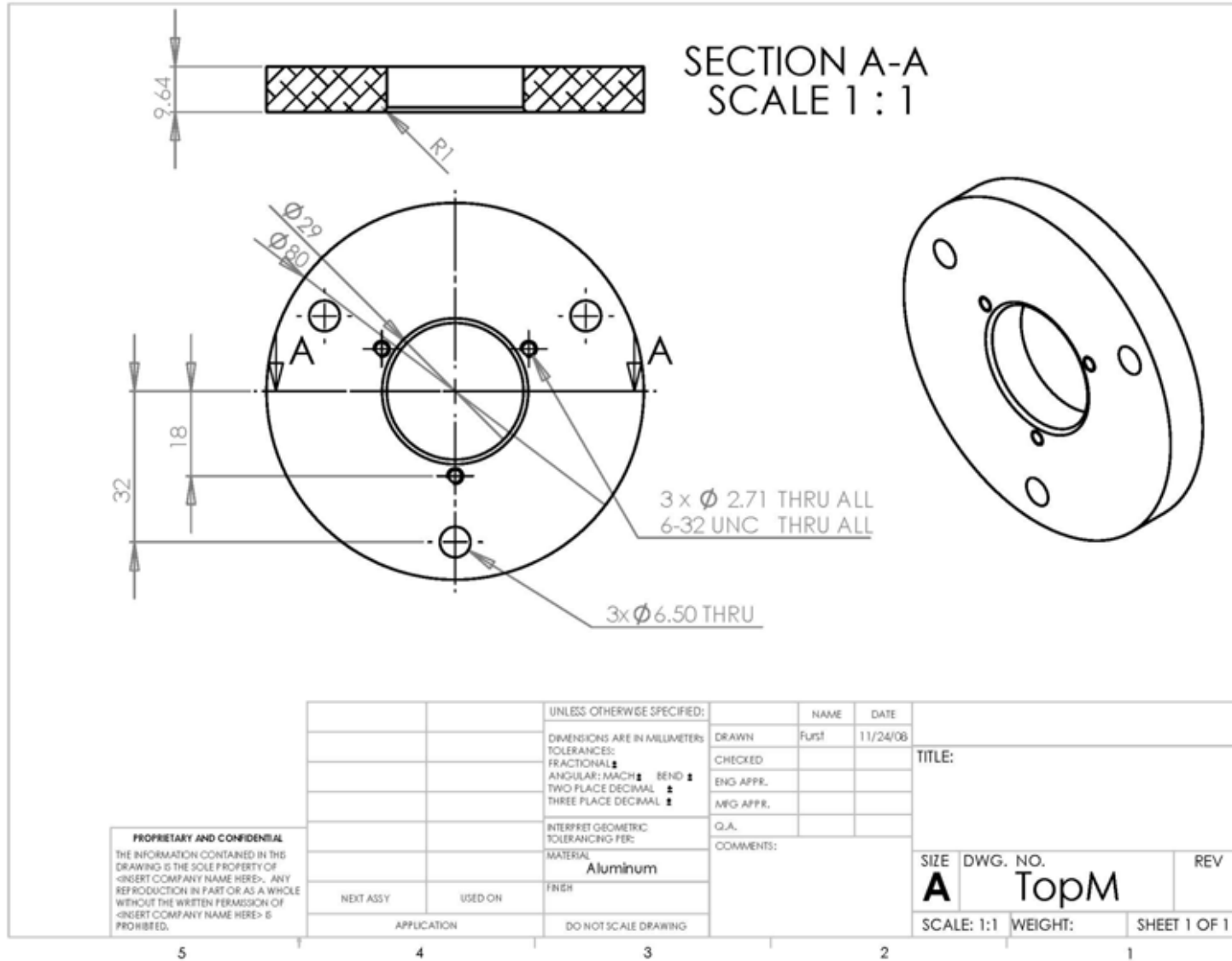
5

4

3

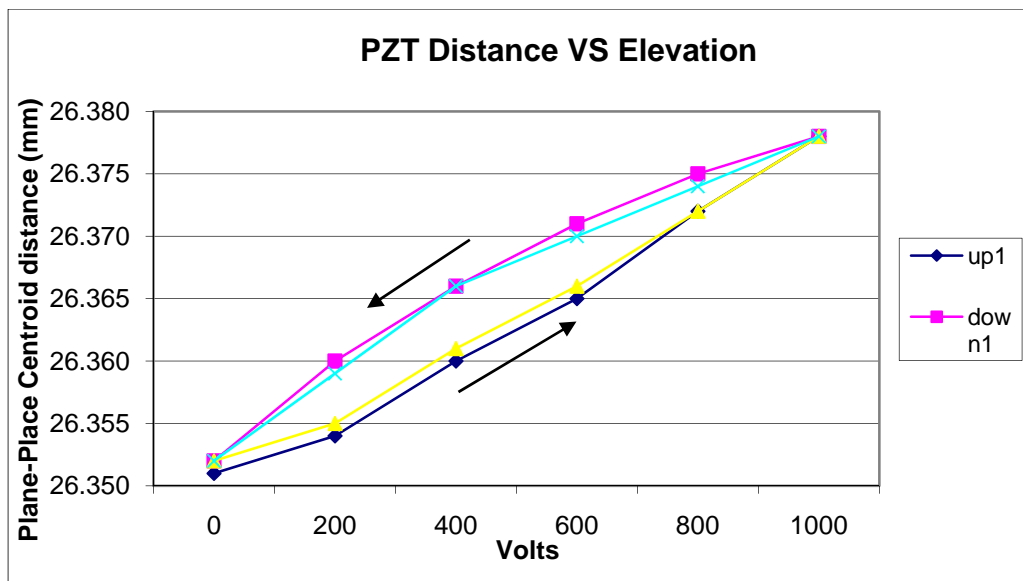
2

1

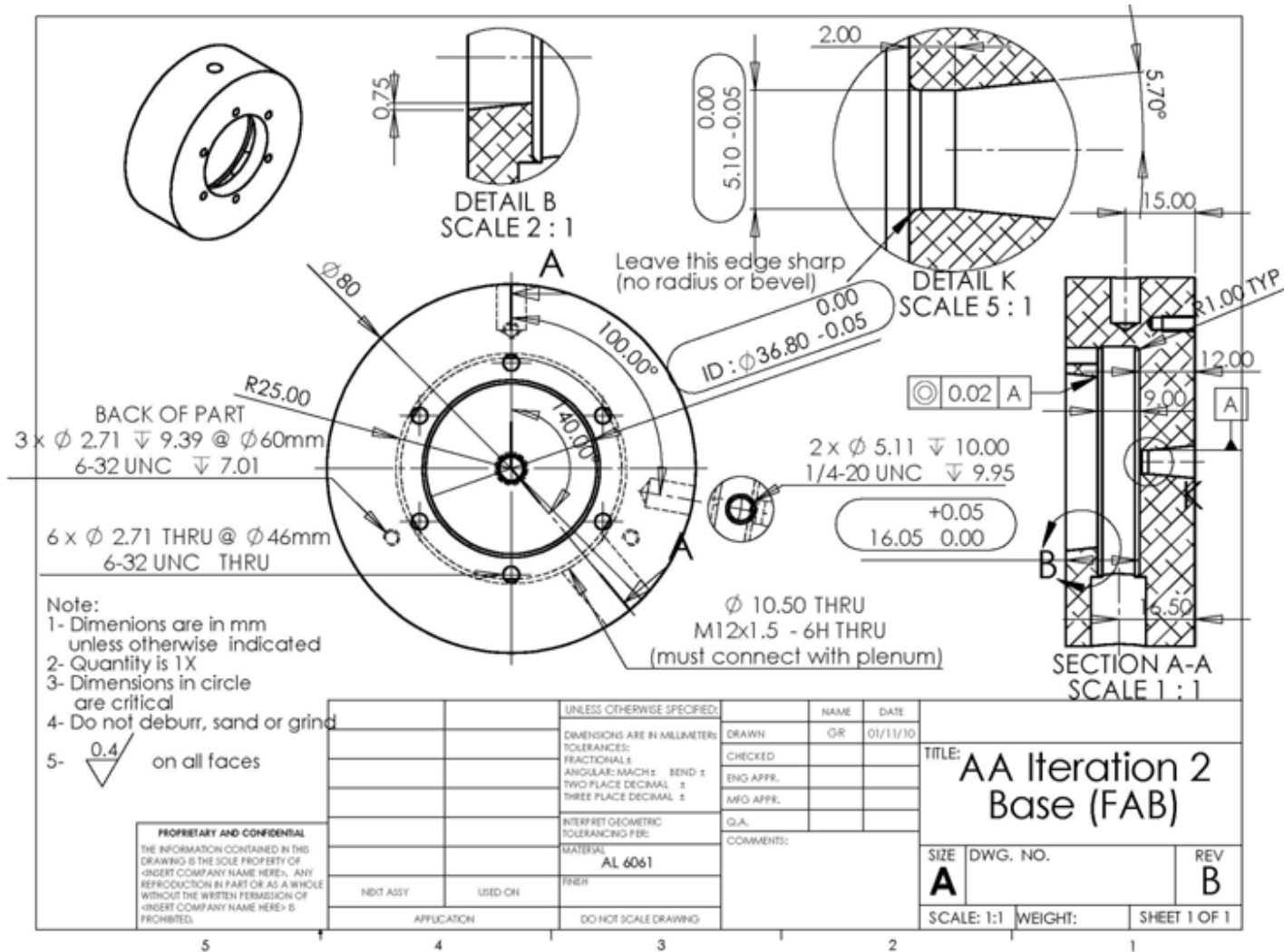


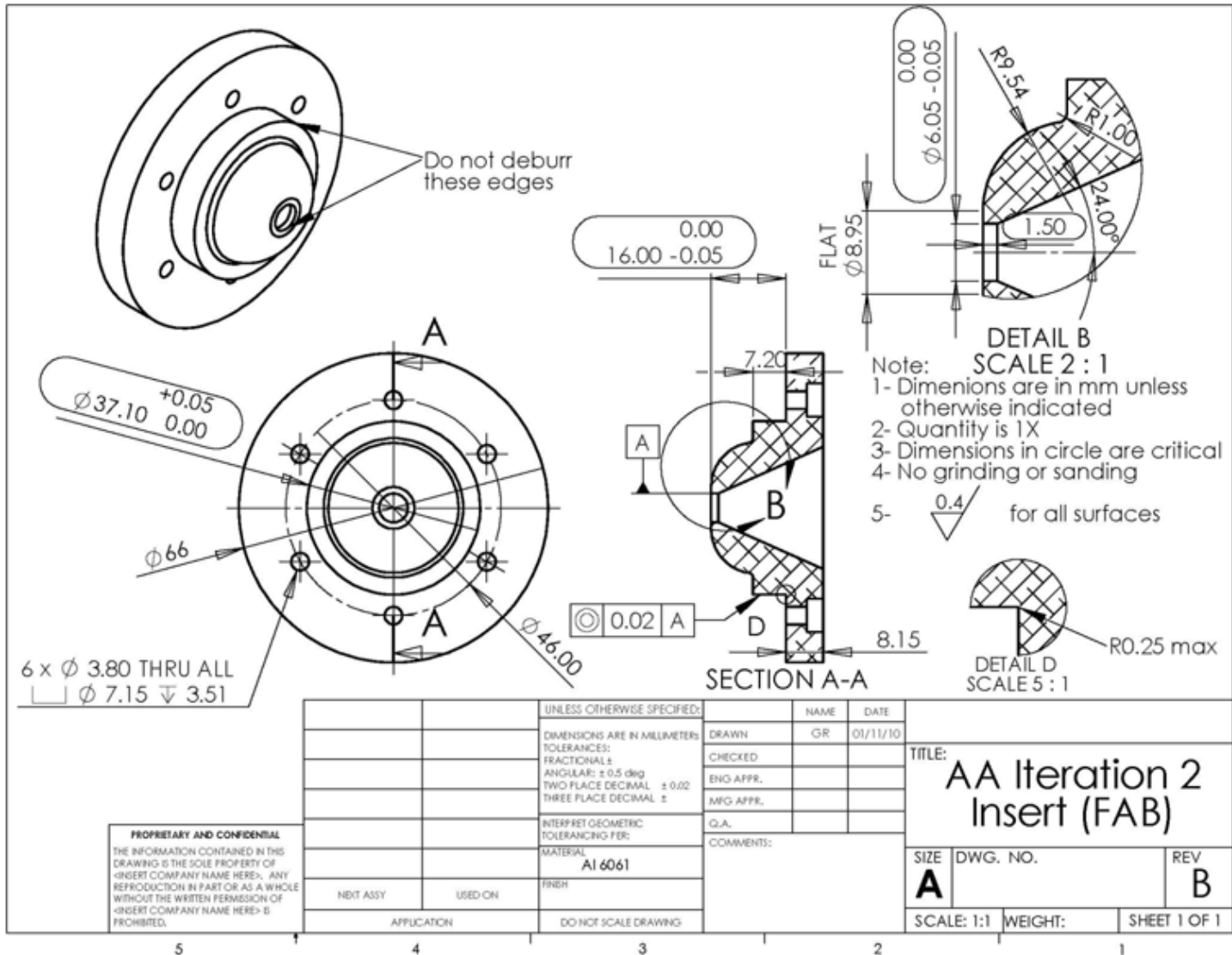
APPENDIX B – Additional Measurements on First Iteration of Air Amplifier

| Voltage | Dist (mm) | Parallelism (mm) |
|---------|-----------|------------------|
| 0 | 26.351 | 0.001 |
| 200 | 26.354 | 0.002 |
| 400 | 26.360 | 0.001 |
| 600 | 26.365 | 0.001 |
| 800 | 26.372 | 0.001 |
| 1000 | 26.378 | 0.003 |
| 800 | 26.375 | 0.001 |
| 600 | 26.371 | 0.001 |
| 400 | 26.366 | 0.001 |
| 200 | 26.360 | 0.002 |
| 0 | 26.352 | 0.001 |
| 200 | 26.355 | 0.002 |
| 400 | 26.361 | 0.003 |
| 600 | 26.366 | 0.002 |
| 800 | 26.372 | 0.002 |
| 1000 | 26.378 | 0.002 |
| 800 | 26.374 | 0.002 |
| 600 | 26.370 | 0.002 |
| 400 | 26.366 | 0.003 |
| 200 | 26.359 | 0.003 |
| 0 | 26.352 | 0.002 |



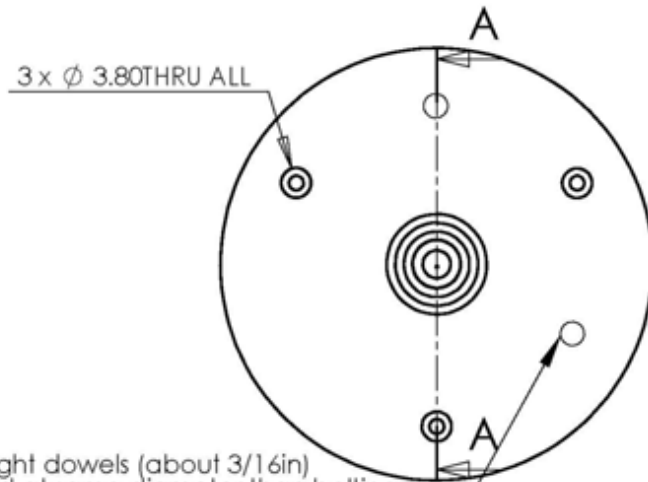
APPENDIX C – Second Iteration of Air Amplifier – Parts and Drawings



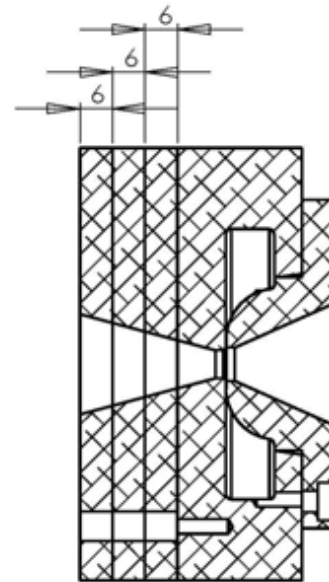


Proposed Instructions :

- 1- Machine base part as per drawing (except for cone)
- 2- machine the 3 additional plates to 6mm thickness (machine both side)
- 3-Dowel to base and bolt in place the plates
- 4- Machine cone to angle prescribed on base drawing



2X straight dowels (about 3/16in) located at same diameter than bolting. Need to be able to be assemble and disassembled few times (LC5 clearance). Depth in base is 1.5dia of dowel



SECTION A-A
SCALE 1 : 1

PROPRIETARY AND CONFIDENTIAL
THE INFORMATION CONTAINED IN THIS DRAWING IS THE SOLE PROPERTY OF <INSERT COMPANY NAME HERE>. ANY REPRODUCTION IN PART OR AS A WHOLE WITHOUT THE WRITTEN PERMISSION OF <INSERT COMPANY NAME HERE> IS PROHIBITED.

| | | | | | | | |
|-------------|--|---------------------------------------|--|------------|----------|--------------|--|
| | | UNLESS OTHERWISE SPECIFIED: | | NAME | DATE | | |
| | | DIMENSIONS ARE IN MILLIMETERS | | DRAWN | GR | 01/20/10 | |
| | | TOLERANCES: | | CHECKED | | | TITLE: AA Iteration 2 Extra plates |
| | | FRACTIONAL ± | | ENG APPR. | | | |
| | | ANGULAR: MACH ± BEND ± | | MFG APPR. | | | |
| | | TWO PLACE DECIMAL ± | | Q.A. | | | |
| | | THREE PLACE DECIMAL ± | | COMMENTS: | | | |
| | | INTERF RET GEOMETRIC TOLERANCING PER: | | | | | |
| | | MATERIAL | | | | | |
| | | AL 6061 T6 | | | | | |
| | | FINISH | | | | | |
| NEXT ASSY | | USED ON | | | | | |
| APPLICATION | | DO NOT SCALE DRAWING | | | | | |
| | | | | SIZE | DWG. NO. | REV | |
| | | | | A | | B | |
| | | | | SCALE: 1:1 | WEIGHT: | SHEET 1 OF 1 | |

5

4

3

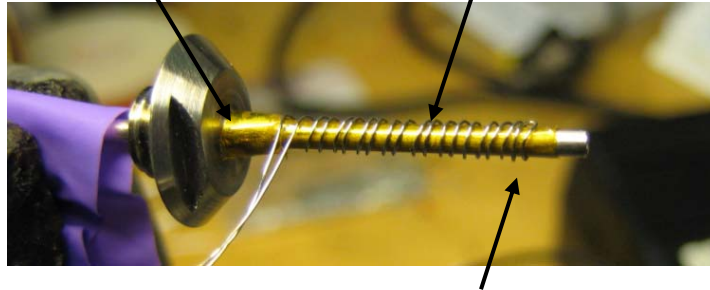
2

1

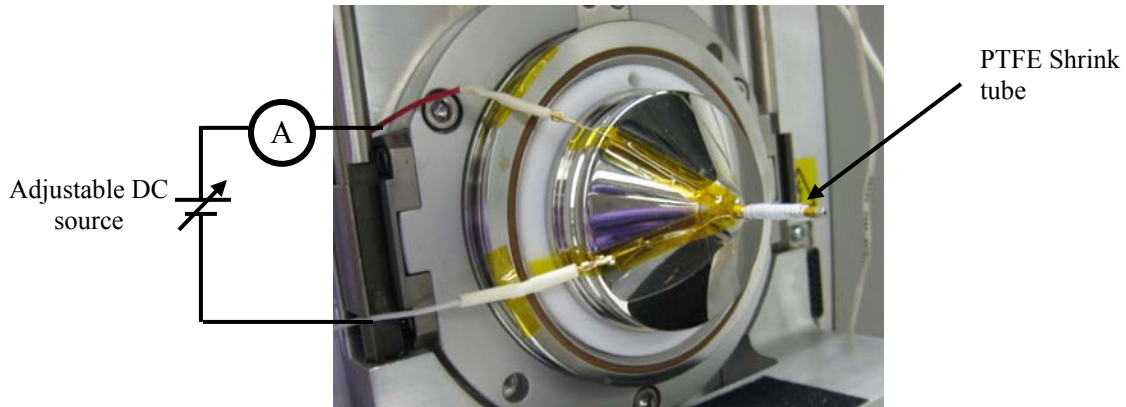
APPENDIX D – Heating of the Mass Spectrometer inlet

Kapton Tape (rated operating temperature of 280 °C)

Nichrome 60, 32 AWG wound in parallel to avoid creating magnetic field



160 °C Measured at tip with thermocouple probe with 0.6 Amp DC on test bench, same as temperature measured on tip of regular MS inlet



Effect of Heater on Total ion Current

